Modelling neuropathic pain in vitro: A multimodal approach using induced-pluripotent stem cell-derived sensory neurons and mechanically compressed keratinocytes

Von der Fakultät für Mathematik und Naturwissenschaften der RWTH Aachen University zur Erlangung des akademischen Grades eines Doktors der Naturwissenschaften genehmigte Dissertation
vorgelegt von

Fiona Maria Roll, M.Sc.

aus

Bergisch Gladbach, Deutschland

Berichter: Prof. Dr.-Ing. Laura De Laporte

Prof. Dr. med Angelika Lampert

Tag der mündlichen Prüfung: 19.02.2026

Diese Dissertation ist auf den Internetseiten der Universitätsbibliothek verfügbar.

Table of contents

Summary

Neuropathic pain is a chronic pain disorder arising from a dysfunction of the somatosensory nervous system, often resulting in altered activity of voltage-gated sodium channels (Na_v). However, the molecular mechanism is complex and not fully understood. Therefore, this thesis investigated the development of advanced *in vitro* models for neuropathic pain, with a focus on sensory neurons and the keratinocytes surrounding them in the skin.

Human induced pluripotent stem cells (iPSCs) reprogrammed from somatic cells of healthy individuals and neuropathic pain patients offer a unique opportunity to obtain human sensory neurons harboring the donor's genotype. IPSC-derived sensory neurons have been successfully used to model phenotypes of small fiber neuropathy (SFN) patients with mutations in $Na_v1.7$. The tetrodotoxin-resistant (TTXr) channels $Na_v1.8$ and $Na_v1.9$ critically modulate nociceptor excitability, and variants have been linked to neuropathic pain. However, the functional presence of $Na_v1.8$ and $Na_v1.9$ in iPSC-derived sensory neurons is unclear. Here, iPSCs from two SFN patients with a putative pathogenic $Na_v1.9$-Y66S variant were employed to evaluate iPSC-sensory neurons as neuropathic pain models, focusing on TTX-resistant currents, neuronal excitability, and action potential characteristics, as well as modelling of the $Na_v1.9$-Y66S phenotype. The three iPSC-sensory neuron differentiation protocols employed – small-molecule- or transcription factor-overexpression-driven – yielded comparable TTXr currents. However, no persistent $Na_v1.9$-like current or clearly-identifiable $Na_v1.8$ current could be detected, indicating that the TTXr currents largely consist of $Na_v1.5$ current. This is consistent with a hyperpolarizing shift of activation and inactivation of iPSC-sensory neurons compared to mouse dorsal root ganglia (DRG) and indicates a developmental stage of the iPSC-sensory neurons distinct from mature DRG neurons. In contrast, the neuronal excitability and action potential characteristics were comparable to native human DRG neurons. Disease modelling of $Na_v1.9$-Y66S revealed increased firing frequency and narrowed action potentials in patient-derived sensory neurons in the small molecule-driven differentiation, raising the possibility of marginal $Na_v1.9$ activity below the detection limit or additional modulatory factors contributing to the phenotype.

Recent studies have attributed an essential role to keratinocytes in touch and pain sensation. Patients with pachyonychia congenita (PC) carry mutations in keratins, resulting in palmoplantar keratosis, which increases the mechanical load locally, and neuropathic pain in the affected regions. Shaving of the callus does not alleviate the pain, indicating a chronic pain phenotype. Therefore, this thesis aimed to investigate whether mechanically compressed keratinocytes could sensitize sensory nerves. For this, a keratinocyte monolayer cyclic compression system was developed. Keratinocytes from PC patients intrinsically showed a pro-inflammatory phenotype trend on the mRNA level, which was exacerbated by cyclic mechanical compression for 1 h at 150 mHz at 0.9 kPa compressive force. However, conditioned media from compressed keratinocytes failed to alter the excitability of mouse DRG neurons.

In conclusion, iPSC-sensory neurons, despite displaying limited $Na_v1.8$ or $Na_v1.9$ currents, demonstrate potential for disease modelling, but the model requires further advancements to allow for precise modelling of native human nociceptors. Mechanically stressed keratinocytes may contribute to pain in PC through sensory nerve sensitization via inflammation, but further experiments are required to understand the extent and molecular mechanisms behind it. Both iPSC- sensory neurons and mechanically compressed keratinocytes present valuable models to answer burning questions in pain research, but will benefit from further optimization and ultimately integration into larger, more complex models featuring multiple cell types.

Zusammenfassung

Neuropathischer chronischer Schmerz entsteht durch eine Dysfunktion des somatosensorischen Nervensystems und tritt häufig mit veränderter Aktivität der spannungsabhängigen Natriumkanäle (Na_v) auf. Die zugrunde liegenden molekularen Mechanismen sind jedoch komplex und bislang nicht vollständig aufgeklärt. Ziel dieser Arbeit war daher die Entwicklung von *in-vitro*-Modellen für neuropathischen Schmerz mit einem Schwerpunkt auf sensorischen Neuronen und den sie umgebenden Keratinozyten der Haut.

Humane induzierte pluripotente Stammzellen (iPSCs) können aus somatischen Zellen von gesunden Individuen und neuropathischen Schmerzpatienten gewonnen werden und zu humane sensorische Neuronen mit dem Genotyp des Spenders differenziert werden. Aus iPSCs abgeleitete sensorische Neuronen (iPSC-SN) wurden bereits erfolgreich genutzt, um Phänotypen von Patienten mit Small-Fiber-Neuropathie (SFN) und Mutationen im $Na_v1.7$-Kanal zu modellieren. Die Tetrodotoxin-resistenten (TTXr) Kanäle $Na_v1.8$ und $Na_v1.9$ tragen entscheidend zur Erregbarkeit von Nozizeptoren bei, und Mutationen in diesen Kanälen wurden mit neuropathischen Schmerzen assoziiert. Jedoch ist die funktionelle Präsenz von $Na_v1.8$ und $Na_v1.9$ in iPSC-SN noch nicht gezeigt worden. In dieser Arbeit wurden iPSCs von zwei SFN-Patienten mit einer potenziell pathogenen $Na_v1.9$-Y66S-Variante verwendet, um iPSC-SN als Modelle für neuropathischen Schmerz zu evaluieren. Die drei verwendeten Differenzierungsprotokolle für iPSC-SN – gesteuert über die Zugabe von Entwicklungsfaktoren oder Transkriptionsfaktorüberexpression – ergaben vergleichbare TTXr-Ströme. Es konnte jedoch weder ein persistierender $Na_v1.9$-Strom noch ein eindeutig identifizierbarer $Na_v1.8$-Strom nachgewiesen werden, was darauf hindeutet, dass die TTXr-Ströme größtenteils $Na_v1.5$ zuzuordnen sind. Dies weist auf ein Entwicklungsstadium der iPSC-SN hin. Im Gegensatz dazu waren die neuronale Erregbarkeit und die Eigenschaften der Aktionspotentiale vergleichbar mit nativen humanen Spinalganglion (DRG)-Neuronen. Die Krankheitsmodellierung der $Na_v1.9$-Y66S-Variante zeigte in patientenabgeleiteten iPSC-SN eine erhöhte Feuerrate sowie schmalere Aktionspotentiale; dies lässt auf eine möglicherweise marginale, unterhalb der Nachweisgrenze liegende Aktivität von $Na_v1.9$ oder zusätzliche modulierende Faktoren schließen, die zum beobachteten Phänotyp beitragen.

Keratinozyten spielen eine essenzielle Rolle bei Berührungs- und Schmerzwahrnehmung. Patienten mit Pachyonychia congenita (PC) tragen Mutationen in Keratinen, was zu palmoplantaren Keratosen und zu neuropathischen Schmerzen führt. Das Abtragen der Schwielen resultiert nur in einer teilweisen Schmerzreduktion, was auf einen chronischen Schmerzphänotyp hinweist. Daher wurde in dieser Arbeit untersucht, ob mechanisch komprimierte Keratinozyten sensorische Nerven sensibilisieren können. Hierzu wurde ein System zur zyklischen Kompression kultivierter Keratinozyten entwickelt. Keratinozyten von PC-Patienten zeigten bereits intrinsisch einen Trend zu einem proinflammatorischen Phänotyp auf mRNA-Ebene; dieser wurde durch zyklische mechanische Kompression über 1 Stunde bei 150 mHz Frequenz und 0,9 kPa Druck weiter verstärkt. Dennoch führten konditionierte Medien komprimierter Keratinozyten nicht zu einer veränderten Erregbarkeit in Maus-DRG-Neuronen. Zusammenfassend zeigen iPSC-SN trotz begrenzter Nachweisbarkeit von $Na_v1.8$- oder $Na_v1.9$-Strömen Potenzial als Modell für neuropathischen Schmerz; jedoch bedarf es weiterer Optimierung zur präzisen Modellierung nativer humaner Nozizeptoren. Mechanisch gestresste Keratinozyten könnten über inflammatorische Prozesse zur Sensibilisierung sensorischer Nerven in PC-Patienten beitragen; hierzu sind jedoch weitere Untersuchungen erforderlich, um das Ausmaß und die molekularen Mechanismen besser zu verstehen. Beide Modelle profitieren von weiterer Optimierung sowie letztlicher Integration in größere, komplexere Systeme, um neuropathische Schmerzen akkurat *in vitro* zu erforschen.

1 Introduction

The five senses—touch, taste, smell, sight, and hearing—serve as fundamental links between the human body and its environment, playing a crucial role in survival. When one of these senses is exposed to a stimulus that exceeds the innocuous range, the body may perceive pain, a mechanism that signals potential harm and initiates protective responses (Julius & Basbaum, 2001). This thesis focuses on the detection of mechanical stimuli and pain, as well as the consequences that arise when these finely tuned systems are disrupted by disease.

1.1 The peripheral nervous system

Chemical and physical stimuli, whether originating from the external environment or within the body, are detected and transduced into sensory information by receptors in the peripheral nervous system (PNS). This information is subsequently relayed by the PNS to the central nervous system (CNS), where conscious or unconscious decisions occur based on the sensory input. The PNS also transmits motor signals from the CNS to target organs, converting neural signals into chemical signals at synapses within the target tissues. Without the PNS, humans would not be able to perceive stimuli from the outside world (Boron & Boulpaep, 2012).

The PNS consists of the spinal cord with its spinal nerves and their branches. Each spinal nerve is formed by the convergence of the dorsal and ventral nerve roots. The dorsal roots coalesce into a spindle-shaped structure known as the dorsal root ganglion, which contains the cell bodies of sensory neurons—referred to as dorsal root ganglia (DRG) neurons. These neurons are typically pseudounipolar, possessing a single axonal process that bifurcates into a peripheral and a central branch, forming a characteristic T-shape (Boron & Boulpaep, 2012).

DRG neurons or sensory neurons can be classified based on their size and conduction velocity or based on their function. In the former category, there are three main groups according to Erlanger and Gasser: large-diameter Aα- and Aβ-fibers, medium-sized Aδ-fibers, and small-diameter C-fibers (Figure 1) (Erlanger & Gasser, 1924). Similarly, Lloyd and Hunt categorized sensory neurons into four groups of decreasing diameter: group 1 corresponds to Aα-fibers, group 2 to Aβ-fibers, group 3 to Aδ-fibers and group 4 to C-fibers (Hunt, 1954; Lloyd, 1943). Aα and Aβ-fibers are thickly myelinated and therefore conduct action potentials rapidly. Aδ-fibers have an intermediate diameter and conduction velocity, with thin myelination. In contrast, C-fibers possess thin, unmyelinated axons, resulting in slower conduction velocities (Bennett et al., 2019; Erlanger & Gasser, 1924). Functionally, sensory neurons can be divided based on their responsiveness to mechanical, thermal, or chemical stimuli in the normal or noxious range. Aα-fibers innervate muscle spindles and act as proprioceptors. Aβ-fibers can also act as proprioceptors but predominantly respond to mechanical stimuli such as touch and pressure. Aδ- and C-fibers primarily function as nociceptors, mechanoreceptors and thermoreceptors and typically terminate in free nerve endings within their target tissues, such as the skin (Bennett et al., 2019; Kupari & Ernfors, 2023).

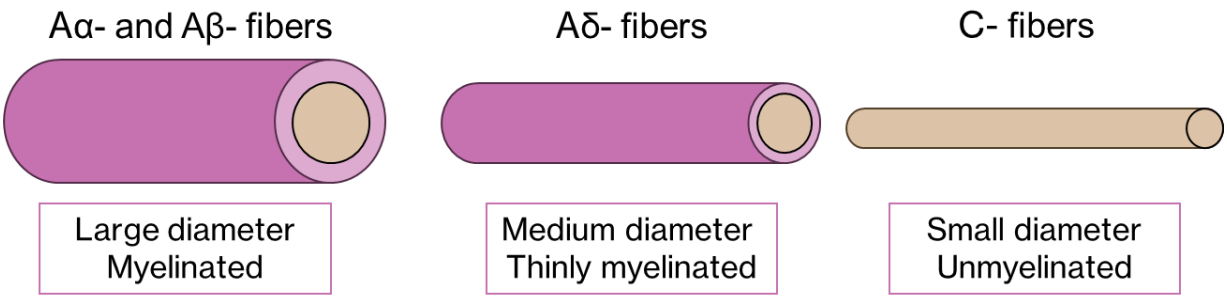

Figure 1 Sensory nerve fiber types according to Erlanger & Gasser. Sensory neurons can be classified based on their diameter and conduction velocity. Aα and Aβ-fibers are thickly myelinated and conduct action potentials rapidly. Aδ-fibers have an intermediate diameter and conduction velocity, with thin myelination. C-fibers possess thin, unmyelinated axons, resulting in slower conduction velocities **(Erlanger & Gasser, 1924)**. Created with Biorender.

1.2 The skin as a somatosensory organ

The skin fulfills multiple essential functions in the human body: (1) it acts as a protective barrier against external hazards such as microorganisms, harmful substances, and ultraviolet (UV) radiation; (2) it contributes to thermoregulation; and (3) it plays a fundamental role in somatosensation (Speckmann et al., 2024).

The skin is composed of three distinct layers: the deep hypodermis, the intermediate dermis, and the outer epidermis. The hypodermis, also referred to as the subcutaneous layer, is a connective tissue layer that contains adipocytes and anchors the skin to the underlying tissue (Figure 2). Above this lies the dermis, which is primarily composed of an extracellular matrix produced by fibroblasts. This layer is rich in collagen and elastin, providing both mechanical stability and elasticity to the skin. Additionally, the dermis contains capillaries, mechanoreceptors, thermoreceptors, sweat glands, sebaceous glands, hair follicles and free nerve endings. The epidermis consists predominantly of keratinocytes (~85%), along with Langerhans cells (~10%) and melanocytes (~5%) and additionally contains Merkel cells and free nerve endings. It is organized into four distinct layers, progressing from the basal layer to the surface. The stratum basale, the deepest layer, contains proliferating keratinocytes. Above this, in the stratum spinosum, keratinocytes lose their proliferative capacity and begin to differentiate, resulting in enhanced mechanical properties and strengthened intercellular adhesion. The differentiation continues in the stratum granulosum, where keratinocytes become increasingly flattened and undergo terminal differentiation. This process is characterized by reinforced intracellular adhesion, an enhanced cytoskeletal structure, and increased phospholipid synthesis. In the outermost layer, the stratum corneum, keratinocytes transform into corneocytes, which form a protective barrier exposed to air and the external environment (Shutova & Boehncke, 2022; Speckmann et al., 2024). The skin plays a crucial role in the sensation of mechanical stimuli (mechanosensation) and pain (nociception).

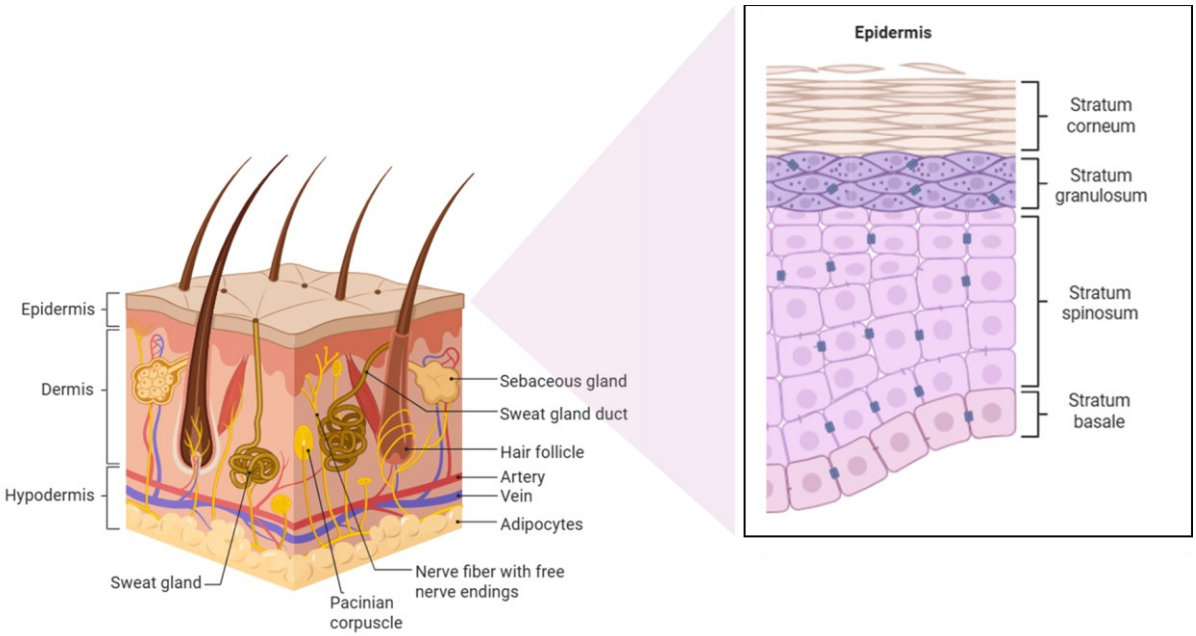

Figure 2 Structure of the skin and the epidermis. The skin consists of the hypodermis, dermis and epidermis. The hypodermis contains adipocytes, while the dermis contains glands, blood vessels, hair follicles, mechanoreceptors (here shown as Pacinian corpuscle) and free nerve endings. The epidermis primarily consists of keratinocytes but also contains immune cells, free nerve endings, melanocytes and Merkel cells. The keratinocytes in the epidermis are present in different proliferation states organized into four distinct layers: the stratum basale, stratum spinosum, stratum granulosum and stratum corneum. Created with Biorender.

1.3 Mechanosensation

Mechanosensation occurs via mechanoreceptors, which are sensitive to mechanical forces such as bending or stretching. Mechanoreceptors are present throughout different tissues of the human body, including the skin. The skin contains multiple types of mechanoreceptors, each specialized in detecting distinct mechanical stimuli. These receptors can be classified as either slowly or rapidly adapting and have varying receptive field sizes, allowing the brain to decode the nature and precise location of mechanical stimuli. This results in the remarkable sensitivity of the skin, where a dot as small as 0.006 mm in height and 0.04 mm in width can already be detected by specialized receptors (Boron & Boulpaep, 2012).

Human glabrous skin contains four main mechanoreceptor types: Merkel's disks, Meissner's corpuscles, Ruffini's corpuscles, and Pacinian corpuscles (Figure 3). While hairy skin mainly contains hairs connected to a nervous apparatus consisting of lanceolate, circumferential or free nerve endings, occasionally the root of the hair can be associated with Merkel cells, Ruffini or Pacinian corpuscles (Cobo et al., 2020). Pacinian corpuscles are located in the subcutaneous tissue and consist of layers of connective tissue wrapped around a nerve terminal. When the capsule is compressed, the nerve terminal membrane deforms, opening mechanosensitive ion channels and triggering an action potential. Even when a stimulus is sustained, the viscous fluid between the connective tissue layers allows them to shift, relieving pressure from the nerve terminal. This structural adaptation makes Pacinian corpuscles highly sensitive to vibrations but largely unresponsive to steady pressure. Ruffini's corpuscles resemble Pacinian corpuscles structurally but are smaller. They are found in the dermis and subcutaneous tissue and serve as

slowly adapting receptors, responding optimally to low-frequency vibrations and skin stretch (Boron & Boulpaep, 2012; Cobo et al., 2020). Merkel's disks consist of flattened epithelial cells that form synapses with nerve terminals. They are located at the interface between the epidermis and dermis and are classified as slowly adapting receptors, making them particularly sensitive to sustained pressure and texture. In contrast, Meissner's corpuscles are situated in the dermal ridges and are rapidly adapting mechanoreceptors. Both Merkel's disks and Meissner's corpuscles play key roles in mediating light touch perception (Boron & Boulpaep, 2012). In addition to mechanosensation, mechanotransduction plays an important role in skin homeostasis.

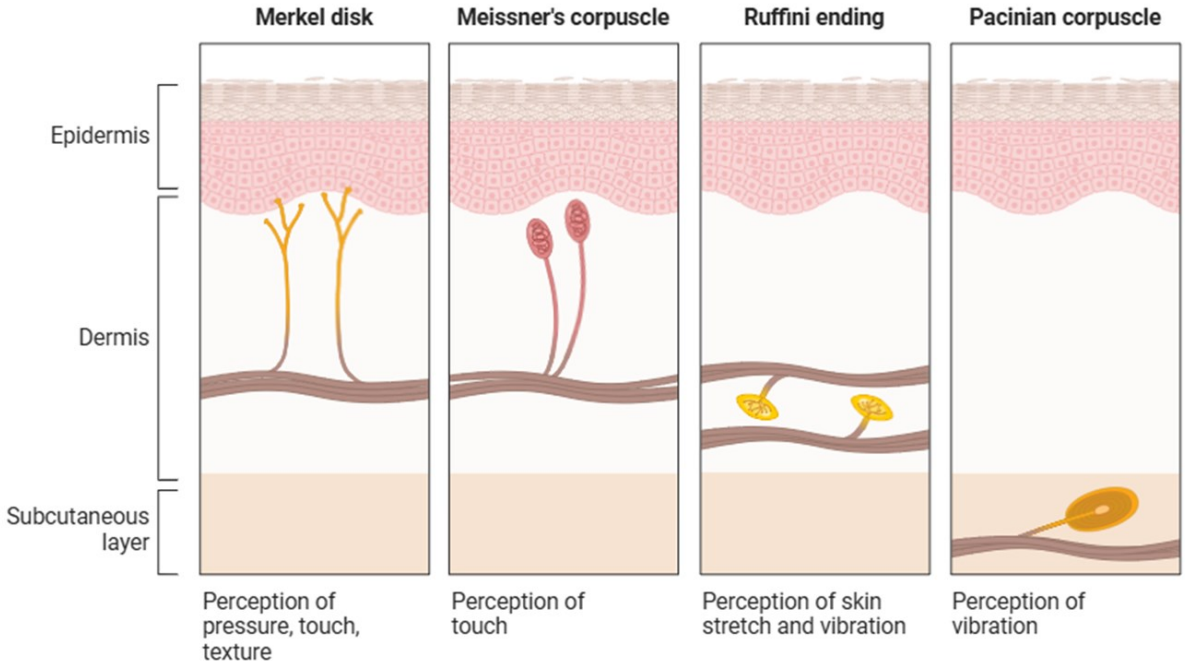

Figure 3 Mechanoreceptors in the skin. Merkel disks are located at the interface between the epidermis and dermis and are sensitive to sustained pressure, texture and light touch. Meissner's corpuscles are located in the upper ridges of the dermis and mediate light touch. Ruffini endings or corpuscles are located in the dermis and subcutaneous tissue (hypodermis) and respond to skin stretch and low-frequency vibrations. Pacinian corpuscles are located in the subcutaneous tissue and are sensitive to vibrations. Created with Biorender.

1.4 Mechanotransduction

Mechanotransduction describes the capability of cells to sense and transform mechanical cues from their environment into biochemical signals. It regulates cell proliferation, motility and differentiation and thereby cell phenotype and fate. Mechanotransduction occurs through mechanically-gated ion channels and structural proteins (Shutova & Boehncke, 2022).

Mechanically-activated (MA) ion channels are a broad class of ion channels whose open probability changes in the presence of mechanical stimuli. The primary ion channel families involved in skin mechanosensation are Piezo and transient receptor potential (TRP) channels (Martinac & Cox, 2017; Mikesell et al., 2022).

Piezo1 and Piezo2 are mechanically gated, non-selective cation channels. The channels are expressed in various hollow organs such as the lung, skin, bladder or vasculature. Piezo1 is

expressed in keratinocytes, whereas Piezo2 is expressed in sensory neurons and Merkel cells (Martinac & Cox, 2017; Mikesell et al., 2022). Knockout (k.o.) of Piezo1 decreases the firing rate of sensory neurons in the skin after mechanical stimuli *in vitro* and diminishes behavioral responses to noxious and innocuous mechanical stimuli *in vivo* (Mikesell et al., 2022). TRP channels are a diverse family of cation channels that can respond to a wide range of stimuli, including mechanical forces. One example of a mechanosensitive TRP channel is TRPV4, which mainly responds to osmotic pressure and is expressed in Merkel cells, DRG neurons and keratinocytes (Basbaum et al., 2009; Martinac & Cox, 2017). TRPV4 k.o. mice exhibit normal acute mechanosensation but show deficits in mechanical and thermal algesia (Basbaum et al., 2009). Other prominent ion channels that seem to play a lesser role in mechanotransduction are the potassium channels K2P and the mammalian epithelial sodium channels (ENaC) (Martinac & Cox, 2017).

In addition to mechanically-activated ion channels, different structural components of the cell are important for mechanotransduction, namely the actin-myosin cytoskeleton, integrins, cell-cell adhesions, and intermediate filaments. The actin cytoskeleton is a dynamic, mechanosensitive system that generates pushing and pulling forces and is essential for cell adhesion, migration, cytokinesis, membrane trafficking and secretion of proteins and differentiation. Nonmuscle-myosin II is a motor protein that is responsible for the majority of the force generated by the cell. Integrins are receptors that connect cells to the extracellular matrix (ECM). Upon mechanical activation, integrins cluster and strengthen the adhesion between the ECM and the actin-myosin cytoskeleton in so-called focal adhesion points. Additionally, they activate multiple proliferative and pro-survival pathways, such as the MAP kinase cascade and the Rac- and Ras-mediated pathways. Cell-Cell adhesions include adherens junctions, tight junctions, desmosomes and gap junctions. They function as mechanosensors and transducers, and provide adhesion and semipermeable barriers (Shutova & Boehncke, 2022).

Intermediate filaments have previously been thought to only provide mechanical stability to cells, but have recently become recognized as important in mechanotransduction. Mechanical stimuli are transmitted through cell-cell junctions and cell-ECM adhesions to the intermediate filaments, which are connected to the actin-associated cadherin and integrins. The ability of intermediate filaments to deform and stretch enables cells to withstand and counterbalance mechanical forces. One type of intermediate filaments that are prominent in keratinocytes are keratins. The keratin subtype expression pattern is defined by the differentiation status of the keratinocyte. The keratin network can regulate keratinocyte rigidity sensing and nuclear mechanotransduction (Laly et al., 2021; Shutova & Boehncke, 2022). The significance of keratins in keratinocyte proliferation is evident in patients with mutations in keratin genes, as discussed later in the section on pachyonychia congenita (1.11).

1.5 Nociception

Nociception is the process of encoding noxious stimuli (International Association for the Study of Pain, 2011). Nociception is performed by a subset of sensory neurons called nociceptors, which are excited by thermal, mechanical or chemical stimuli that reach a noxious range (Basbaum et al., 2009). To sense noxious stimuli from the environment, Aδ- and C-fiber nociceptors have free nerve endings in the skin. Some nociceptors respond specifically to mechanical, thermal or chemical noxious stimuli, whereas polymodal nociceptors respond to at least two of the listed stimuli (Boron & Boulpaep, 2012). Aδ-fibers often function as mechanical nociceptors and more rarely as thermoreceptors. Most C-fibers are polymodal, but a small subpopulation is only

responsive to heat, mechanical or mechano-cooling stimuli (D. Bennett et al., 2019). In addition, a group of ordinarily mechano-insensitive C-fibers exists that can become mechanosensitive upon nerve sensitization (so-called CMi-fibers or silent nociceptors) (Namer & Lampert, 2025). A key difference between Aδ- and C-fiber nociceptors can be found in their transmission of different kinds of nociceptive stimuli: While Aδ-nociceptors convey well-localized stimuli very quickly, which is experienced as sharp pain, C-nociceptors transmit poorly localized stimuli much slower, which is experienced as delayed, dull pain (Kupari & Ernfors, 2023).
On a molecular level, both ligand-gated and voltage-gated channels play a pivotal role in the detection of high-threshold stimuli by nociceptors. Two of the most researched ion channels relevant for nociception are the TRP channels and the voltage-gated sodium channels. The first TRP channel to be linked to nociception was TRPV1, which is activated by noxious heat, capsaicin and low pH. Others are TRPV2, which responds to high temperature, and TRPA1, which responds to noxious cold and various chemical substances (Bennett et al., 2014).

1.6 Voltage-gated sodium channels

Voltage-gated sodium channels (VGSCs or Na_vs) are selective Na^+ channels that are gated by voltage. These ion channels are key determinants of nociceptor excitability and contribute to the action potential shape, repetitive action potential firing, amplification of subthreshold stimuli, resting membrane potential of the neuron and neurotransmitter release at the synapse. Due to their central role in neuronal activity, alterations in VGSC function can result in drastic changes in nerve fiber excitability and neuropathic pain phenotypes (Bennett at al., 2014).

1.6.1 Structure and gating of voltage-gated sodium channels

VGSCs are transmembrane proteins that are made up of a pore-forming alpha subunit and associated beta subunits. The alpha subunit is arranged in four domains (DI-DIV), each consisting of six transmembrane segments (S1-S6) (Figure 4A). The S1-S4 transmembrane segments act as a voltage sensor. A group of positively charged amino acids on S4 is especially important for the voltage-sensing of VGSCs. The S5 and S6 segments form the pore of the channel. The loops between S5 and S6 of each domain form the outer vestibule of the channels, which contains the ion selectivity filter (Bennett et al., 2019).
In principle, VGSCs can exist in three voltage-dependent conformational states: open, closed and inactive (Figure 4B). At hyperpolarized membrane potentials, the channel will be closed and nonconducting. Upon depolarization, the positively-charged voltage sensors will move outward, which pulls the pore open (Bennett et al., 2019). As the Na^+ ion concentration is much higher outside of the cell, Na^+ will rapidly move into the cell, creating an inward current. After a short opening period of below 1 ms, the channel enters a state called fast inactivation. Steady-state fast inactivation is mediated by the IFM motif, which is located on the intracellular loop between domains 3 and 4 and closes the channel pore upon binding to its side. In addition to fast inactivation, which occurs on a millisecond time scale, VGSCs can be inactivated via prolonged depolarizations, a process called slow inactivation. The slow inactivation state is very stable and recovery from it requires prolonged repolarization. The mechanism behind slow inactivation is still being researched, but it presumably depends on a rearrangement of the domains of the alpha subunit, ultimately closing the pore. Inactive channels are non-conducting and cannot be opened by depolarization of the membrane. Upon re-hyperpolarization of the membrane, the voltage sensor will return to its position towards the inside of the cell. The channel has now returned to

the closed state and can be activated again by depolarization of the membrane (Bennett et al., 2019). It should be noted that this is a simplified overview of the Na_v channel gating; there are more channel conformations, such as the open channel block, that will not be discussed in the scope of this thesis.

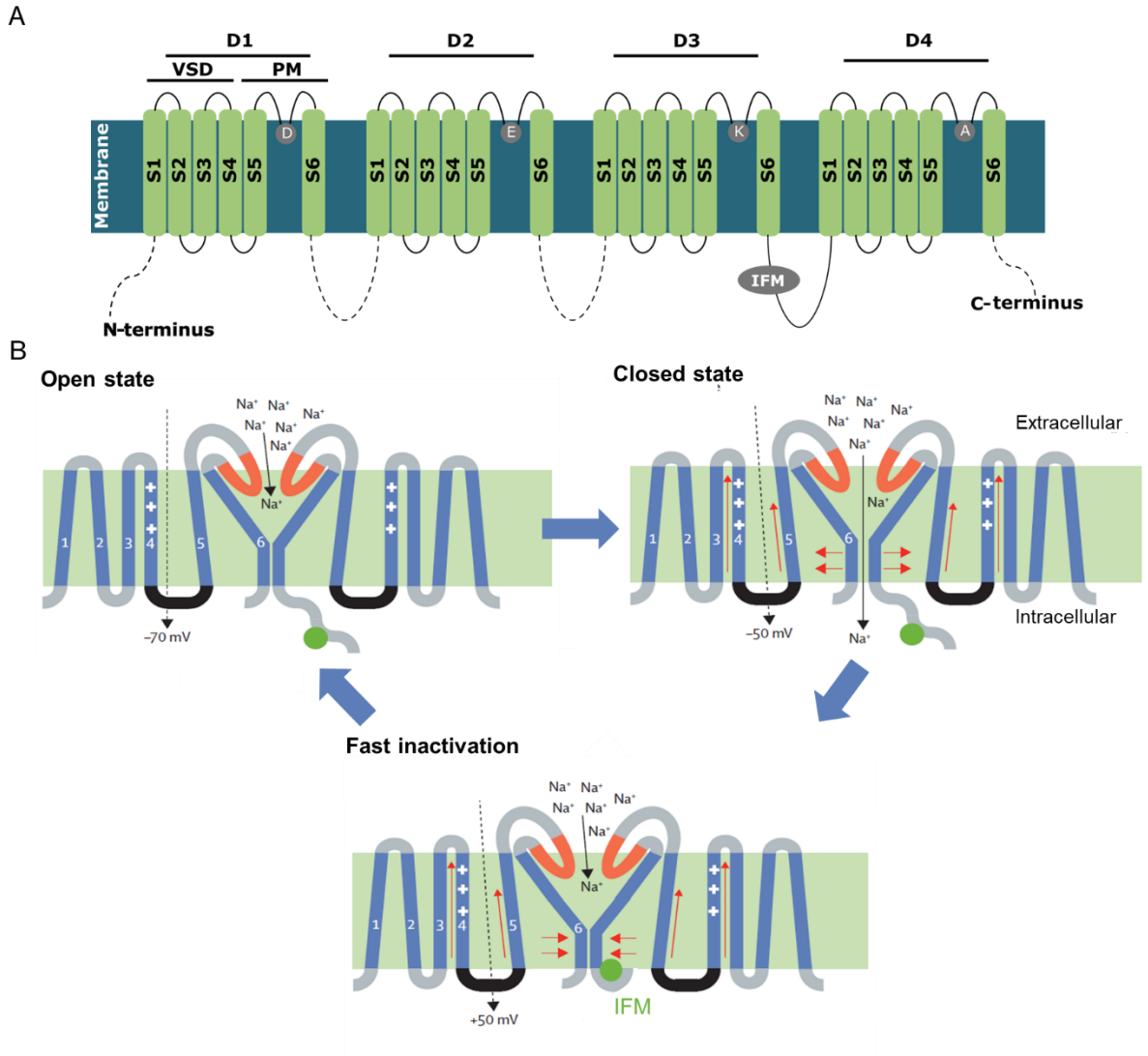

Figure 4 Voltage-gated sodium channel structure and gating. A) 2D structure of the VGSC alpha subunit displaying the four domains (D) with the six transmembrane segments. S1-S4 forms the voltage sensor domain (VSD), S5-S6 forms the pore module (PM). B) Gating of VGSCs shown exemplary in one domain. In the resting state, the pore module is closed. Upon depolarization of the membrane, the positively charged arginine residues in S4 move the voltage sensor upwards, pulling the pore open through the rigid linker between S4 and S5 (black). Na^+ ions can now enter the cell controlled by the selectivity filter (orange). During steady-state fast inactivation, the intracellular inactivation motif (IFM, green circle) moves to the side of the pore and causes it to close. After hyperpolarization of the membrane, the channel returns to its closed state. Figure B adapted from (Bennett et al., 2014).

1.6.2 Subtypes of voltage-gated sodium channels

The VGSC alpha subunits are encoded by the SCN genes. 10 different related alpha subunits exist, resulting in 9 voltage-sensing Na_v channels and one salt-sensing channel called Nax. Na_v alpha subunits differ in their kinetics and expression pattern in the nervous tissue. The channels can be divided into tetrodotoxin-sensitive (TTXs) and tetrodotoxin-resistant (TTXr) channels. Tetrodotoxin can bind to an aromatic residue in the extracellular loop between the S5 and S6 segments in domain 1 in TTXs channels, which blocks the pore. TTXr Na_v channels have a cysteine or serine residue at this position, which reduces the affinity of TTX for this position and thereby decreases the amount of current reduction by TTX to a large magnitude. $Na_v1.5$, $Na_v1.8$ and $Na_v1.9$ are TTXr channels; all other listed Na_vs are TTXs channels (Bennett et al., 2014).

$Na_v1.1$, $Na_v1.2$, $Na_v1.3$, $Na_v1.4$, $Na_v1.5$ and $Na_v1.6$ are primarily expressed in the central nervous system (CNS) and $Na_v1.7$, $Na_v1.8$ and $Na_v1.9$ are preferentially expressed in the peripheral nervous system (PNS) (Bennett et al., 2019; Wang et al., 2017). Despite $Na_v1.5$ usually being referred to as the "cardiac sodium channel", $Na_v1.5$ currents could be recorded in 80 % of neonatal rat DRG neurons (Renganathan et al., 2002). In adult rats, $Na_v1.5$ currents could only be found in 5 % of rat DRG neurons and $Na_v1.5$ mRNA has been detected at low levels in adult mouse DRG neurons (Renganathan et al., 2002; Usoskin et al., 2015). $Na_v1.7$ is predominantly expressed in the PNS, but also in a few distinct regions of the CNS, for example in olfactory sensory neurons. $Na_v1.8$ can mainly be detected in sensory and trigeminal neurons (Bennett et al., 2019). $Na_v1.9$ is preferentially expressed in nociceptors, trigeminal and intrinsic myenteric neurons (Dib-Hajj et al., 2015).

1.6.3 Nav1.9- a special voltage-gated sodium channel

In this thesis, the focus will be on $Na_v1.9$, which presents unique gating characteristics and is the least well-researched Na_v channel. The $Na_v1.9$ protein has the least homology with other Na_v channels (Dib-Hajj et al., 2015). $Na_v1.9$ activates and inactivates at very hyperpolarized potentials compared to other Na_vs. Furthermore, it inactivates very slowly, which creates a persistent current. The overlap between activation and inactivation creates large window currents, where channels may spontaneously or persistently open (Huang et al., 2019; Vanoye et al., 2013; Zhang et al., 2024). These unique gating features indicate that $Na_v1.9$ contributes little to the action potential amplitude but is rather active around the resting membrane potential. This could mean that $Na_v1.9$ acts as a subthreshold channel, whose activity can lower the threshold for action potentials and increase repetitive firing, thus making it a relevant candidate to contribute to sensory neuron over-excitability in neuropathic pain (Dib-Hajj et al., 2015). Furthermore, a recent study employing a Hodgkin-Huxley model based on iPSC-SN data reported a crucial role of $Na_v1.9$ in the generation of the fast action potential upstroke and shoulder (Köster et al., 2025).

$Na_v1.9$ is one of the least well-researched Na_vs due to the difficulty to express this channel in heterologous systems. Therefore, it is largely investigated in rodent DRG neurons. However, human and rodent $Na_v1.9$ only show 75 % genetic sequence homology, which is the highest sequence divergence amongst all VGSCs (Dib-Hajj et al., 1999). In line with this, human and rodent $Na_v1.9$ show differences in channel kinetics. Human $Na_v1.9$ activates and inactivates slower and at more hyperpolarized potentials compared to rat $Na_v1.9$ (Dib-Hajj et al., 2015; Zhang et al., 2024). In addition, human $Na_v1.9$ current was found to be decreased by application of an inflammatory cocktail, whereas rat $Na_v1.9$ current was increased. These results are especially striking in the presumed role of $Na_v1.9$ in inflammatory pain, which is an assumption largely based

on rodent models that may not be true for humans (Zhang et al., 2024). This data indicates that human models are required to study the role of Na_vs, and especially Na_v1.9, in neuropathic pain.

1.7 Neuropathic Pain

After discussing the function and molecular mechanism of nociception in the healthy body, the focus will now turn to diseases in which nociception is dysregulated, resulting in neuropathic pain. Pain is defined as “an unpleasant sensory and emotional experience associated with, or resembling that associated with, actual or potential tissue damage” (Raja et al., 2020). Pain is a complex experience that involves not only the transduction of noxious environmental stimuli, but also cognitive and emotional processing by the brain (Julius & Basbaum, 2001). Perceived pain is dependent on the environmental context, emotional factors, attentional mechanisms and past experiences (Bennett et al., 2014). Pain is essential, as illustrated by people with an inability to feel pain, who frequently suffer from unnoticed severe injuries and have a higher risk of premature death (Leipold et al., 2013). However, if the pain pathways get altered, pain can develop from an acute warning system to a chronic and debilitating disease (Basbaum et al., 2009).
It is important to notice that nociception can trigger pain, but in chronic pain conditions, pain can exist without the presence of an acute noxious stimulus or nociception. Pain is regarded as chronic if it occurs regularly for more than three months (Bennett et al., 2019). In this thesis, the focus will be on chronic pain that originates from the dysfunction of the peripheral nerves, called neuropathic pain. Neuropathic pain is defined as “pain caused by a lesion or disease of the somatosensory nervous system” (International Association for the Study of Pain, 2011). It affects 7-10% of the global population and poses a major clinical burden (Van Hecke et al., 2014). Currently, most available treatments are ineffective, lead to an overall pain relief of only 50 % in half of the patients and often have to be discontinued due to severe side effects (Sopacua et al., 2019). Neuropathic pain can originate from various molecular mechanisms, which are only partially understood yet and present in different symptoms clinically. This thesis will focus on neuropathic pain resulting from changes in the microenvironment of free nerve endings in the skin and variants in VGSCs and highlight two different disease phenotypes that both include nerve sensitization leading to neuropathic pain. To better understand how neuropathic pain develops, one has to understand how nerves can become sensitized in a temporary or chronic manner.

1.7.1 Nerve sensitization in neuropathic pain

Chronic pain can arise from central or peripheral sensitization. In central sensitization, neurons of the central nervous system become hyperexcitable, which enhances the perception of nociceptive signals received from the peripheral nervous system. In peripheral sensitization, the properties of peripheral nerves are altered, which is evident by an alteration in the relationship between stimulus and response. This results in increased responses to subthreshold stimuli, lowered thresholds to thermal or mechanical stimuli or nerve firing in the absence of a stimulus (Bennett et al., 2019). Consequently, a normally innocuous stimulus such as light touch can be perceived as painful, which is called allodynia and a normally painful stimulus can elicit greater pain as usual, which is called hyperalgesia (Basbaum et al., 2009). In addition, during nerve sensitization, the ordinarily mechano-insensitive CMi-fibers can become mechanosensitive, resulting in an increased response to mechanical stimuli (Kleggetveit et al., 2012; Namer & Lampert, 2025).

Peripheral nerve sensitization can occur due to damage of the nerve fiber, changes in the nerve fiber environment or mutations in proteins that are essential in regulating nerve fiber activity (Basbaum et al., 2009). One well-known inducer of nerve sensitization is inflammation, which often occurs after a tissue injury (Basbaum et al., 2009; Julius & Basbaum, 2001). In the healthy human body, the nerve sensitization should resolve as soon as the primary injury has healed. If allodynia or hyperalgesia persists after the injury has healed, nerve sensitization can result in neuropathic pain (Basbaum et al., 2009). In neuropathic pain patients, a large proportion of CMi fibers have been shown to be spontaneously active (i.e., firing in the absence of an input stimulus), correlating with the spontaneous pain of the patients (Kleggetveit et al., 2012; Namer & Lampert, 2025).

1.8 Voltage-gated sodium channel variants in neuropathic pain

Given their essential role in the conductance of neurons, VGSC activity can strongly influence neuronal activity. Altered VGSCs function alters important key parameters such as the action potential threshold, amplitude or the firing frequency and can thereby increase or decrease the response of a neuron to a given stimulus (Bennett et al., 2019). The former is known as nerve sensitization. Nerve sensitization through VGSCs can occur from the action of external factors such as cytokines secreted by keratinocytes or genetic variants in the VGSCs. The increased activity of VGSCs can occur on several time scales. On a short-term time scale, the conductance and amount of VGSCs in the membrane can increase through phosphorylation events, interactions with G-protein coupled receptors and increased trafficking to the membrane. On a longer time scale, the amount of VGSCs can be increased through an increase in mRNA and protein production (Bennett et al., 2014).

Neuropathic pain disorders can be caused by channelopathies in $Na_v1.7$, $Na_v1.8$ or $Na_v1.9$ that are inherited in a Mendelian fashion. These channelopathies can cause various neuropathic pain disorders, including small fiber neuropathy (SFN), inherited erythromelalgia (IEM), familial episodic pain syndrome or paroxysmal extreme pain disorder (PEPD) (Bennett et al., 2019). The severity of pain caused by the Na_v mutations is dependent on the affected region within the channel and the type of mutation. Mutations leading to a change in amino acid polarity within channel regions that are evolutionarily highly conserved are more likely to be pathogenic. Gain-of-function (GOF) mutations in VGSCs can for example result in a hyperpolarizing shift in the voltage of activation, a depolarizing shift in the voltage of slow and fast inactivation, an increase in peak currents or impaired slow inactivation. These GOF mutations mostly lead to an increase in nerve fiber excitability, thereby causing a pain phenotype (Bennett & Woods, 2014). In contrast, loss-of-function (LOF) mutations in $Na_v1.7$ can result in congenital insensitivity to pain (CIP), likely through a decrease in neuronal excitability (Cox et al., 2006). Interestingly, GOF mutations do not always result in increased neuronal excitability. Leipold et al. found the GOF $Na_v1.9$ variant Leu811Pro in a CIP patient that caused a hyperpolarizing shift in channel activation and deactivation kinetics as well as a slowed channel inactivation. The authors suggest that this mutation leads to an increased neuronal activity at the resting state, thereby inactivating other channels such as $Na_v1.7$ and $Na_v1.8$ and causing a conduction block. Thus, despite the GOF mutation, the patient is largely unable to feel pain (Leipold et al., 2013).

What proves challenging in the understanding and treatment of these neuropathic pain disorders is the heterogeneous clinical presentation within the patient population, even between members of the same family with identical channelopathies (Mis et al., 2019). Certain variants, such as I228M in $Na_v1.7$, can result in either SFN or IEM, with varying levels of facial pain within affected

families (Estacion et al., 2011). Therefore, advanced cellular models are required that not only model the channelopathy but also recapitulate the full phenotype of the patient, including all support proteins that may influence the Na_v channels and neuronal excitability.

1.9 Small fiber neuropathy

Small fiber neuropathy (SFN) is characterized by the dysfunction and/or degeneration of the thinly myelinated Aδ- or unmyelinated C-fibers. Patients suffering from SFN report burning, stabbing, and electrifying pain sensations on the skin, often localized in the hand or feet. Additional SFN symptoms include 'positive' symptoms such as allodynia, dysesthesia, hyperesthesia, itch, paraesthesia and 'negative' symptoms such as hypoesthesia for heat or light touch, numbness or reduced sensation to sharp stimuli. As Aδ- and C-fibers not only innervate the skin but also the internal organs, additional symptoms include dry eyes and mouth, reduced sweating, orthostatic dysfunction or gastrointestinal dysfunction (Gross & Üçeyler, 2020; van den Braak et al., 2025). Underlying etiologies for SFN can be hereditary (see above), metabolic, immunological, toxic, infectious or paraneoplastic (Gross & Üçeyler, 2020). The disease is diagnosed through clinical evaluation of the patient's symptoms and quantitative sensory testing (QST), in which the sensory thresholds for pain, touch, vibration and temperature are determined. Furthermore, a reduced intraepidermal nerve fiber density (IENFD) in skin biopsies is frequently observed and therefore evaluated for the diagnosis of SFN (Gross & Üçeyler, 2020). Although the reduction of IENFD seems counterintuitive to the pain phenotype of the patients at first, it has been proposed that the enhanced activity of VGSCs in the hyperexcitable nerve fibers of SFN patients would lead to an increased sodium concentration in the neurons, which could reverse the operation of the sodium-calcium exchanger protein, resulting in increased intra-axonal calcium concentration. Thereby, calcium toxicity could cause axonal degradation (Estacion et al., 2015). However, a reduced IEFND is not present in all SFN patients, and therefore, this diagnostic test should be viewed as supplementary but not conclusive for diagnosing the disease (Lauria & Lombardi, 2012).
Variants in peripheral VGSCs are frequently found in SFN patients. In a large cohort study, 393 patients with idiopathic SFN were tested for variants in the genes encoding $Na_v1.7$ (Faber, Hoeijmakers, et al., 2012), $Na_v1.8$ (Faber, Lauria, et al., 2012) or $Na_v1.9$ (Huang et al., 2014). Of these 393 patients, 34 showed variants in SCN9A ($Na_v1.7$), 15 presented variants in SCN10A ($Na_v1.8$) and 8 were found to have variants in SCN11A ($Na_v1.9$). In total, more than 15 % of the tested patients showed variants in one or two of the peripheral Na_vs. A subset of identified variants was functionally characterized using electrophysiology recordings in heterologous expression systems and rodent DRG neurons. An overview of published variants is provided in Table 1.

Table 1 Overview of published variants in $Na_v1.7$, $Na_v1.8$ and $Na_v1.9$ in SFN patients. Increased neuronal excitability *in vitro* was considered confirmed when the variants caused a gating shift in heterologous systems and increased the firing behavior in rodent DRG neurons. Variants from (D. Bennett et al., 2019; Faber, Hoeijmakers, et al., 2012; Faber, Lauria, et al., 2012; Huang et al., 2014; Namer et al., 2019).

***Na_v* channel**	**Variants**	**Increased neuronal excitability *in vitro***
$Na_v1.7$	R185H, D623N, I739V, I720K, M1532I, M923L+V991L, I228M	I720K, D623N, M923L+V991L
$Na_v1.8$	L554P, C2816T, A2819T, G3166A, A1304T, G4568A, G4984A, G1662S, I1706V	A1304T, L554P, G1662S, I1706V
$Na_v1.9$	I381T, K419N, A582T, A681D, A842P, L1159P, Phe1689L, I381T, L1158P, N1169S	L1158P, I381T

1.9.1 Two small fiber neuropathy patients carrying a Y66S variant in $Na_v1.9$

Recently, two patients diagnosed with SFN were identified carrying the novel variant p. Y66S in $Na_v1.9$ (van den Braak et al., 2025). Patient Y66S_1 is the mother of patient Y66S_2. Patient Y66S_1 first developed pain symptoms at 53 years of age (Figure 5A). She reported needle-like, pricking sensations and burning pain in both feet. During her first five years of symptoms, the burning pain spread from the feet to the hips and from the hands to the shoulders. Her pain was quantified as 4/10 on the numeric pain rating scale. In addition to the neuropathic pain, she also reported paresthesia (constant prickling), a vibrating sensation of different body parts and episodic sensations of cold in the entire body. She presented with numbness in her feet, hypoesthesia for hot stimuli, reduced perception of light touch on the right bodyside and occasional dizziness. Nerve conduction studies showed no involvement of large fibers and a skin biopsy revealed a reduced IEFND.

Patient Y66S_2 reported the onset of symptoms at age 27 years. However, he did not experience neuropathic pain. He was still diagnosed with SFN due to the following symptoms. At his first examination at age 31, he reported numbness in both feet, paresthesia in feet and hands, restless legs and a persistent cold feeling in hands and feet, even when the extremities were warmed up. Upon examination, a reduced perception of touch and cold in his left arm and both feet, decreased pinprick discrimination in his right foot and thermohypoesthesia in his fingers and feet were found. In QST, significant dysfunction of the Aδ- and C-nerve fibers was found. No signs of larger fiber neuropathy, nerve conduction abnormalities or changes in IENFD were found. The patient had been treated for neuroblastoma at the age of 1 year with surgery and cytostatics, but related documents were not available. It should be noted that cytostatic agents can lead to neuropathic pain (Sisignano et al., 2014). Otherwise, no indication of an acquired SFN, such as autoimmune disorders or vitamin deficiencies, could be found. Importantly, over the course of 26-66 months after initial examination, the symptoms of both patients exacerbated (van den Braak et al., 2025)

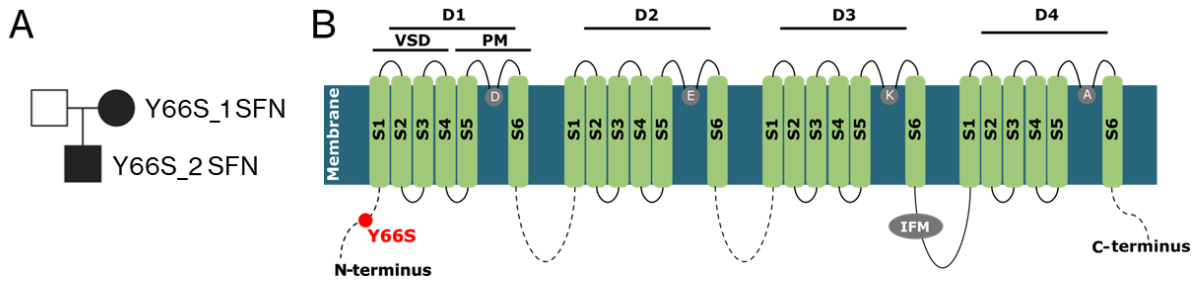

Figure 5 The $Na_v1.9$ variant Y66S. A) Family pedigree of two related small fiber neuropathy (SFN) patients carrying a Y66S variant in $Na_v1.9$. B) Location of the Y66S mutation in N-terminus of the $Na_v1.9$ channel structure (marked in red). D=Domain, VSD= voltage sensor domain, PM= pore module.

The Y66S variant was identified as likely pathogenic and no additional pathogenic or likely pathogenic variants were detected in other sensory disorder-associated genes (van den Braak et al., 2025). The variant is located in the N-terminus of $Na_v1.9$, slightly upstream of the first transmembrane domain (Figure 5B). The tyrosine residue that is switched to a serine residue is conserved through species and across all nine human Na_v channels. The functional characteristics of the Y66S variant were investigated in murine $Na_v1.8$/$Na_v1.9$-k.o. DRG neurons transfected with a $Na_v1.9$-WT or Na1.9-Y66S plasmid. It was found that the variant caused a mix of a gain- and loss-of-function phenotype, with a reduced inward current density, a depolarizing shift of the voltage of activation and steady-state fast inactivation and slower activation and inactivation kinetics compared to the WT channel. The action potential width was decreased and the action potential afterhyperpolarization was more negative in the variant compared to the WT, whereas the RMP, the action potential voltage threshold and amplitude and the mean firing rate were not affected (van den Braak et al., 2025). However, these findings are based on expressing human $Na_v1.9$ in a murine rodent model and need to be validated in a human sensory neuron model. The present thesis addresses this gap by investigating the potential effect of the $Na_v1.9$-Y66S variant in a human model.

1.10 The role of keratinocytes in neuropathic pain

Mechanosensation and nociception in the skin have long been thought of as a task solely carried out by free nerve endings and their associated receptors. It was thought to be a neural process, while the skin was thought of as the organ that merely harbours the mechanoreceptors and free nerve endings. However, in the last two decades, researchers discovered that the keratinocytes in the epidermis play an essential role in touch and pain perception (Talagas et al., 2020a).

Keratinocytes are located between the environment and the sensory neurons and are therefore ideally located to transmit environmental stimuli to sensory neurons. Keratinocytes 1) express sensory receptors activated by noxious stimuli, 2) can release various neuroactive substances, and 3) can specifically activate nociceptive sensory neurons to elicit pain. Keratinocytes express the TRP channels TRPV1, TRPV3, TRPV4, TRPM8 and TRPA1, which are involved in nociception (Talagas et al., 2020a). Furthermore, they express VGSCs. Keratinocytes are unable to generate action potentials, but the VGSCs in keratinocytes may be involved in the release of ATP, which can directly bind to the P2X receptors on neurons and activate them (Zhao et al., 2008).

Keratinocytes can release many neuroactive molecules, including neurotrophins, neurotransmitters or cytokines (Talagas et al., 2020a). Structurally, it has been shown *in vitro* that human keratinocytes attract the neurite growth of mouse DRG neurons and human neurons

differentiated from neural crest cells. Human fibroblasts did not attract neurites (Kreß et al., 2023; Krishnan-Kutty et al., 2017). Additionally, there is evidence that keratinocytes and sensory neurons form sensory synapses *in vitro* and *in vivo* (Talagas et al., 2020b). Functionally, keratinocytes depolarize and release calcium ions upon mechanical probing *in vitro* (Moehring et al., 2018; Tsutsumi et al., 2009). Upon mechanical stimulation, they also release ATP, which binds to the P2X receptor on sensory neurons and elicits action potential firing *ex vivo* (Moehring et al., 2018). In line with these results, mechanical or chemical stimulation of keratinocytes adjacent to sensory neurons evoked calcium currents in sensory neurons *in vitro* (Klusch et al., 2013; Talagas et al., 2020b).

The above-described studies show that keratinocytes are in close contact with sensory neurons and can activate them, but the question remained how much they contribute to mechanosensation and nociception *in vivo*. To determine whether keratinocytes and not only mechanoreceptors surrounding free nerve endings activate sensory neurons, *in vivo* rodent studies have been performed where keratinocytes were selectively activated or inhibited. It has been shown that cutaneous application of capsaicin in mice expressing TRPV1 solely in keratinocytes induced nocifensive behaviour (Caterina & Julius, 2001). Furthermore, focused optogenetic activation of keratinocytes elicited action potentials in cutaneous sensory neurons *ex vivo* and nocifensive responses *in* vivo (Baumbauer et al., 2015; Moehring et al., 2018). These findings have been supported by another mouse model in which the optogenetic inhibition by hyperpolarization of keratinocytes decreased behavioral and cellular mechanosensitivity (Moehring et al., 2018). Keratinocytes may be viewed as primary nociceptive transducers and may therefore be relevant in neuropathic pain. However, the role of keratinocytes in skin diseases involving neuropathic pain, such as pachyonychia congenita, is poorly understood.

1.11 Neuropathic pain in Pachyonychia congenita

Pachyonychia Congenita (PC) is a rare autosomal genodermatosis caused by mutations in one of the five keratin genes KRT6A, KRT6B, KRT6C, KRT16 or KRT17. Patients with PC suffer from severe plantar pain, plantar hyperkeratotic calluses and hypertrophic nail dystrophy. Additional clinical features can include itch, neurovascular structures, oral leukokeratosis or epidermoid cysts (Mccarthy et al., 2023). The exact prevalence for PC is unknown, but the Pachyonychia congenita research & patient support project reported a total of 1038 cases as of January 2021 (Pachyonychia Congenita Research & Support Project, 2021). Of the 5 keratins that can be mutated, mutations in Krt6 and Krt16 are most frequently reported and cause severe phenotypes. 20 % of patients with PC-Krt6 or PC-Krt16 have to use walking aids due to the physical limitations caused by the disease (Samuelov et al., 2020b).

Keratins are intermediate filaments that play an essential role in the organization of the cytoskeleton and thereby provide structural support and mechanical resilience to the cell (see section 1.4). Furthermore, they are involved in immune response and wound healing processes. Krt6, Krt16 and Krt17 are often referred to as “stress-keratins”, due to their role in the process of damage regeneration. These keratins are not found in intact normal interfollicular epidermis, but are highly expressed in injured skin (Romanshin et al., 2024). Mutations in keratins are presumed to result in an abnormal structural network and alteration in keratin-linked signals, thus resulting in an uncontrolled proliferation of keratinocytes (Arin, 2009; Moll et al., 2008). However, the molecular mechanism linking the keratin mutations to the plantar hyperkeratotic calluses and the severe neuropathic plantar pain remains poorly understood.

Severe plantar pain is the major complaint of patients suffering from PC (Pan et al., 2016). In a large case-cohort study, over 60 % of patients reported pain sensation and 24.6 % reported having to take pain medication regularly due to the plantar pain (Samuelov et al., 2020). In a different study, 9 out of 10 patients reported that the pain affects their daily life and walking (Pan et al., 2016). The pain has been described as both nociceptive and neuropathic (Mccarthy et al., 2023). Despite common belief, shaving of the plantar callus only partially alleviates the pain in PC patients. Additionally, intraepidermal nerve fiber density has been shown to be reduced in the PC-affected regions of the patients compared to the unaffected regions (Pan et al., 2016). Cao et al. found that 12 pain-related genes were upregulated in PC-affected skin compared to unaffected skin, including SPRR1A, KLK10 and RGS20 (Y. A. Cao et al., 2015). These findings indicate neuropathic changes of the nervous system. However, the molecular pathology of pain in PC patients is still unknown and most of the above-mentioned studies are limited by a small patient sample size. Therefore, more research is required to validate and understand the pathology of pain in PC patients. Improvement of our understanding of the underlying disease mechanism may ultimately result in improved patient care, as there is currently no cure or specific treatment of PC (Mccarthy et al., 2023). While PC is generally viewed as a skin disease, the previous paragraphs show that a nerve fiber involvement in this disease is likely, resulting in neuropathic pain.

1.12 Modelling neuropathic pain *in vitro*

Modelling neuropathic pain *in vitro* is a complex endeavor, as neuropathic pain is influenced by many cell types and is composed of the pain signal in the PNS and the interpretation of the pain signal in the CNS. In this thesis, the focus will be on two different angles of neuropathic pain. The first one is nerve fiber sensitization generated within the peripheral neuron caused by mutations in VGSCs. The second one is nerve fiber sensitization by surrounding cells; in this case, we will focus on keratinocytes. We will begin with the summary of models for neuropathic pain that focus on VGSCs and then continue with models for neuropathic pain influenced by keratinocytes.

1.12.1 Induced pluripotent stem cell-derived sensory neurons

Traditionally, VGSCs have been studied in heterologous expression systems or rodent DRG neurons. Heterologous expression of VGSCs is frequently performed in Human Embryonic Kidney 293 (HEK-293) cells, human neuroblastoma SH-SY5Y cells or ND7/23 cells, which are a fusion cell-line of embryonic rat DRG neuron and a mouse neuroblastoma cell line. These cell lines express only certain VGSCs, if any, and can therefore be transfected with plasmids carrying different VGSC alpha and/or beta units, allowing for the specific study of VGSCs in isolation. This has resulted in valuable insights about the intrinsic channel properties and gating. However, these studies do not reflect the behavior of the channel in its native cell background (Labau et al., 2022). It has been established that the gating properties of VGSCs are dependent on the presence of auxiliary subunits, post-translational modifications, the cellular environment, including membrane composition, and signaling pathways activation for example through kinases (Ahern et al., 2016). Rodent DRG neurons offer the possibility to study VGSCs in the presence of all cellular factors that can influence their gating. However, rodent and human VGSCs differ in their gating kinetics and expression patterns (Han et al., 2015; Zhang et al., 2024) and comparative transcriptome analyses showed that of the human DRG genes, only 50–70% were expressed in mice (Labau et al., 2022). While human DRG neurons would be the ideal cellular platform to study human Na_v channels in their native surrounding, the availability of these cells is sparse and

determined by hard-to-predict donor availability. In addition, hDRG neurons are rarely available from neuropathic pain patients and are therefore of only partial use in neuropathic pain research. With the stated limitations of the previously used system, a new cellular system was required to study VGSCs in a human system that would include all Na_v alpha subtypes, auxiliary subunits, proteins responsible for post-translational and signaling modifications and have the patient's phenotype. Therefore, researchers have begun to study VGSCs in human stem cell-derived sensory neurons.

The invention of induced pluripotent stem cells (iPSCs) has revolutionized biomedical research (Takahashi et al., 2007; Takahashi & Yamanaka, 2006). IPSCs can be generated from various types of somatic cells, such as peripheral blood mononuclear cells (PBMCs) or fibroblasts, by overexpression of the transcription factors OCT4, SOX2, KLF4 and c-MYC in the cells (Robinton & Daley, 2012). As defined in the name, iPSCs are pluripotent and can develop into any cell type of the mesoderm, endoderm or ectoderm, while maintaining the patient's genotype at the same time (Lampert et al., 2020; Robinton & Daley, 2012). This allows for the modelling of complex disease phenotypes without additional genetic engineering. Furthermore, in comparison to genetically edited cell lines, iPSCs will not harbour only the disease-causing variants, but all variants that the patients carry, including ones that are not known to be relevant to the phenotype yet. In addition to disease modelling, iPSC-derived sensory neurons (iPSC-SN) provide the ideal platform for drug screening and personalized medicine to achieve better treatment of patients with neuropathic pain.

1.12.2 iPSC-SN protocols model *in vivo* embryogenesis

Various protocols have been published in the last two decades to obtain sensory neurons from iPSCs. These protocols aim to recreate the signaling pathways occurring during human embryogenesis, which will shortly be summarized here. Neural crest cells are multipotent neuroectodermal cells that give rise to neurons and glia of the peripheral nervous system, sympathoadrenal cells, cardiac cells, melanocytes, and most of the bone and cartilage of the face and skull (Stuhlmiller & García-Castro, 2012). During embryonic development, neural crest cells reside within the neural plate border, which is located between the neural plate and the non-neural ectoderm. As neurulation proceeds, the neural plate invaginates and the neural tube closes. Afterwards, the neural crest cells lose their intracellular connections and undergo epithelial-to-mesenchymal transition (EMT), followed by their delamination from the neural tube and migration to different niches of the embryo (Simões-Costa & Bronner, 2013).

In the development of neuroectoderm, neural crest cells and sensory neurons, three signaling pathways are especially important: the WNT-signaling, the SMAD2/3 signaling and the bone morphogenetic protein (BMP) signaling (Raible & Ragland, 2005; Smith et al., 2008). The WNT-signal gradient is essential for the rostro-caudal regionalization of the neural tube into the forebrain, midbrain, hindbrain and spinal cord. Active WNT-signaling induces the delamination of the neural crest cells from the neural tube through the modulation of cell division. Inhibition of WNT signaling during early development blocks neural crest cell formation and enhances forebrain precursor cell development. Furthermore, active WNT signaling is essential for the further development of sensory neurons from neural crest cells (Raible & Ragland, 2005). Inhibition of the SMAD2/3 signaling in the ectoderm through factors secreted from the underlying mesoderm facilitates neuroectoderm formation (Smith et al., 2008). BMP signaling plays an interesting and somewhat contradictory role in neural crest development. On the one hand, it has been found to regulate the EMT transition, delamination and migration of neural crest cells. At the

same time, it induces the formation of non-neuronal ectoderm. Research insights of the last decade suggest that since the neural crest cells form at the interface between medial and lateral tissues, an intermediate level of BMP signaling is likely required for neural crest cell induction. It has also been proposed that during gastrulation, a partial or complete inhibition of BMP signaling is adequate to create a "competency zone" for other signals like WNT to specify the neural crest cell lineage (Stuhlmiller & García-Castro, 2012). Importantly, BMP and WNT signaling can act both synergistically or inhibitory, depending on the multitude of other signaling cascades, e.g., the SMAD2/3 signaling (Kléber et al., 2005; Zechner et al., 2007). In recent years, another important aspect of neuronal development has become evident: Mechanobiology and tissue stiffening. Barriga et al. found that the head mesoderm stiffens during morphogenesis and that this process is essential to initiate the EMT transition of the neural crest cells and triggers their migration (Barriga et al., 2018).

After the formation of neural crest cells, sensory neurons can arise through a process of increasingly restrictive gene expression. Two crucial transcription factors in the development of sensory neuros are Neurogenin (NGN) 1 and 2. It was initially believed that these two transcription factors are expressed in two distinct periods, overlapping with the two waves of large-and small-diameter sensory neuron generation (Ma et al., 1999). However, new insights are challenging this hypothesis (Meltzer et al., 2021). Recent studies have suggested that all DRG neuron subtypes arise from newborn neurons expressing both NGN1 and NGN2 and that their subtype specification occurs after these expression waves (Faure et al., 2020; Sharma et al., 2020). In addition, the transcription factors Islet1 and Brn3a have been found to play a role in the establishment of sensory neuron fate (Lanier et al., 2009; Sun et al., 2008).

As this short summary of embryonic neurogenesis demonstrates, the generation of sensory neurons from stem cells is a complex process. There are many protocols available to generate sensory neurons from iPSCs. Here, I will focus on the three protocols that have been employed for this thesis. Notably, most protocols refer to the generated cells as iPSC-nociceptors, but as will be discussed in later sections of the introduction, the functional nociceptor identity of these cells has not been fully validated yet, and therefore, they will here be referred to as iPSC-SN.

The first and probably most well-known protocol to generate sensory neurons from iPSCs was published in 2012 by Chambers *et al.* and uses a cocktail of small molecules to define cell fate. This protocol initiates neuralization of the iPSCs by dual-SMAD inhibition from LDN-193189 and SB431542. Further differentiation into post-mitotic neurons is performed by SU5402, CHIR99021 and DAPT. SU5402 inhibits the vascular epithelial growth factor (VEGF), the fibroblast growth factor (FGF) and the platelet-derived growth factor (PDGF) tyrosine kinase signaling. CHIR99021 acts as a WNT-signaling agonist and DAPT blocks Notch-signaling. After 10 days, the cells should have obtained a post-mitotic neuronal identity and are then maintained in media containing NGF, BDNF and GDNF for maturation into sensory neurons (Chambers et al., 2012).

More recently, differentiation protocols have been developed that initiate differentiation via overexpression of transcription factors crucial for neuronal induction. In the protocol of Schrenk-Siemens *et al*. NGN1 is overexpressed in neural crest cells (Schrenk-Siemens et al., 2022). NGN1 is introduced into the neural crest cells by transfection of a lentivirus carrying the coding sequence of NGN1 under the control of a TET-ON promoter. After 10 days of NGN1 forced over-expression, the immature neurons are maintained in maturation media containing NGF, BDNF and GDNF. This protocol will later be referred to as the NGN1-protocol.

In an alternative genetic engineering approach, Röderer et al. developed a protocol in which a doxycycline-inducible expression cassette encoding the transcription factors NGN1, BRN3A and ISLET1 (later referred to as the 'NBI' protocol) is inserted into the AAVS1 locus of iPSCs. Guided by

doxycycline, the 'NBI' transcription factors are overexpressed for seven days in iPSCs. This generated immature sensory neurons, which are then matured in media containing NGF, BDNF, GDNF and NT-3 (Röderer, 2021).
The available data of all three described protocols show evidence of successfully generated iPSC-SN. This conclusion is based on immunostainings for different sensory neuron markers such as TUJ1 or TRKA, mRNA levels of sensory neuron markers and ion channels and on electrophysiological data. Importantly, the term 'mature iPSC-SN' is used differently by different authors and is occasionally used prematurely. A mature iPSC-SN should model native human DRG neurons as closely as possible in terms of morphology and function, including the generation of mature action potential, functional presence of VGSCs, calcium and potassium channels and responsiveness to chemical and mechanical triggers.

1.12.3 Modelling VGSCs variants linked to neuropathic pain in iPSC-SN

The functional presence of the peripheral VGSCs $Na_v1.7$, $Na_v1.8$ and $Na_v1.9$ is a hallmark of nociceptor identity. This can be assessed with patch clamp, a method in which either a voltage can be applied and the ion current flowing through the channels can be measured (voltage clamp) or a current can be applied and the change in membrane voltage, e.g., an action potential, can be measured (current clamp). It is essential to determine the presence of VGSCs this way, as available antibodies to label VGSCs have proven unreliable due to the close structural difference between the different channel subtypes. For example, Kathrin Dams (Master student, Institute of Neurophysiology, Uniklinik RWTH Aachen, Germany) has shown that $Na_v1.9$ antibodies from Abcam show a bright positive signal in ND7/23 cells, which should have almost no or no $Na_v1.9$ endogenous channels (unpublished data) (Lee et al., 2019). Most published papers include a quantification of mRNA of TTXr-channels. However, between the presence of mRNA and a functional ion channel in the membrane lie multiple processes, including the translation of the mRNA, post-translational modifications, transport and interaction in the membrane with other proteins. Thus, the presence of mRNA gives limited insights into the functional presence of an ion channel in a cell. In this thesis, the focus will therefore be on the electrophysiological analysis of the TTXr-Na_v channels.
To this end, multiple electrophysiological and/ or pharmacological methods can be applied. Recordings of single TTXr Na_v subtypes will be performed in voltage clamp in the presence of 300-500 nM TTX in the bath solution. As described at length in section 1.4.1.3/4, the TTXr $Na_v1.8$ and $Na_v1.9$ show very different gating properties, with $Na_v1.9$ activating and inactivating at more hyperpolarized potentials with a much slower fast inactivation. These differences in gating kinetics can be used to separate the currents of the two channels from one another. The most used protocol will here be referred to as the TTXr-$Na_v1.9^{inact}$ protocol and was first published by Cummins et al. (Cummins et al., 1999). In this protocol, neurons are first held at a voltage of -100 mV, followed by a series of test pulses to incrementally increasing voltages to measure the total TTXr current. Afterwards, the neurons are held at -60 mV to inactivate $Na_v1.9$ but leave the $Na_v1.8$ current intact and the same series of test pulses was applied. When subtracting the current of the second protocol from the first protocol, a pure $Na_v1.8$ current should remain. This $Na_v1.8$ current can then be subtracted from the total TTXr current to obtain a pure $Na_v1.9$ current. Another possible protocol to isolate $Na_v1.9$ from $Na_v1.8$ current was published by Leipold et al. This protocol uses fluoride in the pipette solution and a series of hyperpolarized incrementally increasing voltage steps until -67 mV. Intracellular application of fluoride has been shown to shift the activation and inactivation of $Na_v1.9$ but not $Na_v1.8$ to more hyperpolarized potentials,

allowing for the measurement of only $Na_v1.9$ at a range of hyperpolarized potentials (Coste et al., 2004). To further enhance the detection of $Na_v1.9$ current, known $Na_v1.9$ current enhancers such as prostaglandin E2 (PGE2), cromolyn sodium or GTP-y-S can be applied (Baker et al., 2003; Rush & Waxman, 2004)(unpublished data of Margaux Theys, Molecular Physiology and Neurophysics group, University of Ghent, presented 2023 at the annual meeting society of general physiologists). Alternatively to electrophysiological protocols, $Na_v1.9$ and $Na_v1.8$ currents can also be separated by selective blockers. In the last decades, multiple $Na_v1.8$ blockers have been developed, but for most blockers, the evidence that $Na_v1.9$ is unaffected by the blockers was not available. In 2006, the conotoxin MrVIB was published, which selectively blocks $Na_v1.8$ but not $Na_v1.9$ in mDRG neurons (Ekberg et al., 2006). However, this toxin is rare and expensive to isolate and therefore, the recently published $Na_v1.8$ blocker Suzetrigine (VX-548) is a promising alternative (Osteen et al., 2024). For this blocker, it has been shown in heterologous expression systems that it is more than 30000 times more selective for human $Na_v1.8$ than other Na_v isoforms.

Most iPSC-SN studies focusing on VGSC channelopathies have investigated $Na_v1.7$ mutations. It has been shown in high-resolution imaging of iPSC-SN carrying a HA-tagged $Na_v1.7$ channel that robust surface expression of $Na_v1.7$ can be observed from day 49 of differentiation onwards (Y. Liu et al., 2024). In terms of disease modelling, $Na_v1.7$ channelopathies in iPSC-SN of IEM patients have been investigated in various studies (Alsaloum et al., 2023; L. Cao et al., 2016; Meents et al., 2019; Mis et al., 2019; Yuan et al., 2021). Cao et al. saw a correlation trend between the pain intensity of the patients carrying a Nav1.7 variant and the excitability of the corresponding iPSC-SN (L. Cao et al., 2016). Interestingly, Mis et al. presented a mother with severe pain and a son with mild pain that both carried the $Na_v1.7$-S241T mutation and showed that the iPSC-SN of the mother were more hyperexcitable than those of the son, while both were more active than the iPSC-SN from the unaffected father (Mis et al., 2019). In addition to disease modelling of IEM in iPSC-SN, the cells have also been used to model CIP. IPSC-SN of CIP patients carrying $Na_v1.7$ mutations showed to be much less responsive to depolarizing stimuli (Mcdermott et al., 2019). These studies highlight the usage of iPSC-SN for the study of $Na_v1.7$ variants in neuropathic pain diseases.

In comparison, the presence of the peripheral TTXr channels $Na_v1.8$ and $Na_v1.9$ in iPSC-SN is highly discussed in the field. Multiple studies found TTXr currents in iPSC-SN, but it remains unclear if they can be assigned to $Na_v1.8$ or $Na_v1.9$, or if they could stem from $Na_v1.5$ (Chambers et al., 2012; Meents et al., 2019; Wainger et al., 2015). Alsaloum et al. found virtually no levels of $Na_v1.8$ or $Na_v1.9$ mRNA in their iPSC-SN and in line with that, the observed TTXr current behaved like $Na_v1.5$, but not $Na_v1.8$ or $Na_v1.9$ (Alsaloum et al., 2021). A different study also found that the TTXr current in iPSC-SN appears to be $Na_v1.5$ to a large extent (Eberhardt et al., 2015). There are, however, two studies published that show evidence for the presence of $Na_v1.8$ and $Na_v1.9$ in iPSC-SN. The first one by Namer et al. found an increased firing frequency and spontaneous activity in the iPSC-SN of an SFN patient with a R923H variant in $Na_v1.8$ and a N1169S variant in $Na_v1.9$ compared to the iPSC-SN of two healthy, age-matched controls (Namer et al., 2019). It is unclear if the observed phenotype results from the Na_v variants, as the $Na_v1.9$ N1169S variant is frequently found in healthy control patients and the $Na_v1.8$ R923H variant did not alter the channel function in a heterologous expression system.This paper did not evaluate the TTXr current in the iPSC-SN to conclusively show the presence of $Na_v1.9$ TTXr currents. Such $Na_v1.9$-

like current traces were shown in a study by Wainger et al., where the sensor neurons were transdifferentiated directly from fibroblasts (Wainger et al., 2015). Unfortunately, there was only one representative trace provided that indicated the presence of a $Na_v1.9$-like persistent current, which was not visible in other TTXr representative current traces and was not further analyzed or quantified. To this author's best knowledge, there is no further publication by this or another research group validating these findings. Therefore, the presence of functional $Na_v1.8$ and $Na_v1.9$ currents in iPSC-SN remains uncertain. Closing this research gap is essential to determine the quality of iPSC-SN as a model for native DRG neurons.

1.12.4 Modelling the role of keratinocytes in neuropathic pain *in vitro*

Neuropathic pain is one of the primary symptoms of patients suffering from Pachyonychia congenita (PC). Furthermore, research of the last decades has revealed an essential role of keratinocytes in nociception and neuropathic pain. However, the molecular mechanism by which the mutations in keratins could result in an altered excitability of nerve fibers is unknown and has not been the focus of published research. Here, we suggest that the keratinocytes carrying the keratin mutations secrete an altered amount of neuroactive factors (such as cytokines) following mechanical stress and could thereby sensitize the sensory neurons.

Various studies have shown that mechanical stress, in particular compression and stretch, induces keratinocytes in monolayers and skin equivalents to secrete cytokines. Bronneberg *et al.* showed that static compression of epidermal equivalents for 24 h at 75 mmHg increases the release of IL-1 and IL-8 (Bronneberg et al., 2007). In a follow-up study, the group showed that IL-1 and IL-8 protein levels are already significantly increased after 1 h of compression, whereas TNF-α is significantly increased after 4 h of compression (Cornelissen et al., 2009). Cyclic stretch for 24 h at 20 % and 0.2 Hertz resulted in increased mRNA and protein levels of IL-1, IL-6, IL-23, TNF-α, CXCL1 and CXCL20 in human primary keratinocytes (Qiao et al., 2019). Similarly, 5 % and 10% cyclic stretch for 6 h at 0.5 Hz increased the IL-6 protein levels in HaCaT cells (Oh et al., 2019). Implantation of expanding dilators into rodents *in vivo* also resulted in an increase in cytokine mRNA and protein levels, including IL-6, IL-23 and TNF-α (W. Liu et al., 2021; Qiao et al., 2019). Interestingly, Liu et al. found that rat scalp expansions lead to downregulation of the genes for the alpha subunits of $Na_v1.1$, $Na_v1.2$, $Na_v1.4$ and $Na_v1.8$ (W. Liu et al., 2021). These studies show coherently that mechanical cyclic and static stretch and static compression induce cytokine upregulation in keratinocytes. However, there are no studies at this time point that investigated whether this upregulation of cytokines in keratinocytes in response to mechanical stress is increased in keratinocytes of PC patients and whether this could be the missing link between the keratin mutations and the symptom of neuropathic pain. Therefore, I aimed to investigate this research gap within this doctoral thesis.

2 Aim of the thesis

Neuropathic pain can arise from intrinsic changes within peripheral neurons or from alterations in their environment. This thesis addresses both origins of neuropathic pain through two complementary projects: one focused on voltage-gated sodium channels (Na_vs) that are key components of neuronal excitability, and the other on keratinocytes, which interact closely with sensory neurons in the skin and influence their activity via direct signaling and secretion of neuroactive substances.

Within the peripheral neuron, Na_vs play a key role in neuronal excitability by initiating, generating and propagating action potentials. The $Na_v1.7$, $Na_v1.8$, and $Na_v1.9$ subtypes are preferentially expressed in peripheral neurons and are critical markers of sensory neuron identity. $Na_v1.8$, $Na_v1.9$ and $Na_v1.5$ are resistant to the Na_v-channel blocker tetrodotoxin (TTXr), allowing their current to be distinguished electrophysiologically from the remaining Na_v subtypes. Genetic variants in $Na_v1.7$, $Na_v1.8$ and $Na_v1.9$ have been associated with altered pain perception, ranging from congenital insensitivity to pain to chronic neuropathic pain.

Induced pluripotent stem cell-derived sensory neurons (iPSC-SN) represent a powerful model to study patient-specific Na_v channel variants in human neurons. However, the functional expression of $Na_v1.8$ and particularly $Na_v1.9$ in iPSC-SN remains uncertain, questioning the suitability of iPSC-SN for disease modelling. $Na_v1.9$ remains the least well-researched Na_v subtype as it is difficult to express heterologously. A deeper understanding of $Na_v1.9$ in human neurons could illuminate its role in neuronal excitability and diseases. We were able to obtain iPSC from two neuropathic pain patients carrying a $Na_v1.9$-Y66S variant that has not been characterized in human neurons before.

Therefore, the aims of the first project were to

- Functionally characterize the TTXr current and its individual Na_v components in iPSC-SN generated by three distinct differentiation protocols
- Develop a method for isolating $Na_v1.9$ current and assess its functional expression in iPSC-SN
- Compare the excitability and firing patterns in iPSC-SN from healthy controls and the pain patients carrying the $Na_v1.9$_Y66S variant
- Assess the suitability of iPSC-SN for modelling $Na_v1.9$-related pain disorders

In the skin, peripheral nerves terminate in free nerve endings, which are surrounded by keratinocytes. Recent research has shown that keratinocytes contribute significantly to mechanosensation and pain perception. Keratinocytes can modulate neuronal activity by releasing various pro-inflammatory and neuroactive factors. In skin disorders such as Pachyonychia congenita (PC), patients frequently report neuropathic pain as their primary symptom, particularly in the context of palmoplantar keratoderma. Interestingly, shaving the callus of these areas does not alleviate the pain, indicating a potential chronic sensitization of nociceptive fibers by keratinocytes with aberrant responses to mechanical stress. However, the mechanistic link between mechanical stress in diseased keratinocytes and neuropathic pain remains unknown.

Therefore, the aims of the second project were to

- Develop an *in vitro* system for the application of cyclic mechanical compression on keratinocytes derived from healthy donors and PC patients

- Investigate the mRNA expression of neuroactive factors in keratinocytes from healthy donors and PC patients following mechanical compression compared to uncompressed controls
- Investigate if neuroactive factors secreted into the media by keratinocytes from healthy donors and PC patients following mechanical compression would increase the neuronal excitability of mDRG neurons

3 List of Materials

Product	Company	Order number
Accutase	Sigma Aldrich	A6964
4-Aminopyridine	Sigma Aldrich	275875
Agarose	Invitrogen	16500-500
Antibiotic-Antimycotic (100X)	Gibco	15240062
AraC (1-β-D-Arabinofuranosyl-cytosin-hydrochlorid)	Sigma Aldrich	C6645-25MG
Ascorbic Acid	Sigma Aldrich	A8960-5g
B27 supplement	Thermo Fisher Scientific	17504-044
Beta-III-Tubulin (D71G9)XP® Rabbit m Antibody	Cell Signaling	5568
BMP4	Miltenyi Biotec	130-111-168
CaCl2	Roth	5239
Calcein-AM	AAT Bioquest	ABD-22002
CdCl2	Sigma Aldrich	202908
Cell Line Nucleofector® Kit V	Lonza	VCA-1003
CHIR99021	Tocris	4423
Collagenase	Sigma Aldrich	C9722
CryoStor CS10 freezing medium	Sigma Aldrich	C2874
CsF	Sigma Aldrich	198323
Dapt	Tocris	2634
D-Glucose	Millipore	1.08337.1000
Dibutyryl cAMP	Stem Cell Technologies	100-0244
DMEM F12 (low glucose)	Gibco	11320033
DMEM high glucose	Gibco	41965-062
DMEM-F12 Glutamax	Thermo Fisher Scientific	21331-020
DMSO (100 %)	New England Biolabs	N3232
Doxycycline	Sigma Aldrich	D3447-500MG
DPBS	Gibco	14190-169
EDTA	Invitrogen	15575020
EGTA	Sigma Aldrich	E4378
EpiLife Media 60 µM calcium	Gibco	MEPI500Ca
Ethanol (70 %)	VWR	20821
FBS Superior	Sigma Aldrich	S0615
Fibronectin	Thermo Fisher Scientific	33010-018
Gel Loading Dye, prple (6x), no SDS	NEB	B7025S
Geltrex	Gibco	A14133-02
Gentamycin	Thermo Fisher Scientific	15710049
Glucose Solution (200 g/L)	Gibco	A2494001
GlutaMAX Supplement (100x)	Gibco	35050061

Goat anti-mouse igG (H+L) Cross-adsorbed secondary antibody, Alexa Fluor 488	Life Technologies	A-11001
Goat anti-rabbit IgG (H+L) Highly Cross-adsorbed secondary antibody, Alexa Fluor 555	Life Technologies	A-21429
Goat serum	Pan Biotech	P30-1001
HBSS	Gibco	14175095
HCL, fuming	Roth	4625.2
HEPES	Roth	9105.4
HEPES	Roth	9105.4
human basic FGF	Preprotech	AF-100-15
human beta-NGF	Preprotech	AF-450_01
human EGF	Preprotech	100-18B
human GDNF	Preprotech	450-10
Human Keratinocyte Growth Supplement (HKGS)	Gibco	S0015
human/murine/rat BDNF	Preprotech	450-02
Incucyte Caspase 3/7 dye	Sartorius	4440
Insulin (10 mg/mL)	PanBiotech	P07-04300
jetPEI	Polyplus	101-40N
KCl	Roth	6781.3
Kgluconate	Sigma Aldrich	G4500
Knockout Serum Replacement	Life Technologies	10828-028
Laminin (murine, 1-2 mg/mL)	Sigma Aldrich	L2020-1MG
Laminin 521 (human recombinant)	Biolamina	LN521-05
Laminin-coated coverslips	Neuvitro	GG-12-Laminin
LDN193189	Miltenyi Biotec	130-106-540
Lipopolysacharides	Sigma Aldrich	L3129-25MG
MEM nonessential amino acids	Gibco	11140-035
MgCL2	AppliChem	141396.1211
Mitomycin	Sigma Aldrich	M0503-2MG
N2 supplement	Thermo Fisher Scientific	17502-048
Na2-ATP	Sigma Aldrich	A2383
NaCl	Roth	3957.1
NaCl for cell culture and patch clamp	Roth	3957.1
NaCL solution (150mM) for transfection	Polyplus	702-50
Na-GTP	Sigma Aldrich	G8877
Neurobasal A medium (-Glc, -NaPyruvat)	Gibco	A2477501
Neurobasal medium	Gibco	21103-049
NT-3 (human recombinant)	Peprotech	450-03
NucBlue™ Live Cell Stain ReadyProbes™ reagent	Gibco	R37605
Nuclease-free H_2O	Roth	T143.1
NucleoSpin RNA XS Micro Kit for RNA Isolation	Machery-Nagel	740902.5
PBS+MgCL+CaCL2	Sigma Aldrich	D8662
Penicillin/Streptomycin	Sigma Aldrich	P4333
Perfusion Pencil	Science Products	04-250

Peripherin Antibody (A-3)	Santa Cruz Biotechnology	sc-377093
pmax GFP	Lonza	N/A
Poly-D-Lysine	Sigma Aldrich	P0899
Poly-Ornithin	Sigma Aldrich	3655
Propidium iodide	Sigma Aldrich	P4170-10MG
Protease	Sigma Aldrich	P8811
Puromycin (10 mg/mL)	Invivogen	Ant-pr-1
Retinoic acid	Sigma Aldrich	R2625-50MG
Rock inhibitor (Y-27632)	Stem Cell Technologies	72308
Rotifix Histo 4% PFA	Roth	P087.6
SB431542	Miltenyi Biotec	130-106-275
Sensifast cDNA synthesis kit	Bioline	65053
Sensimix SYBR NO-ROX Kit	Bioline	QT650-05
Sigmacote	Merck	SL2-100ML
Sodium azide	Sigma Aldrich	S2002
Sodium pyruvate (100 mM)	Gibco	11360088
StemMACS™ iPS-Brew XF (Basal medium + supplement)	Miltenyi Biotec	130-104-368
SU5402	Sigma	SML0443-5MG
TEA-Cl	Sigma Aldrich	T2265
Tetrodotoxin	HelloBio	HB1035
Triton-X100	Sigma Aldrich	x100
Trypan blue	Sigma Aldrich	93595
Trypsin Neutralizer Solution	Gibco	R002100
Trypsin-EDTA	Life Technologies	25300-054
Vitronectin (500 µg/mL)	Life Technologies	A14700
Vivaspin 20 centrifugal concentrators, 3,000 MWCO PES	Sartorius	VS2091
β- mercaptoethanol	Gibco	31350-010

Consumable	**Company**	**Order number**
35 mm glass- bottom dishes	Cellvis	D35-20-0-N
Cell scraper	Bioswisstec	800030
Cryo Vials CryoStor CS10	Dominique Dutcher	390708
Glass coverslips	Paul Marienfeld GmbH & Co. KG	11520
Pasteur pipettes	Brand	747715
Perfusion Pencil	Science products	Z-04-04-XXX
Plastic coverslips	Sarstedt	83.1840.002
Vivaspin centrifugal concentrators	Sigma Aldrich	Z629456-12EA

Equipment	Name	Company
Confocal microscope	LSM700	Zeiss
Gel electrophoresis	Powerpac 300	Bio-RAD
Microscope	EVOS M5000	Invitrogen
Patch Clamp Amplifier	EPC_10_USB amplifier	HEKA Electronics
PCR-cycler	Peqstar	Peqlab
qPCR-cycler	CFX Opus 96 real-time pcr system (Bio-RAD)	Bio-RAD

4 Methods

4.1 Culture of induced-pluripotent stem cells

The use of iPSC lines was approved by the Ethics Committee of the Medical Faculty of the RWTH Aachen University (approval number EK243-187/8), and informed consent was obtained from the donors. IPSC lines Ctrl_1, Y66S_1 and Y66S_2 were kindly provided by Dr. Anika Neureiter, Prof. Angelika Lampert (Institute of Neurophysiology, Uniklinik RWTH Aachen, Germany) and Prof. Martin Zenke (Department of Hematology, Oncology and Stem Cell Transplantation, Uniklinik RWTH Aachen, Germany) from the Bio2Treat Consortium. Immature neurons differentiated via the NBI protocol from iPSC lines Ctrl_2 and Ctrl_3 were kindly provided by Dr. Pascal Röderer and Prof. Oliver Brüstle (Institute of Reconstructive Neurobiology, Uniklinik Bonn, Germany). All iPSC lines were reprogrammed from peripheral blood mononuclear cells (PBMCs) and assessed for genetic abnormalities and pluripotency by the providers. Information about the cell lines and respective donors can be found in Table 2.

Table 2 Donor information on iPSC lines.

Cell line	Genotype	Phenotype	Gender	Age at sampling	In registry
Ctrl_1	Control	Healthy	Female	48 years	N/A
Y66S_1	Y66S variant in $Na_v1.9$	Small fiber neuropathy	Female	59 years	N/A
Y66S_2	Y66S variant in $Na_v1.9$	Small fiber neuropathy	Male	35 years	N/A
Ctrl_2	Control	Healthy	Male	50-54 years	hPSCreg https://hpscreg.eu/cell-line/UKBi013-A
Ctrl_3	Control	Healthy	Female	55-59 years	hPSCreg https://hpscreg.eu/cell-line/UKBi019-A

IPSCs were maintained at 37°C with 5 % CO_2. Cells were cultured in StemMACS™ iPS-Brew XF on vitronectin-coated cell culture plates (5 µg/mL, 1h at RT). Upon 80 % confluency and iPSC colony formation, iPSC colonies were detached by incubation with 0.5 mM EDTA in DPBS for 3 min at room temperature. Afterwards, the EDTA solution was removed, and fresh iPS-Brew medium was added to the cells. The colonies were then segregated into smaller clusters by pipetting up and down gently, without creating a single cell suspension, before reseeding the smaller iPSC clusters.

iPSCs were frozen for long-term storage in liquid nitrogen. For this, cells were detached in EDTA and collected in medium. The cells were then centrifuged for 5 min at 200 g and resuspended in cold freezing medium containing 90 % iPS-Brew and 10 % DMSO, supplemented with 10 µM ROCK-inhibitor Y-27632. The cell solution was added into cryovials and transferred to -80°C in freezing boxes for one to three days, before being transferred to a liquid nitrogen tank for long-term storage. For re-thawing the iPSCs, the cryovials were rapidly thawed at 37°C and mixed with 10

mL DMEM F12 medium. Afterwards, cells were centrifuged at 200 g for 5 min and resuspended in iPS-Brew medium supplemented with 10 µM ROCK-inhibitor before seeding.

4.2 Sensory neuron differentiation

Three sensory neuron differentiation protocols were compared, which differed in their induction of neuronal differentiation via small molecules (Chambers) or forced overexpression of transcription factors in iPSC-derived neural crest cells (NGN1) or iPSCs (NBI) to induce a neuronal cell fate (Figure 6). The maturation phase was similar for all protocols, with small differences in media composition. It is important to note that for the Chambers and the NBI protocol, the days of differentiation (or days *in vitro*, DIV) are counted from the iPSC stage (DIV0), whereas for the NGN1 protocol, the differentiation starts (DIV0) when the virus containing the NGN1 gene is added to the neural crest-like cells (NCLCs). These differences were kept as the intention of this study was to compare the differentiation protocols as used by other research groups and published in the literature.

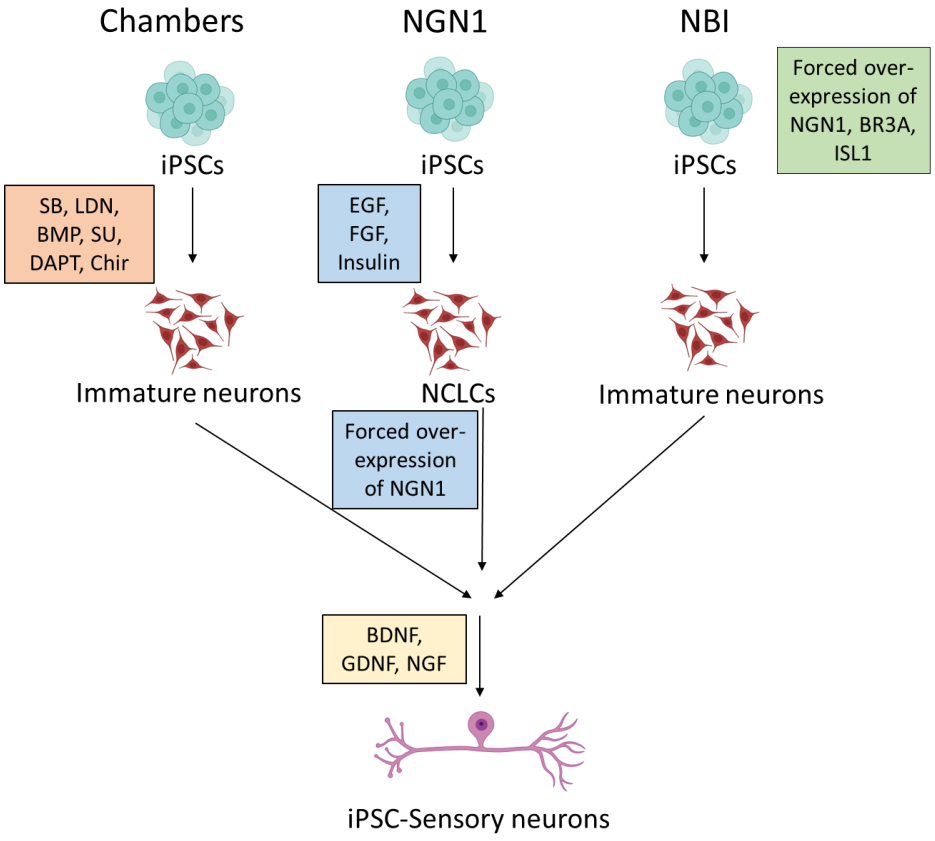

Figure 6 Schematic overview of the three iPSC to sensory neuron differentiation protocols. The Chambers protocol achieves neuronal induction in iPSCs via application of the small molecules SB, LDN, BMP, SU, DAPT and CHIR. In the NGN1-protocol sensory neurons are differentiated by overexpression of transcription factor NGN1 in neural crest-like cells (NCLCs) derived from iPSCs. In the NBI protocol, the transcription factors NGN1, BR3A and ISL1 are overexpressed at the iPSC level to generate immature neurons. All protocols use maturation media supplemented with BDNF, GDNF and NGF. BMP= Bone morphogenetic protein, NGN1=

Neurogenin 1, BR3A= brain-specific homeobox/POU domain protein 3A, ISL1 = Insulin gene enhancer protein 1, iPSCs= induced-pluripotent stem cells

4.2.1 Chambers differentiation protocol

Sensory neurons were generated from iPSCs via application of small molecules. The protocol is based on Chambers *et al*. (Chambers et al., 2012) with small modifications as previously published (Neureiter et al., 2022) and the addition of BMP4 during the neural induction phase. In brief, iPSCs were split into single cells by incubation with Accutase for 5 min at 37°C and seeded 229,000 cells/cm^2 on Geltrex-coated (150-160 µg/mL, 1h at 37°C) culture plates. Cells were cultured in iPS-Brew medium containing 10 µM ROCK-inhibitor Y-27632 for one day. At 90 % – 100 % cell confluence, neural progenitor cell (NPC) differentiation was induced by dual SMAD inhibition by the small molecules LDN193189 and SB431542 (DIV0). Given that WNT-,BMP- and SMAD2/3 signaling play a crucial role in sensory neuron development, the ideal concentrations of LDN193189 and BMP4 were tested for each cell line. For the first six days of differentiation, concentrations of 0, 100, 500 and 1000 nM LDN193189 in combination with 0,1 and 2 µg/mL BMP4 were tested for the Ctrl_1 and the Y66S_1 patient cell lines. Evaluation of sensory neuron generation by immunocytochemistry for peripherin and beta-III-tubulin revealed that for the Ctrl_1 cells 100 nM LDN193189 and 0 µg BMP4 generated the most peripherin-positive neurons, while for Y66S_1 100 nM LDN193189 and 2 µg/mL BMP4 generated the most peripherin-positive neurons. These conditions were applied for all the following differentiations.
Medium was changed daily with changing small molecules according to the NPC differentiation schedule (Table 3, Table 4, Table 5). On DIV10, NPCs were split into single cells using Accutase for 30-60 min at 37°C. Accutase incubation time was dependent on the time required for the NPCs to segregate into single cells. NPCs were then seeded at around 75,000 cells/cm^2 on glass or plastic coverslips. The glass coverslips had been previously prepared by incubation with 1 mM HCL overnight at RT, followed by coating with Poly-Ornithin (15 µg/mL) at 37°C overnight and finally coating with mouse Laminin (10 µg/mL) and Fibronectin (10 µg/mL) overnight at 37°C. The plastic coverslips were prepared by coating with Poly-Ornithin (50 µg/mL) overnight, followed by coating with human Laminin (10 µg/mL) overnight. Following the reseeding of the NPCs, the sensory neuron maturation phase began. For this, half medium changes with Chambers maturation medium (Table 6) were performed twice a week for 7 weeks. On DIV13-DIV14, 10 µM DAPT and SU were included in the medium. Neurons were treated with ARA-C (2 µM) on DIV15 ± 2 overnight to inhibit the growth of proliferative or not fully differentiated cells and remove them from the neuronal culture.
NPCs can be frozen at DIV10 for long–term storage in liquid nitrogen. For this, NPCs were detached as described above and resuspended in freezing medium containing 90 % sensory neuron maturation medium (without growth factors) and 10 % DMSO supplemented with 10 µM ROCK-inhibitor. The freezing and thawing process was performed as described earlier for iPSCs, with the NPCs being resuspended in sensory neuron maturation medium and directly seeded onto coverslips.

Table 3 Chambers neural progenitor differentiation schedule

Days *in vitro*	Medium	Small Molecules	
DIV0 and DIV1	100 % KSR medium	LDN193189 BMP4 SB431542	0-1000 nM 0-2 ng/mL 10 µM
DIV2 and DIV3	100 % KSR medium	LDN193189 BMP SB431542 SU5402 DAPT CHIR99021	0-1000 nM 0-2 ng/mL 10 µM 10 µM 10 µM 3µM
DIV4 and DIV5	75 % KSR medium 25 % N2/B27 medium	LDN193189 BMP SB431542 SU5402 DAPT CHIR99021	0-1000 nM 0-2 ng/mL 10 µM 10 µM 10 µM 3 µM
DIV6 and DIV7	50 % KSR medium 50 % N2/B27 medium	SU5402 DAPT CHIR99021	10 µM 10 µM 3 µM
DIV8 and DIV9	25 % KSR medium 75 % N2/B27 medium	SU5402 DAPT CHIR99021	10 µM 10 µM 3 µM

Table 4 Chambers KSR medium

Compound	**Concentration in Medium**
DMEM F12 GlutaMAX	85 %
Knockout Serum Replacement	15 %
MEM nonessential amino acids	100 µM
β- β-mercaptoethanol	100 µM
10 U Penicillin/1 µg/mL Streptomycin	1 x

Table 5 Chambers N2/B27 medium

Compound	**Concentration in Medium**
DMEM F12 GlutaMAX	50 %
Neurobasal	50 %
GlutaMAX	1 %
MEM nonessential amino acids	100 µM
N2 Supplement	1 x
B27 Supplement	1 x
10 U Penicillin/1 µg/mL Streptomycin	1 x

Table 6 Chambers sensory neuron maturation medium

Compound	Concentration in Medium
Neurobasal	100 %
B27 Supplement	1 x
GlutaMAX	1 x
10 U Penicillin/1 µg/mL Streptomycin	1 x
hBDNF	20 ng/mL
hGDNF	20 ng/mL
hNGF	20 ng/mL
Ascorbic Acid	200 µM
Murine Laminin	0.5 µg/mL

4.2.2 NGN1 differentiation protocol

NGN1-differentiated sensory neurons were differentiated and provided by Dr. Anika Neureiter (Institute of Neurophysiology, Uniklinik RWTH Aachen, Germany) with support from Luise Rüßmann and me during the maturation phase. Sensory neurons were differentiated via overexpression of the transcription factor NGN1, as previously described by Schrenk-Siemens *et al.*, with minor modifications (Schrenk-Siemens et al., 2022). In brief, iPSCs were detached using EDTA and seeded as small clusters into a 10 cm non-coated tissue culture dish in sphere medium supplemented with 10 µM ROCK-inhibitor (Table 7). Under these culture conditions, the iPSCs formed floating spheres. Medium was changed every other day for the initially floating spheres without ROCK-inhibitor. For this, the dish was tilted and the spheres and media were transferred to a Falcon tube and allowed to sink down by gravity until most of the medium could be removed. The spheres were then resuspended in fresh sphere medium and transferred to a new non-coated dish. After 7-10 days in culture, the spheres attached and neural crest-like cells (NCLCs) grew out. To harvest the NCLCs, the medium and spheres were aspirated from the dish and the NCLCs were incubated in Accutase at 37°C until detached. NCLCs were then collected in sphere medium and centrifuged at 200 g for 5 min.

At this stage, the NCLCs can be frozen for long-term storage. For this, the NCLCs were resuspended in cold freezing medium containing 90 % sphere medium and 10 % DMSO and frozen down stepwise as described earlier. The NCLCs were thawed in sphere medium as described for the iPSCs.

To obtain sensory neurons, 5,200 cells/cm^2 NCLCs were seeded in sphere medium on Poly-Ornithin (15 µg/mL), Laminin (10 µg/mL) and Fibronectin (10 µg/mL) coated dishes. After 24 h, NCLCs were transduced with a lentivirus carrying the coding sequence for NGN1 under control of a TET-ON promoter and a puromycin resistance cassette. The next day (DIV0), medium was changed to maturation medium (Table 8) containing 2 µg/mL Doxycycline for 10 days. On DIV3, 10 µg/mL Puromycin was added to the maturation medium to select for transduced cells. On DIV5, cells were reseeded onto Poly-Ornithin (15 µg/mL) and Laminin (10 µg/mL) coated coverslips (50-100,000 cells/cm^2). Medium containing Doxycycline was changed daily until DIV10, when maturation medium with either 0.5 mM dbcAMP or 0.125 µM retinoic acid was added to the cells and half-changed twice a week for 8 weeks.

Table 7 NGN1 Sphere Medium

Compound	Concentration in Medium
DMEM F12 GlutaMAX	50 %
Neurobasal	50 %
B27 Supplement	0.5 x
N2 Supplement	0.5 x
GlutaMAX	0.5 x
Insulin	2.5 µg/mL
10 U Penicillin/1 µg/mL Streptomycin	1 x
hEGF	10 ng/mL
hFGF	10 ng/mL
Y-27632	10 µM

Table 8 NGN1 Sensory neuron maturation medium

Compound	Concentration in Medium
Neurobasal-A	100 %
B27 Supplement	1 x
N2 Supplement	1 x
GlutaMAX	1 x
Glucose	5 mM
Sodium Pyruvat	0.055 mM
NaCl	35 mM
10 U Penicillin/1 µg/mL Streptomycin	1 x
hBDNF	20 ng/mL
hGDNF	20 ng/mL
hNGF	20 ng/mL
Ascorbic Acid	200 µM
Murine Laminin	0,5 µg/mL

4.2.3 NBI differentiation protocol

NBI-differentiated immature sensory neurons were differentiated and kindly provided by Dr. Pascal Röderer in the lab of Prof. Dr. Oliver Brüstle (Institute of Reconstructive Neurobiology, Uniklinik Bonn, Germany). Mature sensory neurons were generated from these by me and once kindly provided by Dr. Pascal Röderer. IPSC-derived sensory neurons were generated via over-expression of transcription factors NGN1, BRN3A and ISLET1 as previously described by Röderer *et. al* (Röderer, 2021). For this, a doxycycline inducible transcription factor overexpression cassette containing the three factors NGN1, BRN3A and ISLET1 was homozygously integrated into the AAVS1 safe harbor locus of iPSCs via TALEN-based genome editing. In brief, iPSCs were nucleofected with the NGN1-BRN3A-ISLET1 donor and TALEN plasmids using the Cell Line Nucleofector Kit V. Afterwards, cells were seeded onto Geltrex-coated (180 µg/mL) dishes and cultured in iPS brew-medium containing 10 µM ROCK-inhibitor Y-27632. Medium was changed daily. Three days post-nucleofection, edited clones were selected by the addition of 0.5 µg/mL

puromycin into the medium for about 5 days. Afterwards, edited clones were picked and expanded mono-clonally and checked for homozygous transgene integration via PCR.
Single-cell iPSCs were then seeded at 10,000 cells/cm^2 (DIV-1) into Geltrex-coated (180 µg/mL) T175-flasks and cultured in iPS-brew medium supplemented with 10 µM ROCK-inhibitor for 24 h. Afterwards, the cells were cultured in neural induction medium (Table 9) for 7 days, with the medium changed every other day. At DIV7, immature neurons were dissociated into single cells by incubation with Accutase for 45-60 minutes, centrifuged at 400 g for 10 minutes, resuspended in cold CryoStor CS10 freezing medium and frozen at -80°C in freezing boxes. After 24 h, frozen cells were transferred to a liquid nitrogen tank. The hereby generated immature sensory neurons were kindly provided by Dr. Pascal Röderer and Prof. Dr. Oliver Brüstle (Institute of Reconstructive Neurobiology, Uniklinik Bonn, Germany).

To obtain mature sensory neurons, frozen immature neurons were rapidly thawed at 37°C. Afterwards, 9 mL warm sensory neuron maturation medium (without growth factors, Table 10) was added dropwise to the cell suspension and the cells were centrifuged for 10 min at 400 g. The immature neurons were then resuspended in sensory neuron maturation medium supplemented with 10 µM ROCK-inhibitor and seeded at 35,000 cells/cm^2 on pre-laminin-coated coverslips that were additionally coated with Geltrex (360 µg/mL). Half-medium changes with maturation medium (Table 10) were performed twice a week for 8 weeks. 3 days post-seeding, cells were treated with Mitomycin C (1 µg/mL) for 2 h to remove non-neuronal cells from the culture.

Table 9 NBI neural induction medium

Compound	Concentration in Medium
Neurobasal	100 %
B27 Supplement	1 x
N2 Supplement	1 x
GlutaMAX	1 x
β-mercaptoethanol	20 µM
Gentamycin	12 µg/mL
Doxycycline	1 µg/ mL
Ascorbic Acid	200 µM

Table 10 NBI Sensory neuron maturation medium

Compound	Concentration in Medium
Neurobasal-A	100 %
B27 Supplement	1 x
N2 Supplement	1 x
GlutaMAX	1 x
β- mercaptoethanol	20 µM
Gentamycin	12 µg/mL
NT3	10 ng/ mL
hBDNF	10 ng/mL
hGDNF	10 ng/mL
hNGF	10 ng/mL
Ascorbic Acid	200 µM
Recombinant Laminin	100 ng/mL

4.3 Isolation of thoracolumbar mouse dorsal root ganglia neurons

The procedures for sacrificing mice and isolating murine dorsal root ganglia (DRG) neurons were approved by the State Agency for Nature, Environment and Consumer Protection (LANUV, Recklinghausen, Germany; reference no. 50191A4). In line with the 3R regulation, animal numbers were minimized and wild-type animals bred for other studies were reused. 3-6,5 months old male Gpr-101-Cre-B, male B6/J-SCN11a-LP)tm or female C57BL/6J mice were euthanized by CO_2 or isoflurane and killed by decapitation. Mice were placed on cold Sylgard platforms to reduce slow metabolic activity and related cell death. To isolate DRG bundles, first the internal organs were removed from the ventral side. Next, the vertebral column was cut in a straight line along the Anterior-Posterior (AP) axis from the sacral region to the neck while still attached to the body. The vertebra was then cracked open and the now visible thoracolumbar DRG bundles were cut out of the connective tissue. In a cell culture dish filled with cold HBSS, DRG bundles were further cleaned of connective tissue. For the generation of a single cell suspension, cleaned DRG bundles were enzymatically digested by 0.5 mg/mL protease (Sigma) and 1mg/mL collagenase IV (Sigma) at 37°C for 45-60 min. Next, digested DRG bundles were triturated through fire-polished Pasteur pipettes of decreasing diameters. Single DRG neurons were seeded on Poly-D-Lysine (0.1 mg/mL, overnight) and 2.5 µg/mL laminin (2.5 µg/mL, overnight) coated glass coverslips and maintained in DMEM F12 GlutaMAX containing 10 % FBS and 0.1 µg/mL nerve growth factor (Figure 7). Cells were left to adhere and patch clamped 20-52 h post-seeding. Mice euthanization and decapitation were performed by Danxia Bao and Raya Bott (Institute of Neurophysiology, Uniklinik RWTH Aachen, Germany).

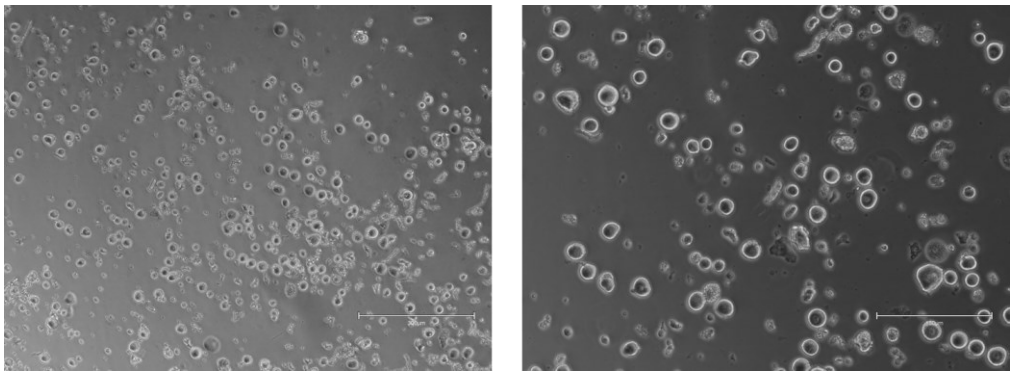

Figure 7 Images of isolated mDRG neurons. mDRG neurons were isolated from the thoracolumbar part of the spine of wild-type mice and imaged 20h after isolation. Scale bar left 300 µm, right 150 µm.

4.4 Manual patch clamp

Whole-cell patch clamp recordings were performed on mDRG neurons, 8-9 week old iPSC-sensory neurons and SH-SY5Y cells with a HEKA EPC_10_USB amplifier (HEKA electronics, Germany) at room temperature (~20 °C). Data were sampled at 50 kHz for voltage clamp and 20 kHz for current clamp and filtered at 10 kHz. Capacitive transients were compensated for and leak currents were measured with the P/4 method (leak hold -120 mV, leak delay 100 ms, leak size -0.1). The liquid junction potentials were corrected with 8.5 mV for the voltage clamp solutions and 13.4 mV for the current clamp solutions. The series resistance (Rser) was

compensated for as high as possible without causing cellular oscillations (50 - 90 %). The voltage error (VE) was calculated with the formula $\mathrm{VE} = \left(\mathrm{Rser} - \left(\mathrm{Rser} * \left(\frac{\mathrm{Rsercomp}}{100}\right)\right)\right) * \mathrm{I}$, where $\mathrm{Rser}_{\mathrm{comp}}$ is the percentage of series resistance that is compensated for and I is the maximum inward current. All the described functions were performed using the PatchMaster or PatchMaster Next software (HEKA electronics, Germany).

4.4.1 Voltage Clamp

For voltage clamp of iPSC-SN and small-diameter mDRG neurons, the bath solution contained (in mM) 140 NaCl, 1 $CaCl_2$, 1 $MgCl_2$, 10 HEPES, 20 TEA-Cl, 1 4-Aminopyridine, 0.1 $CdCl_2$, 1 D-glucose and 500 nM tetrodotoxin (pH 7.41, 327 mOsm). $CaCl_2$ and $MgCl_2$ stabilize the cellular membrane and HEPES buffers the pH. TEA-Cl and 4-Aminopyridine block potassium channels, whereas $CdCl_2$ blocks calcium channels. Fire-polished borosilicate glass pipettes (1.5 - 2.5 MΩ) were filled with a solution containing (in mM) 10 NaCl, 140 CsF, 10 HEPES, 1 EGTA, 5 D-glucose, and 5 TEA-Cl (pH 7.3, 316 mOsm). EGTA is a calcium chelator and CsF blocks potassium channels, stabilizes the seal formation between the patch pipette and cell and shifts the gating of $Na_v1.9$ to more hyperpolarized potentials.
For voltage clamp of SH-SY5Y cells transfected with $hNa_v1.9$, the bath solution contained (in mM) 140 NaCl, 3 KCl, 1 $MgCl_2$, 1 $CaCl_2$, 10 HEPES, 20 D-glucose and 500 nM tetrodotoxin (pH 7.4, 304 mOsm). Fire-polished borosilicate glass pipettes (2-4 MΩ) were filled with a solution containing (in mM) 10 NaCl, 140 CsF, 10 HEPES, 1 EGTA and 18 Sucrose (pH 7.3, 314 mOsm).

4.4.1.1. Voltage-dependence of activation and steady-state fast inactivation

Cells were held at -120 mV to minimize inactivation of $Na_v1.9$ and stepped to a test pulse at -40 mV every 10 s for 3 min to allow the seal and current to stabilize. In between every step protocol, an automated wait period of 5 s at –120 mV was programmed to allow for channel recovery from inactivation. To measure the voltage-dependence of activation, a step pulse protocol was applied from -110 mV to +40 mV in 10 mV increments (Figure 8A). To measure the voltage-dependence of steady-state fast inactivation, cells were prepulsed from -140 mV to 30 mV for 300 ms in 10 mV increments, followed by a test pulse at -40 mV for 100 ms (Figure 8B). Cells with a VE < 8 mV were included in the analysis.

4.4.1.2. Gravity-driven perfusion

For gravity-driven perfusion experiments, liquid reservoirs were connected through descending tubes to a perfusion pencil (Science Products), which was placed around 200 µm away from the cell on the bottom of the cell culture dish. For perfusion experiments with the $Na_v1.8$ blocker VX-548, cells were kept in the bath solution with 500 nM TTX and pulsed to -10 mV for 100 ms repeatedly every 10 s. After 10 sweeps without perfusion, the perfusion with ECS and 500 nM TTX was switched on to examine the effect of the perfusion flow on the current of the cell. After 10 sweeps with ECS & TTX perfusion, the perfusion with ECS containing 500 nM TTX and 100 nM VX-548 was started. After 10-25 perfusion sweeps with TTX and VX-548, the perfusion was stopped and the cell was measured for an additional 35-45 sweeps. For every perfusion experiment, a new coverslip with iPSC-SN was used.

4.4.1.3. Isolation of $Na_v1.9$ current in Voltage Clamp

For the TTXr-$Na_v1.9^{inact}$ protocol, two separate step protocols are applied to the cells: in the first one, the total TTXr current is measured (TTXr-total) and in the second one, the TTXr current is measured while $Na_v1.9$ is inactivated (TTXr-$Na_v1.9^{inact}$). The TTXr-$Na_v1.9^{inact}$ traces can then be subtracted from the TTXr-total current to obtain separate $Na_v1.8$/$Na_v1.5$ and $Na_v1.9$ current traces. The TTXr-total current was measured in a step protocol from -100 mV to +40 mV in 10 mV increments and 100 ms duration (Figure 8D). The TTXr-$Na_v1.9^{inact}$ current was measured by application of a prepulse of -60 mV, followed by a recovery period of 100 ms at the holding potential of -120 mV and the identical step protocol as used for TTXr-total (TTXr-$Na_v1.9^{inact}$a). Alternatively, the TTXr-$Na_v1.9^{inact}$ current was measured by changing the holding potential to -60 mV, -80 mV or -90 mV, applying a recovery period of -120 mV for 100 ms or 500 ms and then applying the step protocol to measure activation (TTXr-$Na_v1.9^{inact}$b) (Figure 8D). The TTXr-slow current was subtracted from the TTXr-total current in FitMaster v2x91 (HEKA Elektronik).
In the Leipold protocol, isolated $Na_v1.9$ current was recorded through applying a series of hyperpolarized pulses ranging from -110 mV to -55 mV of 100 ms length in 5 mV increments (Figure 8C). Isolation of $Na_v1.9$ current can be achieved in the protocol through the presence of CsF in the patch pipette, which shifts the gating of $Na_v1.9$ to more hyperpolarized potentials, thus isolating its gating from the gating of other Na_v channels.

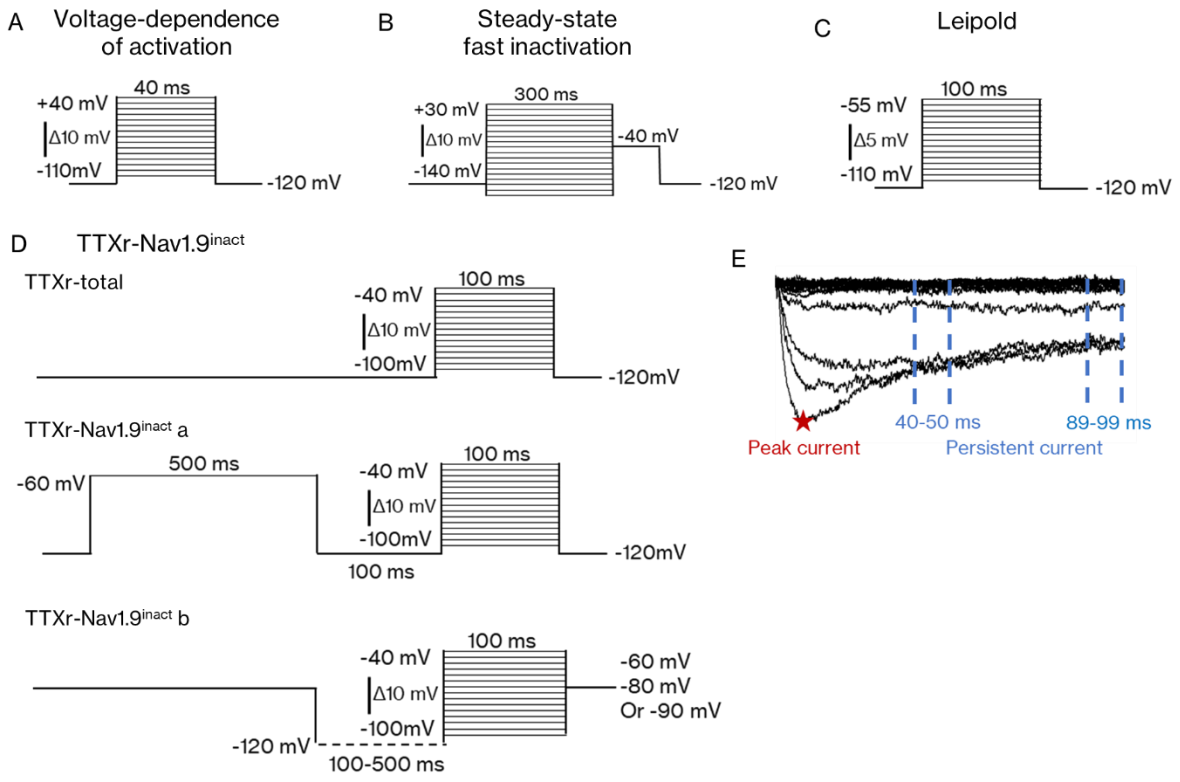

Figure 8 Voltage Clamp protocols. Electrophysiology protocols for voltage-dependence of A) activation and B) Steady-state fast inactivation. C) Leipold and D) TTXr-$Na_v1.9^{inact}$ protocol for $Na_v1.9$ current isolation. E) Indication of measured parameters in a representative current trace.

4.4.2 Current Clamp

For the current clamp of iPSC-SN and mDRG neurons, the bath solution contained (in mM) 140 NaCl, 3 KCl, 1 $MgCl_2$, 1 $CaCl_2$, 10 HEPES, and 20 glucose (pH 7.4; 296mOsm). The intracellular solution contained (in mM): 4 NaCl, 135 Kgluconate, 3 $MgCl_2$, 5 EGTA, 5 HEPES, 2 Na_2-ATP, and 0.3 Na-GTP (pH 7.25, 298 mOsm) and the pipette size ranged from 2-3.5 MΩ. The resting membrane potential (RMP) was measured with 0 pA current injection immediately after establishing the whole-cell configuration. The holding current (V_{Ihold}) was then adjusted to a membrane potential of -65 ± 5 mV for iPSC-SN and -60 ± 5 mV for mDRG. Action potentials were evoked by square current injection of 500 ms length in 10 pA or 0.5x rheobase increments (Figure 9).

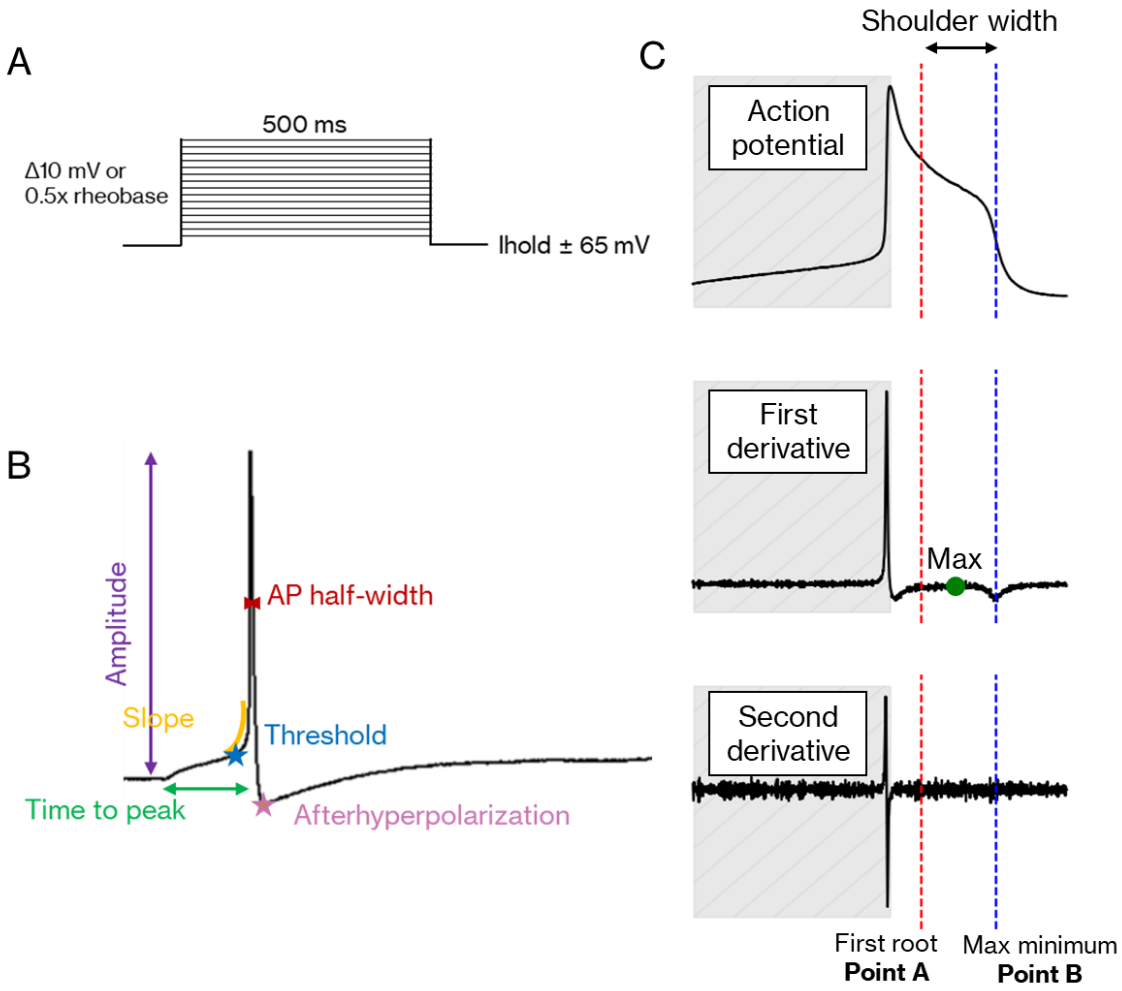

Figure 9 Current clamp protocols. A) Electrophysiology protocol to determine the rheobase or firing frequency. B) Indication of measured parameters in a representative action potential voltage trace. C) Graphical illustration of the determination of the action potential shoulder location, width and prominence. The action potential location was defined between the first root of the second derivative (Point A) and the following maximum minimum (Point B). The action potential width was measured between Point A and Point B in the action potential and the shoulder prominence was measured between the maximum of the first derivative (indicated with a green dot) within the shoulder location and Point B. Max= Maximum

4.4.3 Analysis of electrophysiological data

Peak current (I) and persistent current were analyzed with in-house procedures in Igor Pro (Wave Metrics, USA) (Figure 7E). The peak current was defined as the maximum inward current. mDRG neurons and iPSC-SN were identified as positive for TTXr current if the peak current exceeded 300 pA in the presence of 500 nM TTX and had a typical fast inward Na_v current shape. As Na_v channels gate very quickly, the peak current for activation and inactivation was measured between the first 0.1 to 10 ms after the start of the pulse application. For the measurement of the slower gating $Na_v1.9$, the window was set between 0.2 and 50 ms. The persistent current was measured as the mean current between 40-50 ms and 89-99 ms after the start of the applied test pulse. This is a timepoint at which only a very slowly inactivating current can be measured.

The conductance (G) was calculated with the equation $G = \frac{I}{V - V\mathrm{rev}}$, where I is the peak current, V is the applied voltage at every step during the pulse protocol and Vrev is the reversal potential. The Vrev was calculated for each neuron by plotting the peak current at each potential against the respective voltage, resulting in an IV plot. Afterwards, a linear regression trendline was fitted to the points on the IV that had an ascending slope. The y-value of the intersection of this line with the x-axis of the IV plot was noted down as the reversal potential. The conductance was normalized to the maximum conductance (G/GMAX). For the steady-state fast inactivation curves, the peak inward current was normalized to the maximum peak inward current (I/IMAX). The voltage of half-activation/inactivation (V50) and the slope of the curves were determined in GraphPad Prism version 10 using a Boltzmann sigmoidal fit. Perfusion data was analyzed by normalizing the inward current at every sweep to the peak inward current and plotting it against the number of sweeps.

The resting membrane potential was defined as the mean voltage between 1 and 99 % of the first 20 ms sweep with zero current injection. Spontaneous activity at resting membrane potential was noted if at least one action potential above 0 mV was fired within this sweep. The rheobase was defined as the injected current at which the first action potential above 0mV was fired (measured in 10 pA increments) minus the holding current. The parameters above were analyzed in FitMaster. The action potential characteristics were analyzed in a customized Igor Pro procedure, as previously described (Meents et al., 2019) (Figure 8B). To calculate the action potential properties, the first action potential evoked by the square pulse protocol (Δ10 pA) was used. The action potential amplitude was measured between the membrane potential and the action potential peak. The voltage threshold was defined as the minimum of the first derivative of the action potential. The afterhyperpolarization was measured at the minimum following the action potential peak. The action potential half-width was defined as the distance between the depolarizing upstroke and the repolarizing downstroke and was measured at the half-distance between the voltage threshold and the action potential peak. The time to peak was measured between the current pulse onset and the action potential peak. The maximum slope of the upstroke was calculated between the action potential voltage threshold and peak. The input resistance was determined by application of two consecutive hyperpolarizing current steps of 100 ms length with a delta of +50 pA and calculated with the formula $\frac{(\mathrm{V1}-\mathrm{V2})\mathrm{mV}}{50\ \mathrm{pA}}$, where V_1 is the more hyperpolarized voltage potential. The cell capacitance was measured by the patch clamp amplifier as C-slow.

The action potential shoulder was analyzed using a customized Python script developed by Lennart Müller (Institute of Neurophysiology, Uniklinik RWTH Aachen, Germany). The shoulder location was determined between the first root of the second derivative (Point A) after the global

minimum of the first derivative and the largest minimum after the start of the shoulder (Point B) (Figure 9C). Minima (Point B candidates) occurring after two-thirds of the action potentials' downward phase were discarded. The prominence of the shoulder was calculated as the ratio of the difference between the maximum slope during the shoulder and the slope at Point B and the absolute slope at Point B $prominence = \frac{max\left(f'(x)\right)-f'(B)}{|f'(B)|}; x \in [A,B]$. Thus, a shoulder prominence of one corresponds to a mostly horizontal shoulder, while a value of zero indicates that no shoulder was present. Additionally, the shoulder width was determined as the time between the two points enclosing the shoulder (Points A and B). The firing frequency was defined as the number of action potentials above 0 mV that were fired at a given current pulse and analyzed in the customized Python script designed by Lennart Müller. Firing behaviour was determined in a protocol ranging from 0.5 x to 5x the rheobase in 0.5 x rheobase increments and classified by the following: 1 action potential = phasic, 2-4 action potentials intermediate and >5 action potentials tonic. If a neuron fired one action potential for the first sweeps and then suddenly switched to a high firing frequency (>5 action potentials) at higher current injections, its firing was classified as high threshold multiple.

4.5 Immunocytochemistry

After 8-9 weeks of neuronal maturation, iPSC-sensory neurons were fixed with 4 % PFA for 10 min at room temperature, washed with DPBS twice and stored in DPBS supplemented with 0.05 % sodium azide at 4°C. The immuncytochemistry procedure started with permeabilization of the cells with 0.1 % Triton X in DPBS for 10 min and blocking of non-specific binding with 5 % goat serum in DPBS for 60 min. Primary antibodies for beta-III-Tubulin and peripherin were diluted in 5 % goat serum in DPBS and incubated on the cells overnight at 4°C (Table 11). After washing three times with DPBS, the secondary antibodies diluted in 5 % goat serum in DPBS were incubated at room temperature for 60 min (Table 11). Afterwards, the cells were washed again three times with DPBS. DAPI NucBlue was added to the second wash step afterwards to stain the nuclei. Slides were imaged in an LSM 700 confocal microscope (Carl Zeiss) at 405 nm, 488 nm and 555 nm. Image J 1.54f was used to create overlay images and measure the diameter of the neuronal somas. Negative controls that only received the secondary but not the primary antibodies were used to assess the specificity of the primary antibody used.

Table 11 Antibodies for immunocytochemistry of iPSC-sensory neurons

Antibody	Dilution
Beta-III-Tubulin rabbit monoclonal primary antibody	1:200
Peripherin mouse monoclonal primary antibody	1:500
Goat anti-mouse igG secondary antibody, Alexa Fluor 488	1:500
Goat anti-rabbit IgG secondary antibody, Alexa Fluor 555	1:500

4.6 Transfection of SH-SY5Y and iPSC-SN with hNa$_v$1.9

SH-SY5Y cells were cultured at 37°C with 5 % CO_2 in DMEM high glucose with 10 % FBS for at least one week before transfection. Cells were either transfected with pmaxGFP or a codon-optimized

human $Na_v1.9$ sequence fused to pIRES2-EGFP (custom ordered from Biocat) (Figure 10A). For transfection, plasmid DNA and JetPei were first diluted in 150 mM NaCl, then mixed and incubated for 20 minutes at room temperature. The cells were split 24 or 48 h post-transfection to achieve single-cell density for patch clamp and patch-clamped around 4 h later upon adherence to the cell culture dish. IPSC-sensory neurons matured for 8-9 weeks were transfected with JeptPEI as described above and either pmaxGFP only or cDNA constructs containing the coding sequence for human wildtype $Na_v1.9$ combined with GFP (provided by Enrico Leipold, Figure 10B) for 20 h. IPSC-SN were analyzed via patch clamp-clamped 72 h post-transfection.

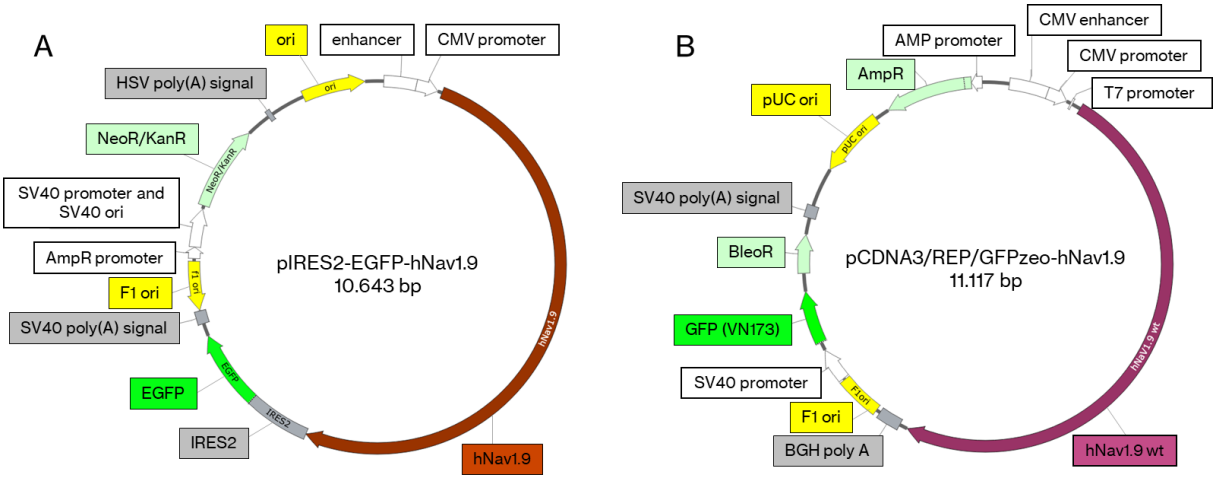

Figure 10 Plasmid maps for transfection with human $Na_v1.9$ A) Vector of pIres2-EGFP-h$Na_v1.9$. B) Vector of pCDNA3/REP/GFPzeo-h$Na_v1.9$. NeoR/KanR = neomycin/ kanamycin resistance, gene, ori= origin, AmpR= ampicillin resistance gene, BleoR= bleomycin resistance gene, bp= base pairs

4.7 Culture of human immortalized keratinocytes

The HaCaT cell line was generously provided by Dr. Nicole Schwarz and Prof. Rudolf Leube (Institute of Molecular and Cellular Anatomy, Uniklinik RWTH Aachen, Germany). Cells were cultured at 37°C in 5 % CO2 in DMEM F12 low glucose media and split at confluency by incubating with DPBS for 20 min, followed by incubation with trypsin-EDTA for 3-5 min.

Patient-derived human primary keratinocytes were obtained from skin biopsies from patients and immortalized by the human papillomavirus (HPV) E6/E7 method (Halbert et al., 1992). The wild-type human immortalized keratinocyte cell line HKC (WT) was kindly provided by Dr. Julia Reichelt, Dr. Verena Wally and Dr. Thomas Lettner (EB Haus Austria, Salzburg, Austria). The PC cell lines K6aN171K (PCK6) and K16R127C (PCK16) were generously provided by Dr. Leonard Milstone (Yale Dermatology Associates, New Haven, CT, U.S.A.). The cell lines HKC, K6aN171K and K16R127C were cultured at 37 °C in 5 % CO_2 in EpiLife media supplemented with human keratinocyte growth supplement and antibiotic-antimycotic solution. Cells were split twice a week by incubating with DPBS at 37°C for 15 min. Afterwards, DPBS was replaced with Accutase and incubated for another 10 min at 37°C. Enzymatic activity of Accutase was stopped by the addition of trypsin neutralizer and after centrifugation at 650 rpm for 4 min, cells were resuspended in media.

4.8 Co-Culture of mouse dorsal root ganglia and HaCaTs

Spatial separation of mDRG neurons and keratinocytes was achieved by pipetting cell solutions on separate ends of glass coverslips, relying on the surface tension of water and the hydrophobicity of the glass surface, resulting in water droplet formation. mDRG neurons were isolated and dissociated as described above and seeded onto one side of glass coverslips on DIV0. On DIV1, HaCaTs were added at the density of 10,000, 15,000 or 25,000 cells per coverslip. The HaCaT seeding was aimed at the side of the coverslip that was not occupied by mDRG neurons. The co-culture was maintained in DEMEM F12 low glucose with media changes every two days.

4.9 Compression device

A compression device was designed to apply defined dynamic cyclic compressive stresses to keratinocyte monolayers (Figure 11A). The device consists of a main housing, which is composed of 3D-printed Polycarbonate and can hold six 35 mm glass-bottom dishes at the bottom. On top, the housing is connected to a guide made from Polyether ether ketone (PEEK) that holds six stamps perpendicular immediately above the middle of the dishes. The stamps were also produced from cell-compatible PEEK, have a diameter of 15mm at the bottom and have a basket for additional weights above the guide (Figure 11B). Through the guide, the stamps can be lifted and released simultaneously with a movement arm that is connected to a servo motor (Generic Metal Gear (Micro S), EXP, Saarbrücken, Germany). The compression amplitude and frequency can be adjusted by adjusting the voltage applied to the motor and the height of the lever connected to the guide (example in Figure 11C). The design of the compression device and the guides was done by Mert Karpat in Fusion 360 (Autodesk) and manufactured in-house (Department of Dental Materials and Biomaterials Research, Uniklinik RWTH Aachen, Germany).

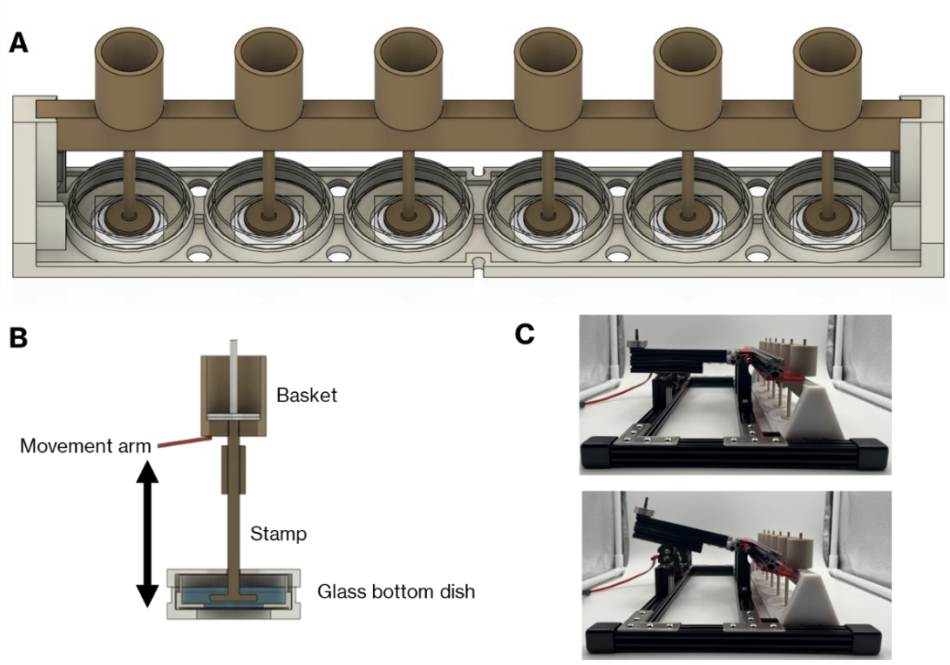

Figure 11 Compression Device. A) Front view of the compression device. B) Side view of one guide with a stamp inside a cell culture dish. C) Photographs of the compression device in rest (top) and compression (bottom) modus.

4.10 Keratinocyte compression

For compression, keratinocytes were reseeded onto 35 mm glass-bottom dishes (Cellvis) onto a defined growth area (Figure 11A). To achieve a defined growth area, coating and seeding guides were designed and 3D-printed from Polyamide. The coating guide had an outer diameter of 14 mm, while the seeding guide had an inner diameter of 14 mm. The coating guide was glued into the middle of the glass-bottom dish (D0). Afterwards, 250 µL hydrophobic Sigmacote (Merck) was added between the outer edge of the coating guide and the inner rim of the plastic surface. The Sigmacote-coated dish was left overnight to dry and sterilized with 70 % Ethanol and UV-light on the following day. Next, the cell seeding guide was placed into the middle of the dish and 300 µL of Geltrex (Life Technologies) diluted in media (1:50) was added into the middle of the seeding guide and incubated for 30 min at 37°C. Afterwards, the keratinocytes were split and seeded 200,000 cells/ dish into the seeding guide. After 1 h, after the cells had attached, the seeding guide was removed and 1.5 mL of media was added to the dish. On the following day, the media was changed to contain 1.2 mM calcium chloride ($CaCl_2$) to initiate differentiation and create a tight monolayer (Figure 11B).
24 h after the calcium switch, the compression procedure was started. For this, the media was changed and 3 mL medium with 1.2 mM CaCl2 was added to keep the compression stamp submerged during compression. Next, the keratinocyte dishes were placed into the compression device at 37°C and 5 % CO2 and compressed for 1 h at 150 mHz with or without 7 g additional weight in the basket of the compression guide. Supernatant was collected and cells were lysed 2 h after compression. The coating and seeding procedures were in large parts performed by Kyeongmin Kim (Institute of Molecular and Cellular Anatomy, Uniklinik RWTH Aachen, Germany) with the support of me and Raphael Tönshoff (Institute of Neurophysiology, Uniklinik RWTH Aachen, Germany).

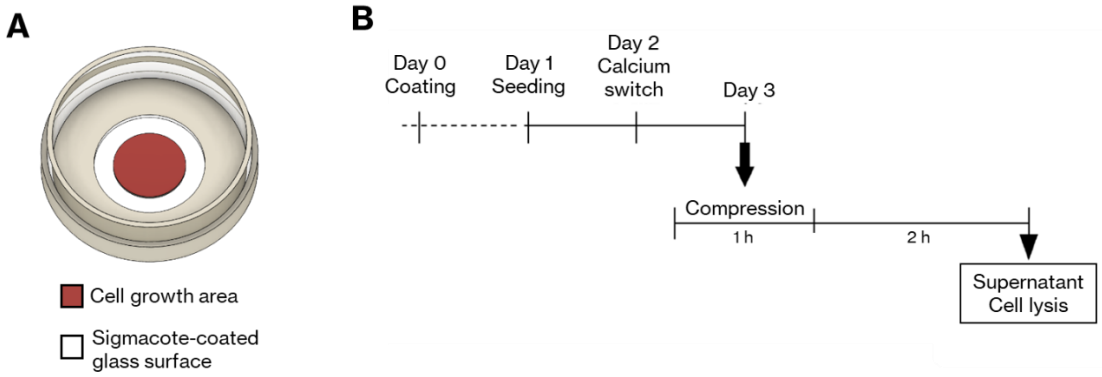

Figure 12 Keratinocyte compression procedure. A) Glass bottom dish with defined keratinocyte growth area created by hydrophobic Sigmacote coating. B) Timeline of compression experiments.

4.11 Quantitative real-time PCR

To quantify the mRNA levels in the different cell lines with and without compression, quantitative real-time PCR (qPCR) was performed. For this, cells were lysed 2 h after 1 h of compression by scraping the cells off in lysis buffer from the NucleoSpin RNA Micro Kit. Next, RNA was isolated according to the manufacturer's instructions and quantified photometrically. Afterwards, 450 ng of RNA were used to produce cDNA with the Sensifast cDNA synthesis kit according to the

manufacturer's instructions. Primers for real-time qPCR were created using the BLAST software from NIH, assessed in the Oligo-analysis tool from Eurofins Genomics for their tendency to form primer-dimers and custom-ordered from Eurofins Genomics (**Table 12**). To validate the designed primers experimentally, WT keratinocytes were exposed to lipopolysaccharides (LPS) for 24 h, to upregulate the target mRNAs. PCR was performed with the SensiMix SYBR No-ROX Kit according to Table 13 and Table 14 in the Peqstar cycler (Peqlab). PCR products were mixed with gel loading dye (2 µL to 10 µL sample), applied to a 1 % agarose gel and ran for 20 min at 90 V in a gel electrophoresis chamber (BioRAD Powerpac 300). The gel was then examined for the presence of a single band, indicating that only one PCR product was produced with the designed primers. This applied to all primers listed below (**Table 12**). To examine primer efficiency, the samples were run in eight concentrations from 0-50 ng of cDNA in the CFX Opus 96 real-time PCR system (Bio-RAD) according to Table 14. From this data, a standard curve was plotted and fitted with a linear regression. Primer efficiency was calculated with the formula $10\text{^}(-1/\text{regression slope}) - 1) * 100$ and was between 96-250 % for the primers below and therefore, these primers were included in further qPCR experiments.

Table 12 Primer sequences for RT-qPCR.

Gene	Forward Primer	Reverse Primer
hIL-1α	TGACTGCCCAAGATGAAGACC	TGCCGTGAGTTTCCCAGAAG
hIL-1β	AGCTCGCCAGTGAAATGATG	GGTGGTCGGAGATTCGTAGC
hIL-6	TAGTGAGGAACAAGCCAGAGC	GGCATTTGTGGTTGGGTCAG
hIL-8	CTTGGCAGCCTTCCTGATTTC	TGGTCCACTCTCAATCACTCTC
hTNF-α	AGGCAGTCAGATCATCTTCTCG	GCTGGTTATCTCTCAGCTCCAC
hNGF	CCAAGGGAGCAGCTTTCTATC	GTGTGGTTCCGCCTGTATG
hIL-31	ACAGTCCCTCTCGAAGATGC	TTGAGATATGCCCGGATGGC
h-OSM	AGCTGCTCGAAAGAGTACCG	TGCAGTGCTCTCTCAGTTTAGG
hGAPDH	AGCCACATCGCTCAGACAC	GCCCAATACGACCA ATCC
hHPRT1	TGACCTTGATTTATTTTGCATACC	CGAGCAAGACGTTCAGTCCT

Table 13 RT-qPCR components.

Component	**Volume per reaction (µL)**
Forward Primer	0.325
Reverse Primer	0.325
SYBR green	6
Water	0,35
cDNA	5

Table 14 RT-qPCR temperature cycle.

Temperature (°C)	**Time (mm.ss)**
95	10.00
95* repeated for 40 cycles	00.15
60* repeated for 40 cycles	00.30
95	01.00
60-95 in 0.5°C increments: Melt curve analysis	

qPCR samples were pipetted according to Table 13. qPCR was performed with the SensiMix SYBR No-ROX Kit in the CFX Opus 96 real-time PCR system (Bio-RAD) according to Table 13. Samples were run in technical duplicates and a no reverse transcriptase and no cDNA control were run to quality control for non-contaminated primer probes and absent primer-dimer.
Primer efficiency for each qPCR plate was calculated in LinRegPCR software, that has been published by Ramakers *et al.* (Ramakers et al., 2003). Data was normalized to the reference genes GAPDH and HPRT1. Data is presented as $\text{primer efficiency}^{-\Delta\Delta Ct}$. Statistical testing requires a dataset that presents the mean and the distribution of the data, which is not given in the ΔΔCt-method, where the control group is set to 1. Therefore, Statistical testing was conducted on $\text{primer efficiency}^{-\Delta Ct}$.

4.12 Incubation of mDRG neurons with supernatant from compressed keratinocytes

The supernatant of compressed and uncompressed keratinocytes was collected after 2 h and centrifuged at 16,000 g. The supernatant without the debris at the bottom of the tube was then frozen at -80°C until further use. On the day of the mDRG incubation with the keratinocyte supernatant, mDRG neurons were prepared as described above and left to acclimate in the DMEM F12 GlutaMAX supplemented with 10 % FBS, 1x PenStrep and 0.1 µg/mL NGF for 5 h before incubation with the supernatant of the compressed keratinocytes. This allowed the mDRG neurons to recover from the isolation procedure and attach firmly to the glass coverslip.
On the same day, the keratinocyte supernatant was thawed on ice and concentrated in centrifugal concentrator tubes with a pore size of 3 kDa for 120 min at 4600 g at 4°C. The concentrated supernatant was then rediluted in DMEM high glucose supplemented with 10 % FBS and 1x PenStrep to a total volume of 1.2 mL. This solution was then added to the mDRG neurons and incubated for 12-48 h. Current clamp of mDRG neurons was performed 12- 48 h after the keratinocyte supernatant had been added. The coverlips of the different conditions were alternated over the patch clamp period to create comparable incubation times between the conditions.

4.13 Statistical analysis

Statistical analyses were performed in GraphPad Prism version 10. Data was assessed for normal distribution, followed by two-tailed T-tests/Mann-Whitney tests or One-way ANOVAs/ Kruskal-Wallis tests. P-values smaller than 0.05 were considered significant and are indicated as follows: * $p < 0.05$, ** $p < 0.01$, ***$p < 0.001$ and ****$p < 0.0001$. All electrophysiological data is shown as mean ± SEM unless otherwise stated. All qPCR data is shown as mean ± SD unless otherwise stated.

5 Results

5.1 Modelling neuropathic pain in iPSC-SN

IPSC-derived sensory neurons (iPSC-SN) present a promising tool to model Na_v variants of neuropathic pain patients. However, the composition of the TTXr Na_v channels in these cells remains unclear, but is a central determinant for their suitability to model human nociceptors. Therefore, in the following section, the usage of iPSC-SN as a model for neuropathic pain will be examined in two aspects: 1) how comparable the iPSC-SN are to native mDRG neurons and 2) whether the iPSC-SN are suitable as a neuropathic disease model for a $Na_v1.9$ variant.
In this thesis, three separate iPSC-SN differentiation protocols were examined to investigate if one protocol would produce more advanced iPSC-SN than the others. This allowed for the comparison between the differentiation protocols, as well as ensuring that the findings were not dependent on the differentiation protocol. The three protocols differed in the induction of neuronal differentiation via 1) small molecules (Chambers) 2) genetic overexpression of NGN1 at the neural crest stage (NGN1) or 3) genetic overexpression of NGN1, BRN3A and ISLET1 at the iPSC stage (NBI). It is important to note that the neuronal induction method is the main difference between the three differentiation protocols, but not the only one. While the maturation medium is largely comparable, small differences in coverslip coating or seeding density exist between the differentiation protocols. The iPSC-SN generated from all three protocols were examined for their TTXr and $Na_v1.9$ currents. The Chambers- and NGN1-differentiated iPSC-SN were additionally examined for their neuronal activity and action potential characteristics and suitability as a $Na_v1.9$-variant neuropathic pain model.

5.2 All three differentiation protocols generated peripherin-positive sensory neurons

In order to validate the successful differentiation of iPSCs into sensory neurons, the morphology of the developing neurons was assessed throughout the differentiation. Starting at the iPSC level, all cell lines grew in smooth-looking colonies in the absence of spontaneously differentiating cells (Figure 13). The Ctrl_2 iPSCs were cultured and genetically edited by Dr. Pascal Röderer according to the NBI protocol and obtained by me at the immature neuronal stage for further maturation. The Ctrl_3 iPSCs were differentiated by Dr. Pascal Röderer according to the NBI protocol and obtained by me after 8 weeks of sensory neurons maturation. Sensory neuron identity of the NBI-differentiated neurons was assessed via immunocytochemistry by Dr. Pascal Röderer. At the neural progenitor/ immature neuron stage (i.e., after reseeding the cells onto coverslips), all cell lines of all differentiation protocols appeared in a neuronal spindle-like shape with the first neurites growing out of the soma. Over the course of the differentiations, the neuronal soma quantity decreased while the soma size and neurite density increased. It was observed that the NGN1-differentiated neurons migrated into bigger clusters compared to Chambers or NBI-differentiated neurons. The immunocytochemistry after 8 weeks of maturation showed that all cell lines in all differentiation protocols were positive for the neuronal marker beta-III tubulin (TUJ1) and the peripheral neuronal marker peripherin. This double-positivity indicates the successful generation of peripheral sensory neurons.

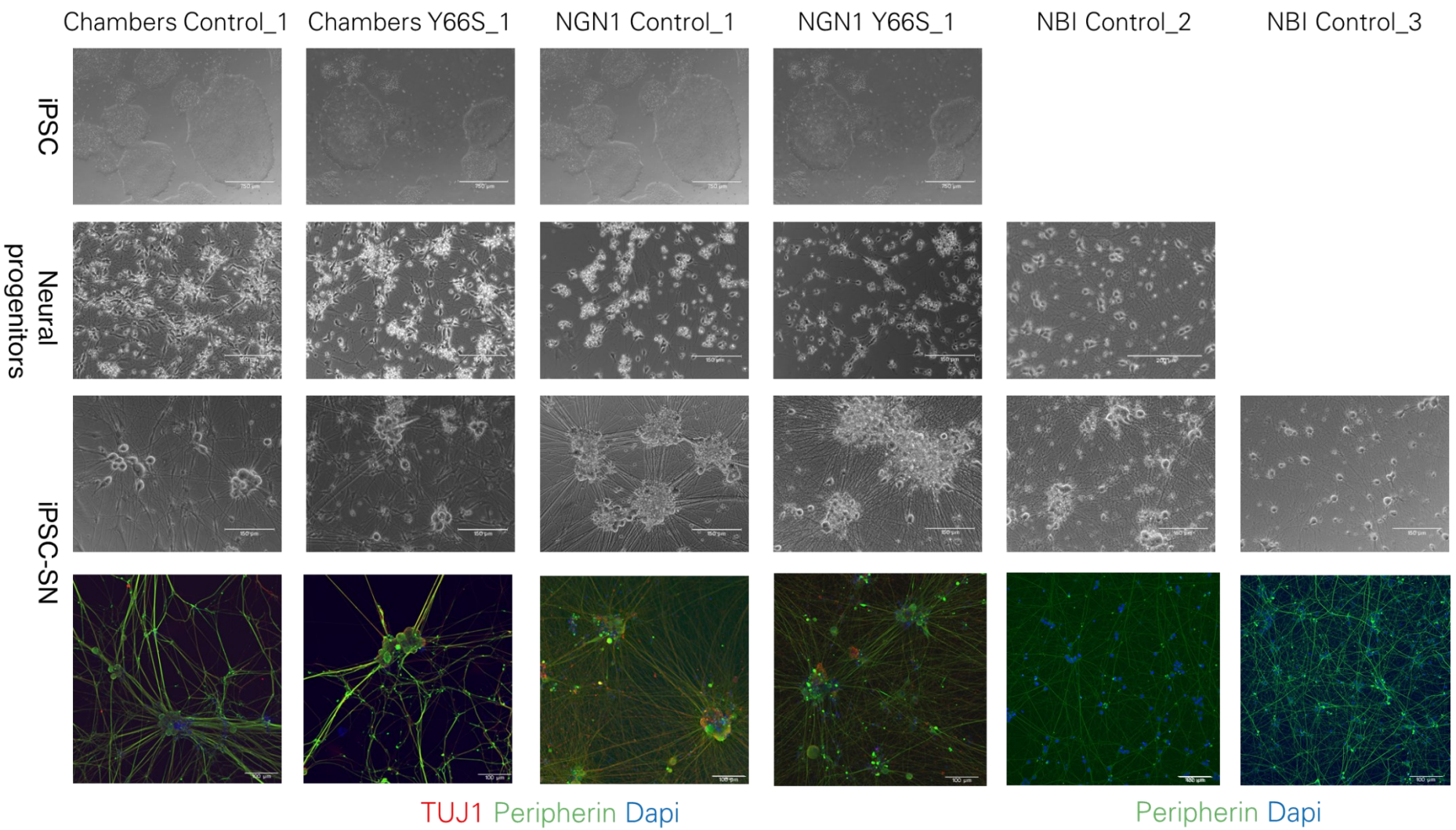
Chambers Control_1
Chambers Y66S_1
NGN1 Control_1
NGN1 Y66S_1
NBI Control_2
NBI Control_3
iPSC
Neural progenitors
iPSC-SN
TUJ1 Peripherin Dapi
Peripherin Dapi

Figure 13 Morphology of iPSC-SN. Brightfield images at the iPSC, neural progenitor and iPSC-SN stage (DIV55-64). Immunocytochemistry staining for peripherin (green) and DAPI (blue) of the three differentiation protocols at the sensory neuron stage. Images were taken at DIV55-64 for Chambers- and NGN1- differentiated neurons and included a beta-III-tubulin (TUJ1, red) staining. Images for the NBI-differentiated neurons were kindly provided by Dr. Pascal Röderer and taken at DIV21/28. Scale bar iPSC 750 µm, neural progenitor 150 µm and iPSC-sensory neuron 100/150 µm (except NBI Ctrl_2 neural progenitor 200 µm).

Quantification of the neuronal somata diameter showed that Chambers and NGN1-differentiated neurons were of similar size (22.7 ± 0.7 and 21.5 ± 0.6 µm, respectively, Figure 14). The NBI-differentiated cells were smaller than the other iPSC-SN (17.4 ± 0.9 µm), but still slightly larger than the isolated small-diameter mDRG, which were presumed c-fibers (15.8 ± 1.1). However, isolated thoracic hDRG neurons are twice as big (Davidson et al., 2014). Notably, the morphology and peripherin-positive staining of the generated neurons indicate the generation of sensory neurons, but to establish if the differentiation was truly successful, the electrophysiological functionality of the neurons had to be assessed.

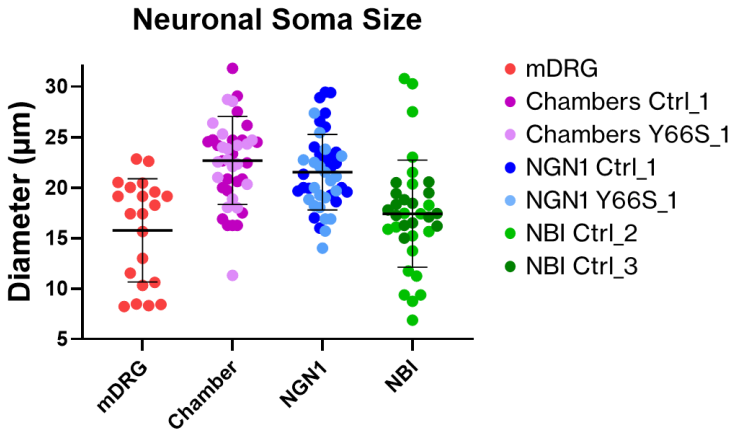

Figure 14 Diameter of neuronal somata of iPSC-SN and mDRG neurons. iPSC-SN somata were measured at DIV55-58. mDRG neuron somata were measured 24 hours post-isolation.

5.3 The majority of iPSC-SN exhibit TTX-resistant currents

The functional presence of the peripheral VGSCs $Na_v1.8$ and $Na_v1.9$ is essential in any nociceptor model. To assess the presence, distribution and gating characteristics of the TTXr channels, voltage clamp experiments were conducted in the presence of 500 nM TTX in the bath. Small-diameter mDRG neurons served as a positive control for mature sensory neurons, known to exhibit functional $Na_v1.8$ and $Na_v1.9$ currents, with low levels of the developmental $Na_v1.5$ channel. Quantification of the number of iPSC-SN showing TTXr currents larger than 300 pA showed that almost all iPSC-SN exhibited TTXr currents (Figure 15). The amount of TTXr current-positive cells was comparable between the three differentiation protocols. 98 % of Chambers-differentiated iPSC-SN were positive for TTXr currents, while 93 % of NGN1-differentiated iPSC-SN and 98 % of NBI-differentiated iPSC-SN exhibited TTXr currents. In the murine model, 86 % of mDRG neurons displayed TTXr currents.

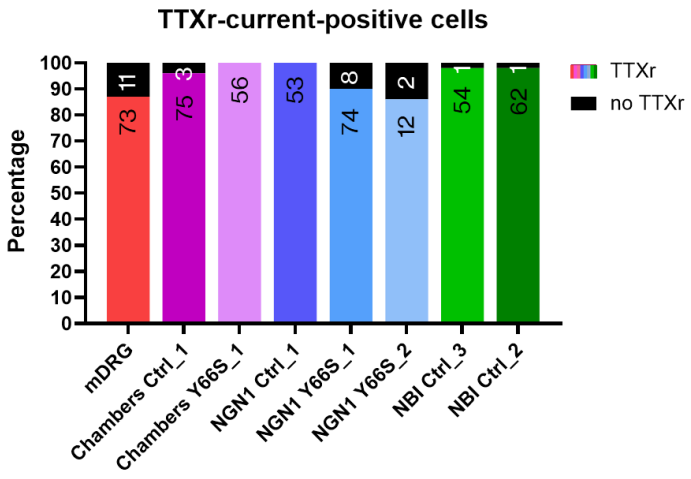

Figure 15 Quantification of TTXr current-positive mDRG neurons and iPSC-SN differentiated with the Chambers-, NGN1- or NBI-protocol. iPSC-SN were patch clamped at DIV55-64. mDRG neurons were patch clamped 20-52 h post-isolation. The bar graphs indicate the percentage of TTXr current positive cells in colour and TTXr current negative cells in black. The sample size is indicated within each sample bar.

5.4 IPSC-SN exhibit hyperpolarized activation and inactivation of TTXr currents compared to mDRG neurons

The Chambers- and NGN1-differentiated iPSC-SN showed an 800-1200 pA smaller peak TTXr current compared to the mDRG neurons, while the NBI-differentiated iPSC-SN exhibited 200-600 pA less current compared to mDRG neurons (Figure 16, Table 15). The peak current amplitude within iPSC-SN differentiated with the same protocol varied with the cell line. Interestingly, Chambers-differentiated iPSC-SN of the patient cell line Y66S_1 had an increased current amplitude compared to the Ctrl_1 cell line, whereas NGN1-differentiated iPSC-SN showed the opposite trend. The current amplitude was not normalized to the cell capacitance, as the cell capacitance measurement by the amplifier may be affected by the presence of many neurites in iPSC-SN, which are partially measured as part of the soma. However, it can be noted that the mDRG neurons were the smallest, suggesting a higher TTXr Na_v density in mDRG neurons compared to iPSC-SN (Figure 14).

Regarding the TTXr-gating characteristics of iPSC-SN compared to mDRG neurons, both the voltage-dependence of activation (V50) and steady-state fast inactivation were shifted towards more hyperpolarized potentials in iPSC-SN (Figure 16, Figure 17, Table 15). The iPSC-SN and mDRG neurons all start to activate between -80 to -70 mV, but a less steep slope of activation in the iPSC-SN results in a more hyperpolarized V50 (Figure 16E,F). The steady-state fast inactivation of TTXr currents was only tested for Chambers- or NGN1-differentiated cells. For both the Ctrl_1 and the patient cell line Y66S_1 in both differentiation protocols, the inactivation curve was significantly shifted by more than -20 mV to hyperpolarized potentials compared to mDRG neurons (Figure 17). The inactivation in iPSC-SN already starts at -140 mV, but only at –90mV in mDRG neurons. Furthermore, the iPSC-SN show a shallower inactivation slope across a larger range of potentials, whereas the mDRG neurons show a steep inactivation slope across a narrow range of potentials. Interestingly, the mDRG neurons did not reach full inactivation even at depolarized potentials of -10mV, but the iPSC-SN did.

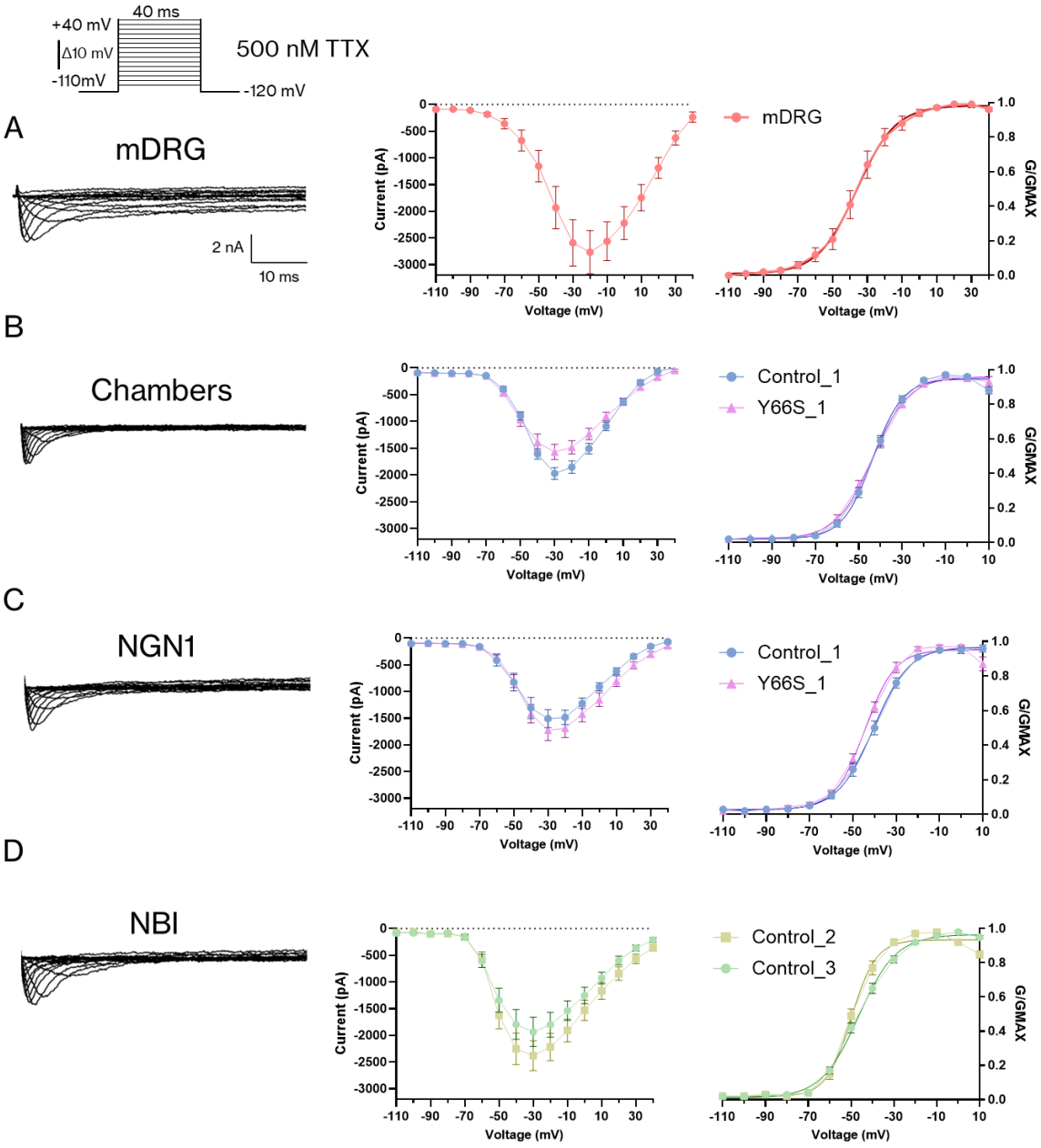
40 ms
+40 mV
Δ10 mV
-110mV
-120 mV
500 nM TTX
A
mDRG
2 nA
10 ms
Current (pA)
Voltage (mV)
G/GMAX
mDRG
B
Chambers
Control_1
Y66S_1
C
NGN1
D
NBI
Control_2
Control_3

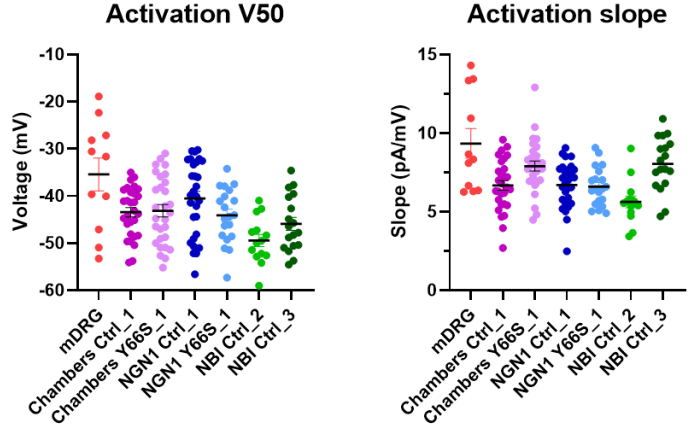
E
Activation V50
Voltage (mV)
F
Activation slope
Slope (pA/mV)
mDRG
Chambers Ctrl_1
Chambers Y66S_1
NGN1 Ctrl_1
NGN1 Y66S_1
NBI Ctrl_2
NBI Ctrl_3

Figure 16 Activation of TTXr channels in mDRG neurons and iPSC-SN. iPSC-SN were patch clamped at DIV55-64. mDRG neurons were patch clamped 20-52 h post-isolation. Representative trace, IV curve and conductance (G) curve normalized to the maximum conductance displayed with a line connecting the data points (lighter colour) and a Boltzmann fit (darker colour) for A) mDRG N=4, n=15, B) Chambers-differentiated iPSC-SN N=3, n=29, C) NGN1-differentiated iPSC-SN N=3, n=24-32, and D) NBI-differentiated iPSC-SN N=1, n=17-20. E,F) Voltage of half activation (V50) and slope of the activation curve were determined using a Boltzmann fit.

Significant differences between iPSC-SN cell lines could only be observed between the Chambers-differentiated Ctrl_1 and the NBI-differentiated Ctrl_2 in the peak current and V50 of activation, between the two NBI-differentiated control cell lines in the slope of the Boltzmann fitted conductance curve, between the Chambers-differentiated Y66S_1 and NBI-differentiated Ctrl_2 in the slope of the curve and in the steady-state fast inactivation of Chambers Y66S_1 and NGN1 Y66S_1. However, the iPSC-SN of all three differentiation protocols showed overall comparable TTXr gating characteristics when compared to mDRG.
To summarize, the iPSC-SN exhibited overall reduced TTXr currents and more hyperpolarized activation and inactivation kinetics in comparison to mDRG. The gating and currents of the iPSC-SN were comparable among the three analyzed differentiations of the same protocol, indicating robust protocols and sensory neuron development.

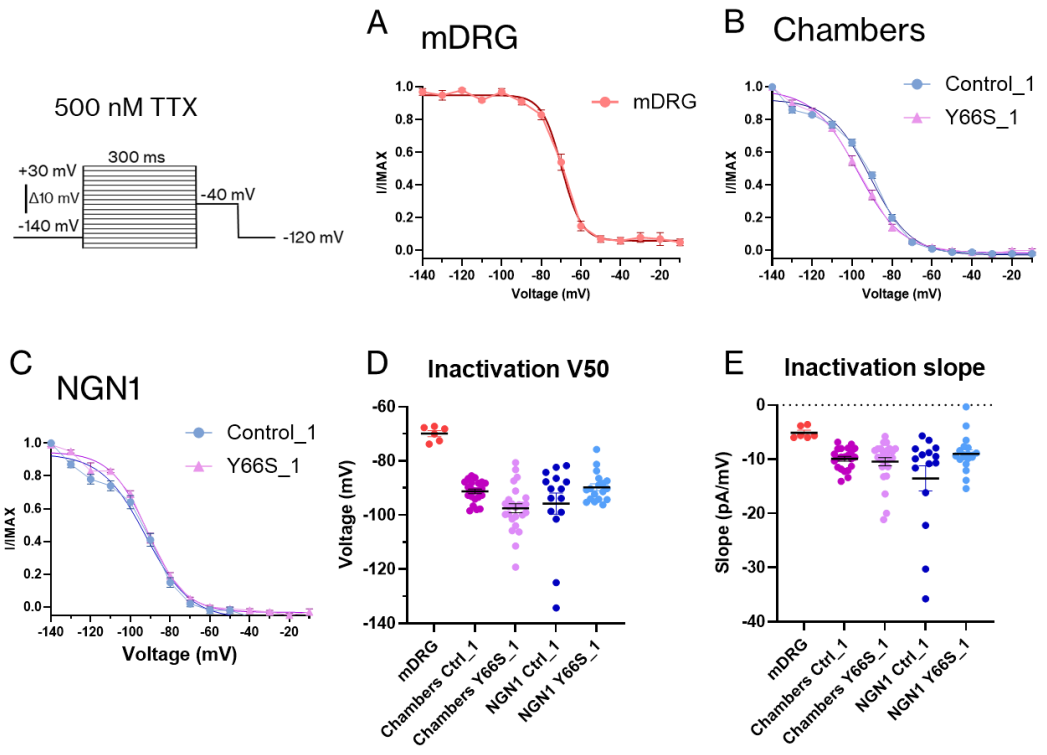

Figure 17 Inactivation of TTXr channels in mDRG neurons and iPSC-SN. iPSC-SN were patch clamped at DIV55-64. mDRG neurons were patch clamped 20-52 h post-isolation. Inactivation curves showing the peak inward current (I) normalized to the maximum inward current and displayed with a line connecting the data points (lighter colour) and a Boltzmann fit (darker colour) for A) mDRG N=2, n=7, B) Chambers-differentiated iPSC-SN N=3, n=22-24, and C) NGN1-

differentiated iPSC-SN N=2, n=15-19. D,E) Voltage of half inactivation (V50) and slope of the curve were determined using a Boltzmann fit.

Table 15 Activation and inactivation parameters of TTXr channels in mDRG neurons and iPSC-SN. iPSC-SN were patch clamped at DIV55-64 of differentiation. mDRG neurons were patch clamped 20-52 h post-isolation. The voltage of half activation/inactivation (V50) and slope were determined with a Boltzmann fit. Data is presented as mean ± SEM and statistical significance between iPSC-SN and mDRG (selected as control) was analyzed with a one-way ANOVA followed by a Tukey's multiple comparison test (if normally distributed) or a Kruskal-Wallis test followed by Dunn's multiple comparison test (if not normally distributed). Statistical significance between iPSC-SN and mDRG is indicated as follows *p≤0.05 **p≤0.01 ***p≤0.001 ****p≤0.0001.

Parameter	mDRG	Chambers		NGN1		NBI	
	mDRG	Ctrl_1	Y66S_1	Ctrl_1	Y66S_1	Ctrl_2	Ctrl_3
Peak current Voltage (mV)	-20	-30	-30	-30	-30	-30	-30
Peak current amplitude (pA)	-2765 ± 403	-1971 ± 112	-1568 ± 141**	-1509 ± 169**	-1727 ± 189**	2565 ± 279	2180 ± 329
Activation V50 (mV)	-35,4 ± 11,6	-43,5 ± 5,3**	-43,1 ± 7,1*	-40,5 ± 7,9	-44,1± 5,8**	-49.4 ± 4.9****	-45.9 ± 5.9***
Activation Slope	9,3± 3,1	6,7 ± 1,6***	7,9 ± 1,7	6,7 ± 1,5***	6,6 ± 1,2***	5.6 ± 1.4****	8.0 ± 1.7
Inactivation V50 (mV)	-69.92 ± 2.7	-91.2 ± 3.9****	-98 ± 8.4****	-95.8 ± 15****	-89.77 ± 5.4****	/	/
Inactivation Slope	-5.1 ± 1.1	-9.9 ± 2	-10.5 ± 3.8*	-13.5 ± 9***	-9 ± 3.3	/	/

5.5 TTXr-Na_v gating between control and Na_v1.9-Y66S variant iPSC-SN was comparable

Both the Ctrl_1 cell line and the patient cell line Y66S that carries the Na_v1.9 variant were differentiated via the Chambers and the NGN1 protocol to investigate if a difference in gating kinetics could be observed. In the Chambers-differentiated cells, the overall activation kinetics and V50 were similar between both cell lines; only the slope was significantly steeper in the control cell line (Figure 16B, Table 15). The steady-state fast inactivation was significantly more hyperpolarized in the patient cell line (Figure 17B, Table 15). In the NGN1-differentiated cells, the activation curve of the patient cell line was 4 mV more hyperpolarized than the control, but this difference was non-significant (Figure 16C, Table 15). This hyperpolarized shift in activation could also be observed in the small sample cells of the 2nd patient cell line Y66S_2, which carries the same Na_v1.9 mutation (Figure Appendix 1). The inactivation of the patient cell line Y66S_1 was 6 mV more depolarized (non-significant) and the slope was significantly steeper in the control cell line in the NGN1-differentiated iPSC-SN (Table 15). It is remarkable that while a depolarizing shift in activation and inactivation was found for the Na_v1.9-Y66S variant in mDRG neurons, the iPSC-SN partially showed hyperpolarizing shifts (van den Braak et al., 2025). Furthermore, the Chambers-differentiated Y66S_1 iPSC-SN showed a hyperpolarizing shift in the inactivation,

while the NGN1-differentiated Y66S_1 iPSC-SN showed a depolarizing shift in the inactivation compared to the controls. However, it is visible in the NBI-differentiated iPSC-SN that even two control cell lines can show a significantly different slope and difference in V50 of activation, which can be attributed to general variation within the population.

5.6 IPSC-SN present a mixture of at least two TTXr-Na_v channels

Regarding the inactivation characteristics of the iPSC-SN (Figure 17B,C), a biphasic fast inactivation (i.e., a change in inactivation slope) is visible in both cell lines in the Chambers- and NGN1-differentiated neurons. This hints at a population of at least two TTXr-Na_v channels that inactivate at different potentials. The first inactivation phase begins at -140 mV until around -100mV and the second steep inactivation phase ranges between -100 to -70mV. The inactivation and activation of the iPSC-SN start at very hyperpolarized potentials, which would indicate the presence of $Na_v1.5$. Furthermore, this biphasic inactivation is not evident in the mDRG neurons, which express functional $Na_v1.5$ in very small quantities. This hints at the presence of a combination of $Na_v1.5$ and at least one more TTXr-Na_v channel current in iPSC-SN. Whether the other TTXr-Na_v channel present in iPSC-SN could be $Na_v1.8$, $Na_v1.9$ or both can be analyzed in the current shape. The representative traces of all three iPSC-SN differentiation protocols show a slower inactivating component, which took up to 11 ms to inactivate (Figure 16B,C,D). This slow inactivation is characteristic for $Na_v1.8$, whereas the persistent current characteristic for $Na_v1.9$ (visible in the mDRG representative trace in Figure 16) cannot be observed. The following experiments investigated whether the iPSC-SN show functional $Na_v1.8$ or $Na_v1.9$ currents in addition to the presumed $Na_v1.5$ currents.

5.7 Application of $Na_v1.8$ blocker VX-548 could not clearly identify $Na_v1.8$ current in iPSC-SN

To evaluate if there is functional $Na_v1.8$ current present in the iPSC-SN, 100 nM of the selective $Na_v1.8$ blocker VX-548 (Suzetrigine) was applied to the Ctrl_1 cell line via gravity-driven perfusion or in the bath solution (Osteen et al., 2024). Perfusion was used as a qualitative measure of current reduction upon blocker application and was performed in four different cells of the Ctrl_1 cell line differentiated with the Chambers protocol. The inward current of the cells was repeatedly measured at -10 mV, which is a potential around which $Na_v1.8$ should have its peak inward current. Cells were first measured for 10 sweeps with TTX in the bath without perfusion, then for 10 sweeps with ECS + TTX perfusion, followed by 10-25 sweeps with ECS + TTX + VX-548 perfusion and finally the perfusion was switched off to see if the current reduction continued. In all four measured cells, the inward current decreased upon the application of the first perfusion with ECS + TTX (Figure 18). This means that the application of fluid shear stress through the perfusion reduced the current size regardless of the presence of any blocker. Upon application of the perfusion with ECS + TTX + VX-548, the current decreased further, which continued after the perfusion with TTX and VX-548 was stopped (cell 247 died before this could be tested, Figure 18). It is possible that the current decreased at first due to the sudden onset of shear stress but then continued to decrease due to the blocker application. However, as the current reduction upon perfusion start does not reach a plateau, this cannot be determined. The ongoing current reduction after the perfusion with the blocker could be explained by a local accumulation of the blocker, which further reduced the current amplitude. However, during the duration (>7 min) of the experiment, the series resistance (Rser) increased gradually (Figure 18B). According to Ohm's

law (V=I/R), an increase in the series resistance reduces the current amplitude. To analyze how much the Rser increase contributed to the current decline, the Rser increase over time was compared to the current decline over time. For this, the formula $\frac{1}{\frac{\text{Rser}}{\text{Rsermin}}}$ was applied to produce a downward slope comparable to the current decline (Rsermin= minimum series resistance). This revealed that while the Rser increase was considerably large and likely contributed to the observed current decline, it cannot account for the entirety of the current decline in all cells. For example, in cell 247, the Rser remained stable, but the current declined continuously. Interestingly, cell 245 showed a very slowly inactivating current before application of the perfusion that inactivated more rapidly during perfusion with ECS + TTX and even faster after application of the VX-548 blocker (Figure 18A). Such a slowly inactivating current is characteristic for $Na_v1.8$ and this slowly inactivating component seems to be affected by both the perfusion shear stress and the presence of the VX-548 blocker. These results indicate that $Na_v1.8$ current could be present at least in small amounts in some cells.

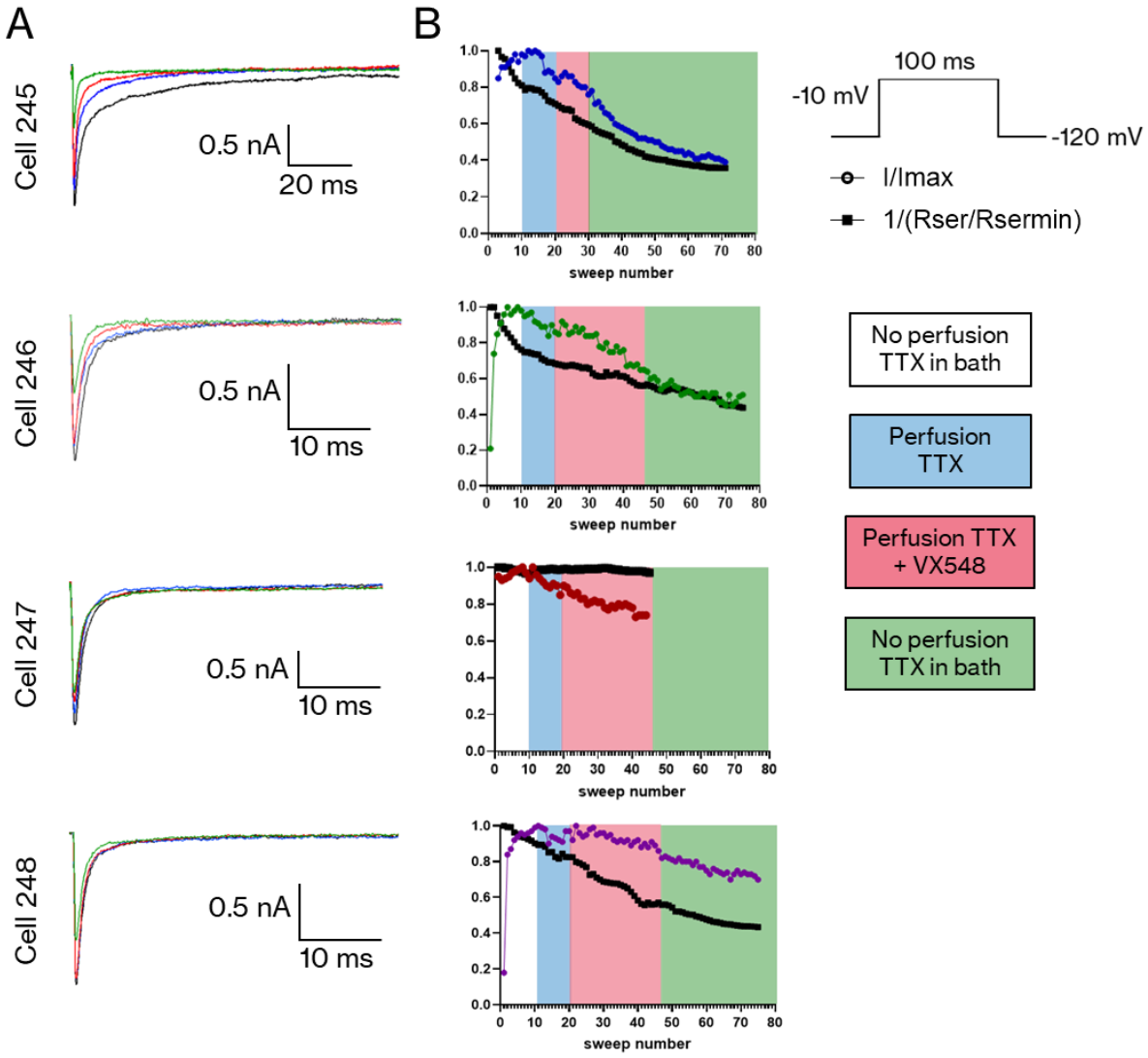

Figure 18 Application of $Na_v1.8$ blocker VX-548 via gravity-driven perfusion to iPSC-SN. Chambers-differentiated Ctrl_1 iPSC-SN, voltage clamped at DIV63. A) Representative current traces of four individual cells before application of perfusion with 500 nM TTX in the bath (black),

during application of perfusion with ECS + 500 nM TTX (blue), during application of perfusion with ECS + 500 nM TTX + 100 nM $Na_v1.8$ blocker VX-548 (red) and after the perfusion was stopped (green). B) Current reduction plotted over increasing sweep number in four different cells of separate dishes with ECS + 500 nM TTX in the bath and no perfusion, followed by perfusion with ECS +500 nM TTX (marked in blue), followed by perfusion with 500 nM TTX + 100 nM VX-548 (marked in red), followed by no perfusion (marked in green). Current (I) was normalized to the maximum inward current (Imax). 1/(Rser/Rsermin) was plotted to indicate the series resistance (Rser) changes in relation to the current changes.

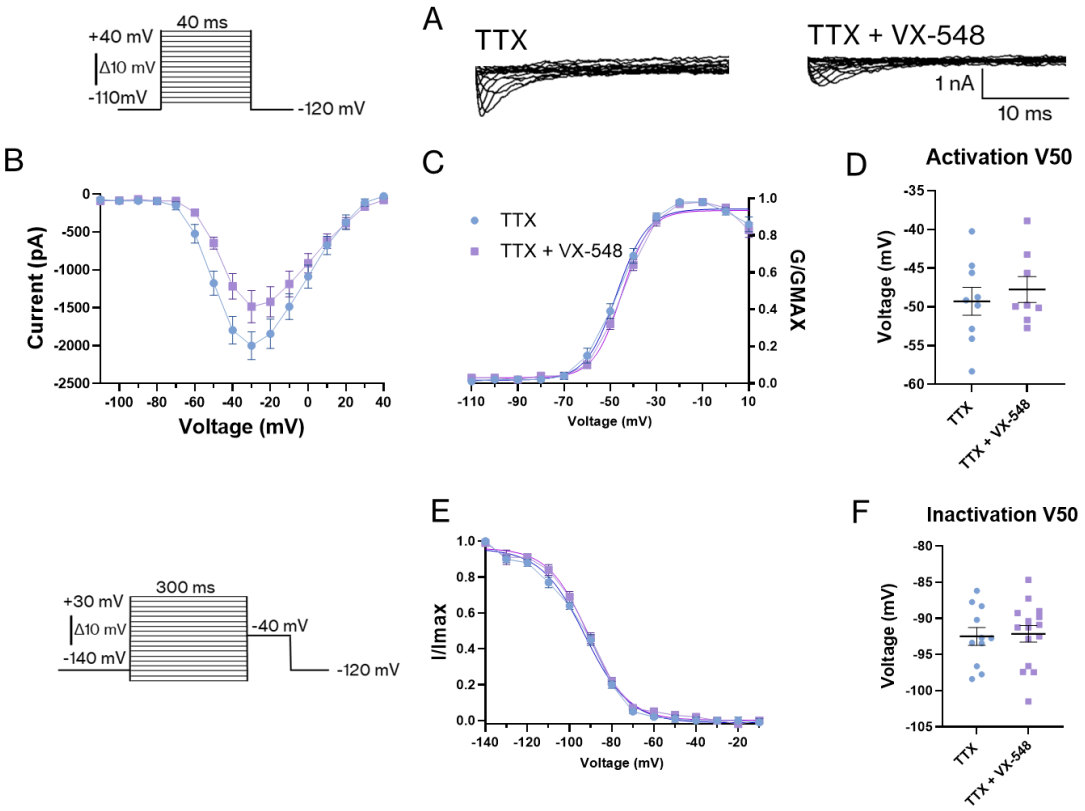

Figure 19 TTXr currents of Chambers-differentiated iPSC-SN with $Na_v1.8$ blocker VX-548 in the bath. Ctrl_1 iPSC-SN were patch clamped at DIV55-64 of differentiation. A) Representative current traces with TTX or TTX + VX-548 in the bath solution. B) IV curve. C) Conductance (G) curve normalized to the maximum conductance displayed with a line connecting the data points (lighter colour) and a Boltzmann fit (darker colour). D) Voltage of half activation (V50) was determined with a Boltzmann fit. E) Inactivation curve normalized to maximum current (I/Imax) displayed with a line connecting the data points (lighter colour) and a Boltzmann fit (darker colour). F) Voltage of half inactivation (V50) was determined with a Boltzmann fit. N=1; n=12. TTX 500 nM, VX548 100 nM.

To quantify the changes in Na_v current and gating upon application of VX-548, iPSC-SN of the cell line Ctrl_1 differentiated via the Chambers or the NGN1 protocol were voltage clamped with 500 nM TTX and 100 nM VX-548 in the bath. For iPSC-SN differentiated with the Chambers protocol, the mean peak current was 515 pA smaller in the VX-548 population (Figure 19A,B, Table 16). However, this difference was not statistically significant. Furthermore, the activation and fast

inactivation curves did not differ significantly in their V50 or slope (Figure 19C,D,E,F, Table 16). For the NGN1 differentiated Ctrl_1 iPSC-SN, there was no statistical difference in the mean peak current or the V50 or slope of activation (Figure 20A,B,C,D, Table 16). However, the V50 of inactivation was significantly shifted towards more depolarized potentials with VX-548 in the bath (TTX -95.57 ± 3.7, VX-548 -85.17 ± 2) (Figure 20E,F, Table 16). This is noteworthy, as $Na_v1.8$ inactivates at more hyperpolarized potentials compared to $Na_v1.5$ and $Na_v1.9$ and therefore blocking $Na_v1.8$ current should hyperpolarize the inactivation curve. Interestingly, the previously mentioned biphasic inactivation persists upon application of the $Na_v1.8$ blocker (Figure 17E). Overall, the experiments with the $Na_v1.8$ blocker VX-548 at 100 nM could not conclusively prove the channel's presence in iPSC-SN in either differentiation protocol. Next, the presence of functional $Na_v1.9$ current was investigated in iPSC-SN.

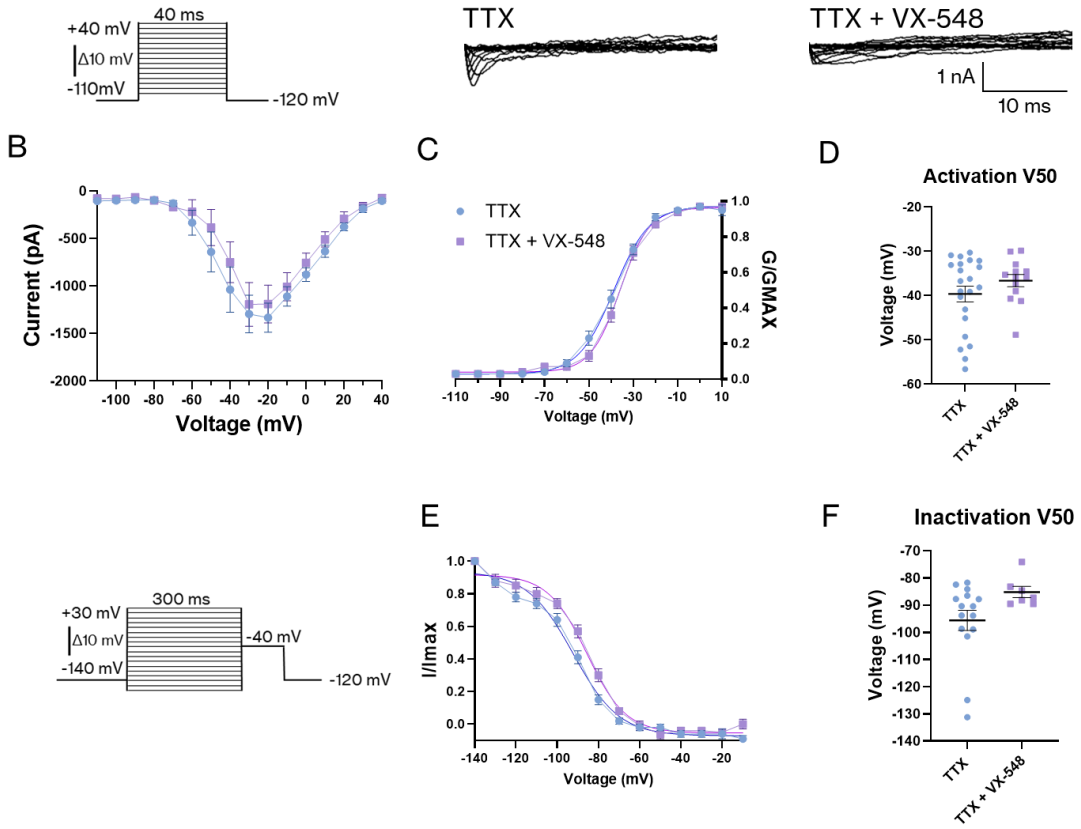

Figure 20 TTXr currents of NGN1-differentiated iPSC-SN with $Na_v1.8$ blocker VX-548 in the bath. Ctrl_1 iPSC-SN were patch clamped at DIV55-64 of differentiation. A) Representative current traces with TTX or TTX + VX-548 in the bath solution. B) IV curve. C) Conductance (G) curve normalized to the maximum conductance displayed with a line connecting the data points (lighter colour) and a Boltzmann fit (darker colour). D) Voltage of half activation (V50) was determined with a Boltzmann fit. E) Inactivation curve normalized to maximum current (I/Imax) displayed with a Boltzmann fit (darker colour). F) Voltage of half inactivation (V50) was determined with a Boltzmann fit. N=1; n=12 . TTX 500 nM, VX548 100 nM. N=1; n=9-23.

Table 16 Activation and inactivation parameters of iPSC-SN with $Na_v1.8$ blocker VX-548 in the bath. iPSC-SN were patch clamped at DIV55-64 of differentiation. The voltage of half activation/inactivation (V50) and slope were determined with a Boltzmann fit. Data is presented as mean ± SEM and statistical significance between iPSC-SN voltage clamped in the presence of 500 nM TTX or 500 nM TTX + 100 nM VX548 of the same differentiation protocol was analyzed with a Mann-Whitney test. *p≤0.05 **p≤0.01 ***p≤0.001 ****p≤0.0001.

	Chambers Ctrl_1		NGN1 Ctrl_1	
	TTX	TTX + VX548	TTX	TTX + VX548
Activation				
Peak current (pA)	-2000 pA ± 184.3	-1485 ± 214.1	-1332 ± 154.3	-1190 ± 199.4
V50 (mV)	-49.27 ± 1.8	-47.75 ± 1.7	-39.63 ± 1.8	-36.62 ±1.4
Slope	4.97 ± 0.4	5.18 ± 0.7	5.76 ± 0.3	6.04 ± 0.6
n	10	11	22	13
Inactivation				
V50 (mV)	-92.48 ± 1.2	-92.14 ± 1.1	-95.57 ± 3.7*	-85.17 ± 2*
Slope	-10.08 ± 0.6	-9.57± 0.7	-13.46 ± 2.3	-10.79 ± 1.8
n	11	15	15	8

5.8 Electrophysiological isolation of $Na_v1.9$ current

To assess the presence of $Na_v1.9$ current in iPSC-SN, a patch clamp protocol is required that can isolate $Na_v1.9$ current from other TTXr currents. $Na_v1.9$ activates and inactivates at more hyperpolarized potentials compared to $Na_v1.8$, and this difference in gating kinetics can be leveraged to separate the currents generated by these two channels. To this end, two different patch-clamp protocols were evaluated.

The first approach tested was the TTXr-$Na_v1.9^{inact}$ protocol, a method that has previously been published by the Waxman laboratory (Cummins et al., 1999; Huang et al., 2014). This protocol involves initially measuring the total TTXr current using a series of incremental voltage steps. Subsequently, the TTXr-$Na_v1.9^{inact}$ current is recorded under identical conditions with the modification that a prepulse is applied at a potential where only $Na_v1.9$ inactivates, but $Na_v1.8$ remains in an available state. By subtracting the TTXr-$Na_v1.9^{inact}$ current from the total TTXr current, the resulting trace represents solely the $Na_v1.8$ current. The isolated $Na_v1.8$ current can then be subtracted from the TTXr-total current to isolate the $Na_v1.9$-mediated current. Two variants of this protocol were tested, named TTXr-$Na_v1.9^{inact}$a and TTXr-$Na_v1.9^{inact}$b.

When applying the TTXr-$Na_v1.9^{inact}$a protocol to iPSC-SN using a prepulse of -60 mV, partial inactivation of $Na_v1.8$ was observed, which was visible by the presence of a transient peak current in the TTXr-total - TTXr-$Na_v1.9^{inact}$ – subtracted current (Figure 21A). This occurred despite the incorporation of a 100 ms recovery period at the holding potential. Additionally, no distinct persistent $Na_v1.9$ current component was detected in the TTXr-total current generated by iPSC-SN. To validate the protocol, the same experiment was conducted in mDRG neurons, a system known to express both $Na_v1.8$ and $Na_v1.9$ currents. In a similar approach (TTXr-$Na_v1.9^{inact}$b), the holding potential was changed to -60 mV to inactivate $Na_v1.9$, followed by a 100 ms recovery period at -120 mV, after which the total TTXr current was measured at a holding potential of -120 mV. However, this adapted protocol also resulted in a partial inactivation of $Na_v1.8$. To mitigate this issue, more hyperpolarized prepulse potentials of -80 mV and -90 mV were tested, along with an extended recovery period of 500 ms (Figure 21B).

A potential refinement of the TTXr-$Na_v1.9^{inact}$ protocol would involve applying an inactivation protocol for each individual cell to determine the precise voltage at which $Na_v1.8$ inactivates and then subsequently applying a more hyperpolarized potential as a prepulse potential to inactivate $Na_v1.9$ but not $Na_v1.8$. However, given the already extended duration of the voltage-clamp protocol required for $Na_v1.9$ isolation, an alternative approach was pursued.
Leipold et al. previously demonstrated that performing a series of test pulses at hyperpolarized potentials selectively generates $Na_v1.9$ current (Leipold et al., 2013). This approach relies on the use of cesium fluoride (CsF) in the intracellular solution, which hyperpolarizes the gating kinetics of $Na_v1.9$ (Coste et al., 2004). When applying this protocol, clear and reproducible $Na_v1.9$ currents were recorded in small-diameter mDRG neurons (Figure 21C). Based on these results, this method was subsequently used in further experiments to assess the presence of $Na_v1.9$ currents in iPSC-SN.

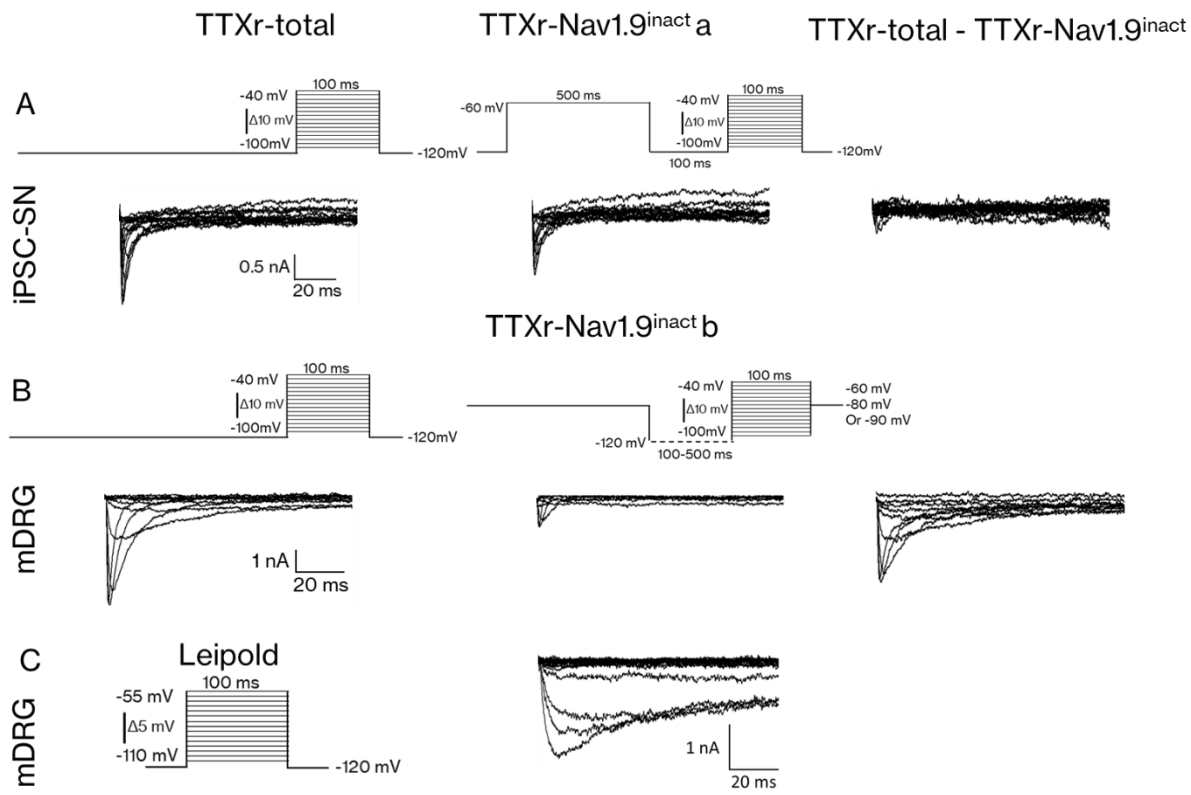

Figure 21 Voltage clamp protocols to isolate $Na_v1.9$ current. A) TTXr-total and TTXr-$Na_v1.9^{inact}$a protocol and the representative current traces for the two protocols and the subtracted current trace in iPSC-SN. B) Voltage clamp protocol of TTXr-total and TTXr-$Na_v1.9^{inact}$b and the representative current traces for the two protocols and the subtracted current trace in mDRG. C) Leipold protocol and representative current trace in mDRG.

5.9 $Na_v1.9$ current not clearly detectable in iPSC-SN

To investigate the functional presence of $Na_v1.9$ in iPSC-SN, the previously tested Leipold voltage clamp protocol was used. mDRG neurons served as a positive control. Persistent current with an amplitude of 300 pA to 3 nA was found in almost all small-diameter mDRG neurons at hyperpolarized potentials (Figure 22A). $Na_v1.9$ current was identified according to the current shape, its very slow decay and large persistent component and its presence at potentials between

-75 and -55 mV. In iPSC-SN differentiated with the Chambers, NGN1 or NBI protocol, such a persistent current component could not be identified. A slowly inactivating current component could sometimes be observed, but it inactivated maximum 30 ms after the onset of the test pulse, a characteristic more commonly known for $Na_v1.8$ current than $Na_v1.9$ current. Quantification of the persistent current in relation to the peak current revealed that mDRG neurons showed a persistent current of 75 % of the peak current at the middle of the current trace and 61 % at the end of the trace, underlining the slow inactivation of this current (Figure 22B). iPSC-SN of all three differentiation protocols of two different cell lines each only showed a mean persistent current amplitude of 0-5 % of the peak current 40-50 ms after the test pulse onset and between -6 to +3 % at 89-99 ms. The negative percentages occur when there is a positive outward current during the segment where the persistent current is measured, which can usually be attributed to leak current. The difference between the mDRG neurons and iPSC-SN was statistically significant for every cell line (analyzed with one-way ANOVA followed by a Tukey's multiple comparison test (if normally distributed) or a Kruskal-Wallis test followed by Dunn's multiple comparison test (if not normally distributed).

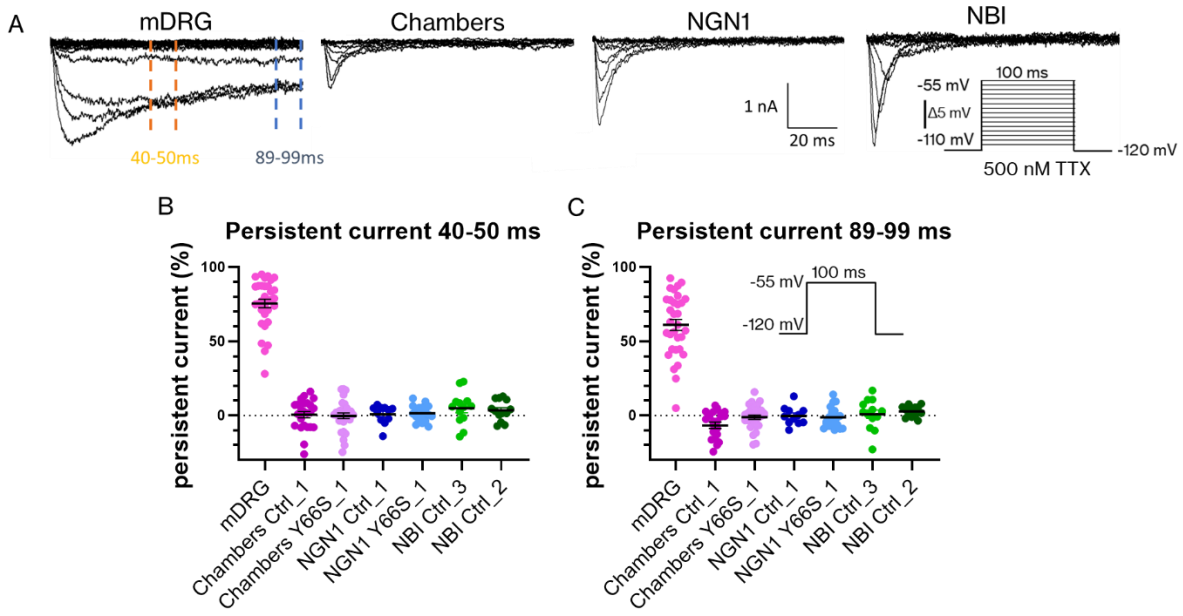

Figure 22 $Na_v1.9$ current in mDRG & iPSC-SN. iPSC-SN were patch clamped at DIV55-64. mDRG neurons were patch clamped 20-52 h post-isolation. A) Representative current traces of mDRG, and iPSC-SN differentiated with the Chambers, NGN1 and NBI protocol. B,C) Quantification of the persistent current normalized to the peak current between 40-50 ms and 89-99 ms of the test pulse at -55 mV. Data is presented as mean ± SEM.

In an attempt to increase the $Na_v1.9$ current size, NGN1-differentiated iPSC-SN of the Ctrl_1 cell line underwent maturation for an extended period of time and were voltage clamped with known $Na_v1.9$ enhancers. $Na_v1.9$ is known to be expressed later in embryonal development of sensory neurons compared to other Na_v channels (Benn et al., 2001). To assess if $Na_v1.9$ current may be present at a later time point during the maturation process, NGN1-differentiated iPSC-SN were voltage clamped at 8 and 12 weeks of maturation. Other research groups have shown that

incubation with the inflammatory mediator Prostaglandin E2 (PGE2) or incubation with the pharmaceutical agent Cromolyn sodium (CS) or addition of GTP-ɣ-S to the ICS increases the $Na_v1.9$ current in rodent DRG and heterologous expression systems (Baker et al., 2003; Rush & Waxman, 2004) (unpublished data Margaux Theys, Molecular Physiology and Neurophysics group, University of Ghent, presented 2023 at annual meeting society of general physiologists). Therefore, iPSC-SN matured for 12 weeks were incubated for one hour with 10 µM PGE2 and 1 µM CS in the media at 37°C, before voltage clamp with 500 µM GTP-ɣ-S in the patch pipette was performed. After 12 weeks of maturation, the NGN1-differentiated iPSC-SN appeared to have an increasingly soft and permeable membrane, which made it difficult to seal at a high resistance. This resulted in increased leak currents and a lower signal-to-noise ratio, as visible in the representative traces (Figure 23C). The peak current amplitude was almost twice as high at week 12 compared to week 8 (Figure 23A, Table 17) and the V50 of activation was shifted by almost 8 mV to hyperpolarized potentials. However, these changes were not significant and only tested in a small sample size of the iPSC-SN patched in week 12 without $Na_v1.9$ enhancers. Interestingly, in a non-significant trend, the assumed $Na_v1.9$ enhancers PGE2, CS and GTP-ɣ-S decreased the peak current and depolarized the V50 compared to both week 8 and week 12. In terms of $Na_v1.9$ current, the extended maturation duration with or without the addition of the $Na_v1.9$ enhancers failed to result in a visible $Na_v1.9$ current (Figure 23C) or quantifiable $Na_v1.9$ current (Figure 23D, E). In the few cells where the persistent current was a positive percentage of the peak current, this was mainly caused by leak artefacts. This can also be seen in the negative percentages that can be reached with the persistent current normalized to the peak current, which are caused by outward current at the point of persistent current measurement.

To summarize, no clear $Na_v1.9$ current could be identified in iPSC-SN of any differentiation protocol. Furthermore, an extended maturation period or the application of PGE2, GTP-ɣ-S and CS did not produce observable or quantifiable $Na_v1.9$ currents in NGN1-derived iPSC-SN. It should be noted that this was only examined in one cell line of one differentiation and at a low n, and therefore only a trend could be observed.

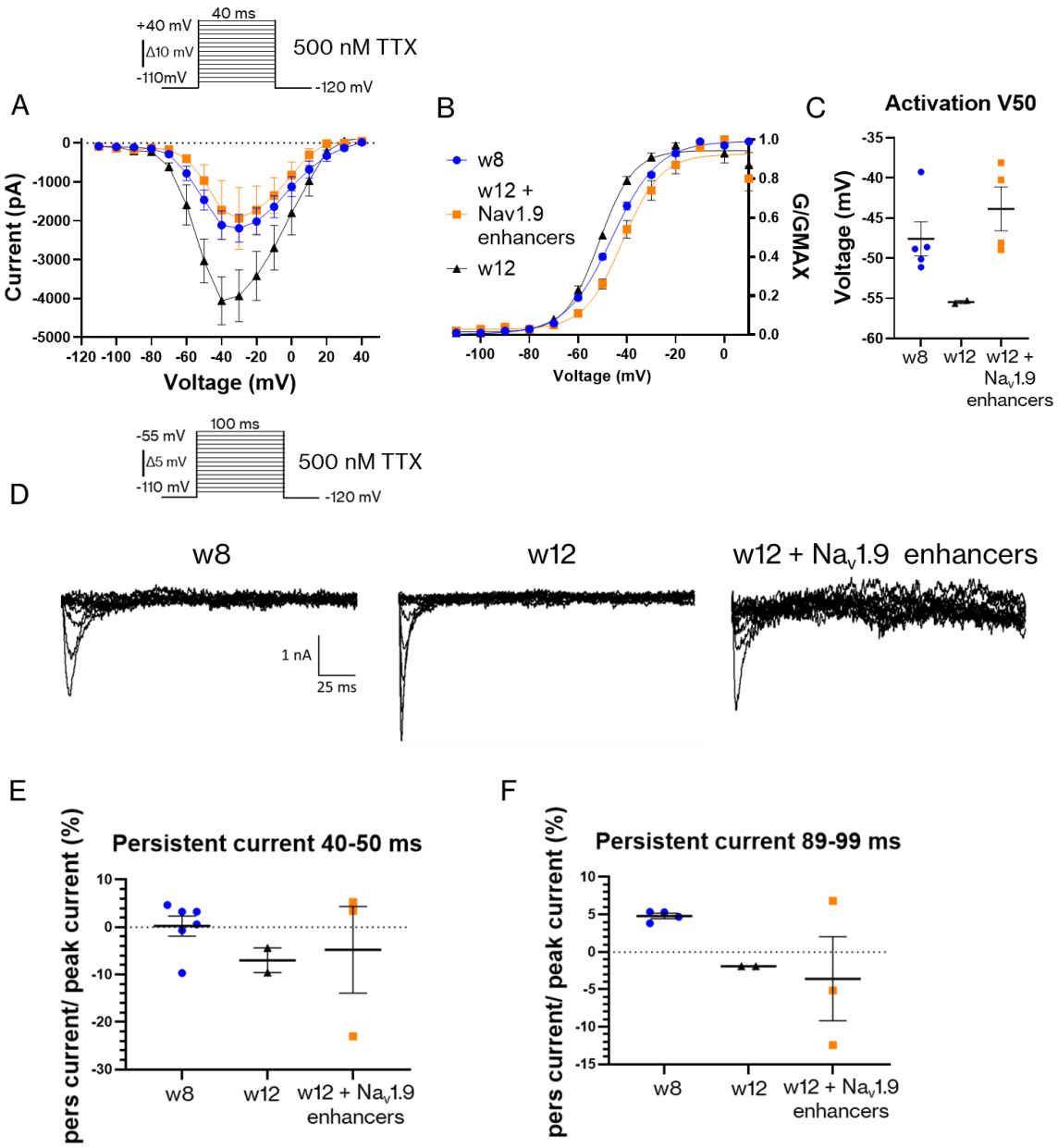

Figure 23 TTXr and $Na_v1.9$ current in iPSC-SN after extended neuronal maturation with $Na_v1.9$ enhancers. NGN1-differentiated iPSC-SN of Ctrl_1 were patch clamped at DIV55-64 (w8) or DIV84-90 (w12). Voltage clamp was performed in the absence or presence of the $Na_v1.9$ enhancers prostaglandin E2, cromolyn sodium and GTP-ɣ-S. A,B) IV curve and conductance (G) curve normalized to the maximum conductance displayed with a Boltzmann fit. C) Voltage of half-activation (V50) for each cell was determined with a Boltzmann fit. D) Representative current traces at w8, w12 and w12 with $Na_v1.9$ enhancers showed no $Na_v1.9$-like persistent current. E,F) Quantification of persistent current normalized to the peak current at -55 mV at 40-50 ms and 89-99 ms after test pulse onset. Data is presented as mean ± SEM.

Table 17 Voltage dependence of activation characteristics after extended neuronal maturation with $Na_v1.9$ enhancers. NGN1-differentiated iPSC-SN of Ctrl_1 were patch clamped at DIV55-64 (w8) or DIV84-90 (w12) and voltage clamped in the absence or presence of the $Na_v1.9$ enhancers prostaglandin E2, cromolyn sodium and GTP-ɣ-S. The voltage of half activation(V50) and slope were determined with a Boltzmann fit. Data is presented as mean ± SEM and statistical significance was analyzed with a Kruskal-Wallis test followed by Dunn's multiple comparison test. *p≤0.05 **p≤0.01 ***p≤0.001 ****p≤0.0001.

	Week 8	Week 12	Week 12 + $Na_v1.9$ enhancers
Activation			
Peak current (pA)	-2193.4 ± 258.5	-4057.2 ±618.2	-1938.2
V50 (mV)	-47.6 ± 2.1	-55.5 ± 0.2	-43.9 ± 2.7
Slope	7.2 ± 0.8	4.7 ± 0.8	5.9 ± 1
n	6	2	4

5.10 Action potential shoulder and firing frequency altered in $Na_v1.9$-Y66S Chambers-differentiated iPSC-SN

After not observing a clear phenotype of the $Na_v1.9$_Y66S mutation in voltage clamp and not being able to identify substantial $Na_v1.9$ current, I investigated if a phenotypic difference would be visible between the patient and the age- and gender-matched control cell line in current clamp.
In the Chambers-differentiated iPSC-SN, both the Ctrl_1 and Y66S_1 cell lines fired mature action potentials and had an RMP comparable to native DRG neurons (Davidson et al., 2014; Zurek et al., 2024) (Figure 24A,B). When comparing the neuronal properties of Y66S_1 and Ctrl_1 differentiated with the Chambers protocol, the RMP (Ctrl_1 -65.9 ± 0.9, Y66S_1 -64.6 ± 1.3 mV) and rheobase (Ctrl_1 46.9 ± 4.7, Y66S_1 36.4 ± 4.4 pA) were comparable (Figure 24B,C). Furthermore, the amplitude (Ctrl_1 106.8 ± 1, Y66S_1 105.6 ± 1.5 mV), voltage threshold (Ctrl_1 -57.9 ± 0.5, Y66S_1 -58.4 ± 0.6 mV) and afterhyperpolarization (Ctrl_1 -71.9 ± 0.6, Y66S_1 -71.7 ± 0.6 mV) were not significantly different between the two cell lines (Figure 24D,E, I). To ensure that the cellular conditions were comparable for the patch clamp experiments, the input resistance and cell capacitance were analyzed. While no difference in input resistance was observed (Ctrl_1 231.4 ± 14.6, Y66S_1 223.1 ± 14.1), a significantly higher cell capacitance was observed in the patient cell line (Ctrl_1 34.2 ± 2.6, Y66S_1 44.4 ± 3.6) (Figure 24J,K). However, cellular capacitance can best be determined by the patch clamp amplifier for isolated cells, but the iPSC-SN grow on a dense network of neurites, leading to a potential distortion of capacitance values. Therefore, the input resistance is a more reliable parameter to assess a difference in electrophysiological conditions and this was not different between groups. The half-width (Ctrl_1 2.7 ± 1.8, Y66S_1 2.1 ± 0.1 ms) and slope upstroke (Ctrl_1 11.7 ± 0.9, Y66S_1 8.1 ± 0.9 V/s) were significantly lower in the patient cell line, while the time to peak was significantly higher (Ctrl_1 21.7 ± 1.8, Y66S_1 38.7 ± 3.2 ms) (Figure 24F, G, H). These findings indicate a difference in action potential shape.

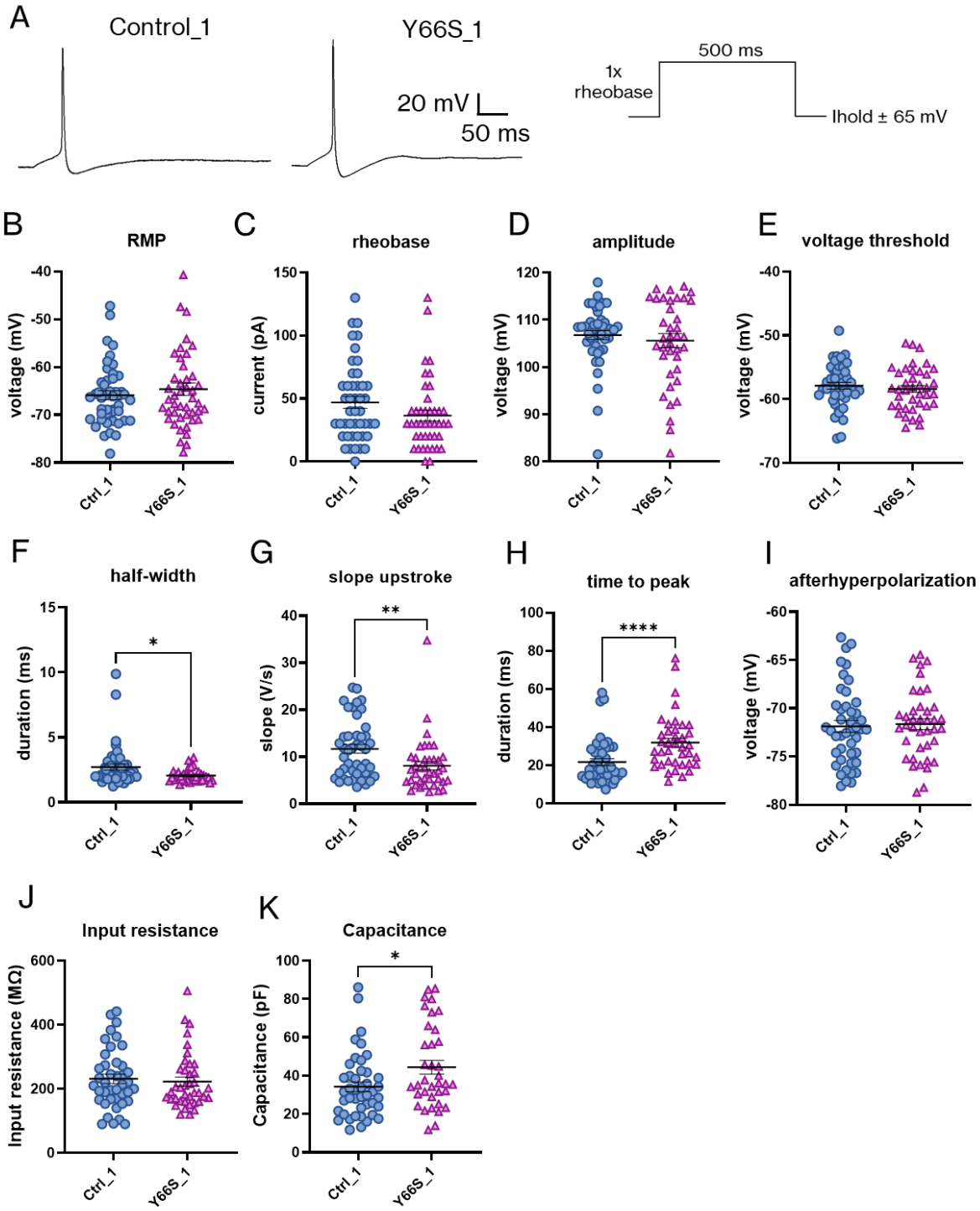

Figure 24 Neuronal excitability and action potential characteristics of control and $Na_v1.9$_Y66S iPSC-SN differentiated with the Chambers protocol. iPSC-SN were patch clamped at DIV55-64. The first action potential fired at the rheobase was used for analysis. A) Representative action potential traces of Ctrl_1 and Y66S_1. B) Resting membrane potential (RMP). C) Rheobase. D) Action potential amplitude. E) Action potential voltage threshold. F) Action potential half-width. G) Action potential slope upstroke. H) Action potential time to peak.

I) Action potential afterhyperpolarization. J) Input resistance was determined by calculating the voltage change upon administration of two hyperpolarized current injections with a delta of 50 pA. K) Cell capacitance was measured by the patch clamp amplifier (C-slow). Data is presented as mean ± SEM and was analyzed for statistically significant differences with a Mann-Whitney test. N=3; n= 39-44. *p≤0.05 **p≤0.01 ***p≤0.001 ****p≤0.0001.

One important parameter of the action potential shape is the action potential shoulder, which is defined as a change in the slope during the repolarizing phase of the action potential, creating a broader action potential (for more details see section 4.4.3, Figure 9). A recent study has indicated a role of $Na_v1.9$ in the prominence of the action potential shoulder (Köster et al., 2025). Therefore, it was specifically analyzed here. As visible in the overlay of all measured action potentials in Figure 25A, the neurons of the Ctrl_1 cell line showed action potential shoulders more often and more pronounced. To quantify the amount of neurons with an action potential shoulder and the shape of the shoulder, the change in slope during the repolarization phase was analyzed on a scale from zero to one, where one is a change from a negative slope to a slope parallel to the X-axis and a pronounced shoulder and zero is no change in slope and no action potential shoulder (see section 4.4.3, Figure 9). 40 % of Ctrl_1 neurons but only 12.2 % of Y66S_1 neurons showed an action potential shoulder. The quantification of the shoulder prominence (i.e. how shallow the slope of the action potential is during the shoulder) (Ctrl_1 0.2 ± 0.05, Y66S_1 0.05 ± 0.03) and the shoulder width (Ctrl_1 1.9 ± 0.6, Y66S_1 0.2 ± 0.2 ms) revealed a statistical significance between the cell lines (Figure 25B,C).

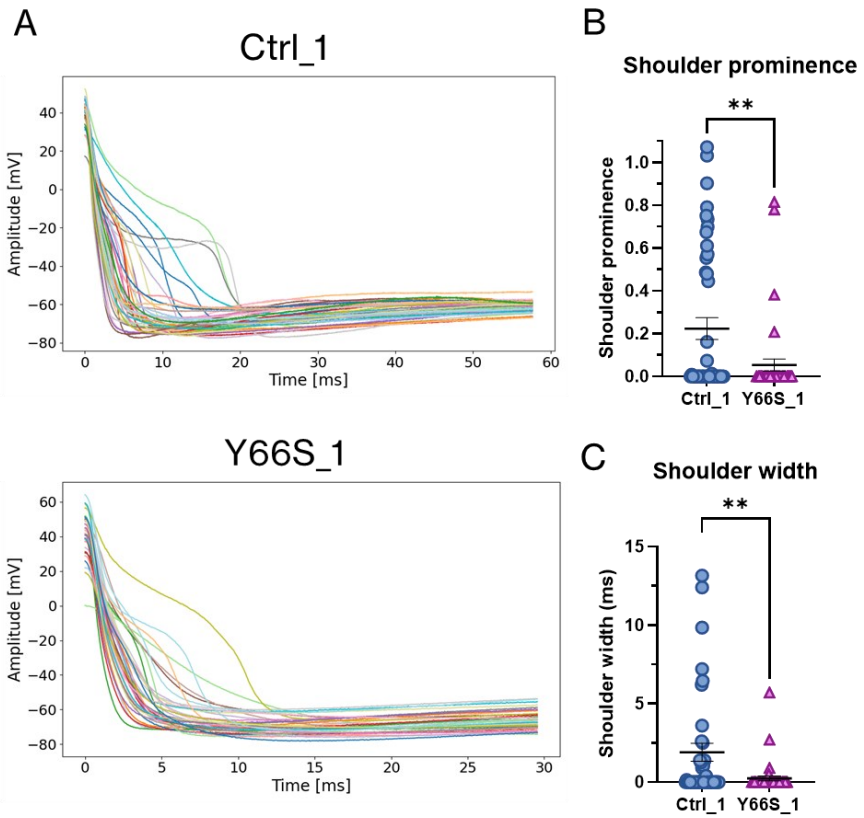

Figure 25 Action potential shoulders in control and $Na_v1.9$_Y66S iPSC-SN differentiated with the Chambers protocol. iPSC-SN were patch clamped at DIV55-64. The first action potential fired at rheobase was used for analysis. A) Action potential traces of individual iPSC-SN (indicated

in different colours) of the Ctrl_1 and Y66S_1 cell line. Traces are shown starting from the action potential maximum and show the repolarization phase, including the shoulder. B) Action potential shoulder prominence was defined as the normalized ratio between the maximum and minimum slope of the shoulder and was calculated on a scale from zero to one, where one is a change from a negative slope to a horizontal slope and a pronounced shoulder and zero is no change in slope and no action potential shoulder. C) Action potential shoulder width was measured between the first root of the second derivative of the action potential (i.e., the first inflection of the action potential downstroke) and the largest local minimum of the first derivative after the shoulder beginning. Data is presented as mean ± SEM and was analyzed for statistically significant differences with a Mann-Whitney test. N=3; n= 41-45. *p≤0.05 **p≤0.01 ***p≤0.001 ****p≤0.0001.

To further analyze potential differences between the patient and control cell line, the firing frequency of the iPSC-SN was analyzed. It was observed that in the Chambers-differentiated sensory neurons, the firing frequency was significantly increased in the Y66S_1 cell line compared to the Ctrl_1 cell line (Figure 26A). An analysis of the firing behaviour of the cells revealed that almost twice as many neurons in the patient cell line showed a tonic firing frequency that fired more than five action potentials upon stimulation (Figure 26B).
To summarize, in the Chambers-differentiated iPSC-SN, significant differences were found between the Y66S_1 patient and the Ctrl_1 cell line in regards to the action potential shape, including the half-width, time to peak, slope upstroke, shoulder prominence and width and the firing frequency.

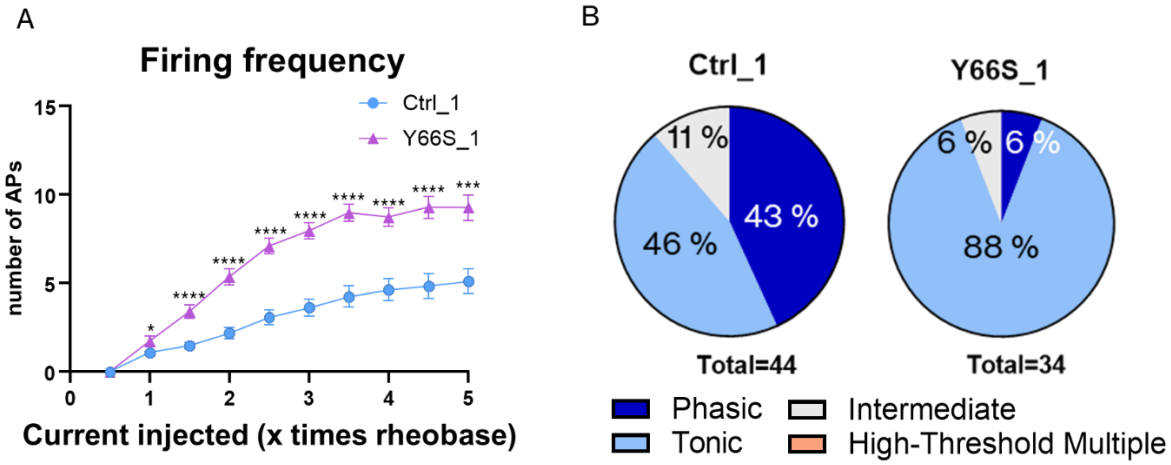

Figure 26 Firing frequency in control and $Na_v1.9$_Y66S iPSC-SN differentiated with the Chambers protocol. iPSC-SN were patch clamped at DIV55-64. A) Firing frequency. Number of action potentials counted with increasing amounts of current injected (0.5x rheobase increments). Data is presented as mean ± SEM and was analyzed with a Mann-Whitney test. N=3; n= 41-45. *p≤0.05 **p≤0.01 ***p≤0.001 ****p≤0.0001. B) Action potential firing behaviour is divided into phasic (1 action potential), tonic (>5 action potentials), intermediate (2-4 action potentials) and high-threshold multiple (1 action potential at low current injections, >5 at high current injections). N=3; n= 41-45.

5.11 Neuronal excitability was comparable between $Na_v1.9$-Y66S and control NGN1- differentiated iPSC-SN

To establish if the phenotypic trend observed in the Chambers-differentiated Y66S_1 patient cell line was reproducible in iPSC-SN generated by a different protocol, I differentiated the patient and control cell line again, employing the NGN1 protocol. Here, I additionally included the Y66S_2 cell line. The Y66S_2 iPSC line was derived from the son of the Y66S_1 patient, who has also been diagnosed with SFN, but does not report ongoing neuropathic pain symptoms. In addition, we pooled six iPSC clones of the same cell line together to limit the effect of single clone variation on the results. Similar to the iPSC-SN generated with the Chambers protocol, the NGN1-differentiated sensory neurons of all three cell lines fired mature action potentials and had a resting membrane potential fitting for sensory neurons (Ctrl_1 -70.7 ± 0.8, Y66S_1 -70.2 ± 1.2, Y66S_2 ± -69.2 mV) (Figure 27A,B). The rheobase was on average 17.5/15.8 pA lower in the Y66S_1 cell line compared to the control and other patient, but this was non-significant (Ctrl_1 83.5 ± 6.8, Y66S_1 66 ± 5.4, Y66S_2 81.8 ±5.9 pA) (Figure 27C). The action potential amplitude was significantly lower in the Y66S_2 cell line compared to the other two cell lines (Ctrl_1 107.8 ± 0.8, Y66S_1 105.9 ± 1, Y66S_2 103.4 ± 1), but it is questionable if a difference of 2-4 mV in action potential amplitude would have physiological relevance for the neuronal excitability of these cells (Figure 27D). On the other hand, the voltage threshold (Ctrl_1 -55.5 ± 0.5, Y66S_1 -55.6 ± 0.6, Y66S_2 -55.3 ± 0.8 mV), half-width (Ctrl_1 1.9 ± 0.1, Y66S_1 2.2 ± 0.2, Y66S_2 2.4 ± 0.2 ms), time to peak (Ctrl_1 35.6 ± 4.3, Y66S_1 38.7 ± 3.2, Y66S_2 35.4 ± 5.4 ms), slope upstroke (Ctrl_1 9.9 ± 0.8, Y66S_1 8.6 ± 0.7, Y66S_2 9.6 ± 0.8 V/s) and afterhyperpolarization (Ctrl_1 -69.8 ± 0.6, Y66S_1 -69.8 ± 0.6, Y66S_1 -63.4 ± 0.7) were comparable between cell lines (Figure 27D, E, F, G, H,I). The input resistance and cell capacitance were not different between cell lines (Figure 27J,K).

Next, the action potential shoulder was analyzed as described in section 4.4.3 (Figure 9). In all three cell lines, the majority of cells showed a rapid repolarization with no action potential shoulder; multiple cells showed a slow repolarization, but only 4 % of Ctrl_1, 5 % of Y66S_1 and 10 % of Y66S_2 iPSC-SN showed a change in the repolarization slope as is characteristic for an action potential shoulder (Figure 28A). Quantification of the shoulder prominence (Ctrl_1 0.01 ± 0.008, Y66S_1 0.02 ± 0.02, Y66S_2 0.03 ± 0.02) and the shoulder width (Ctrl_1 0.07 ± 0.05, Y66S_1 0.2 ± 0.2, Y66S_2 0.2 ± 0.1 ms) showed no significant difference between the groups (Figure 28B,C).

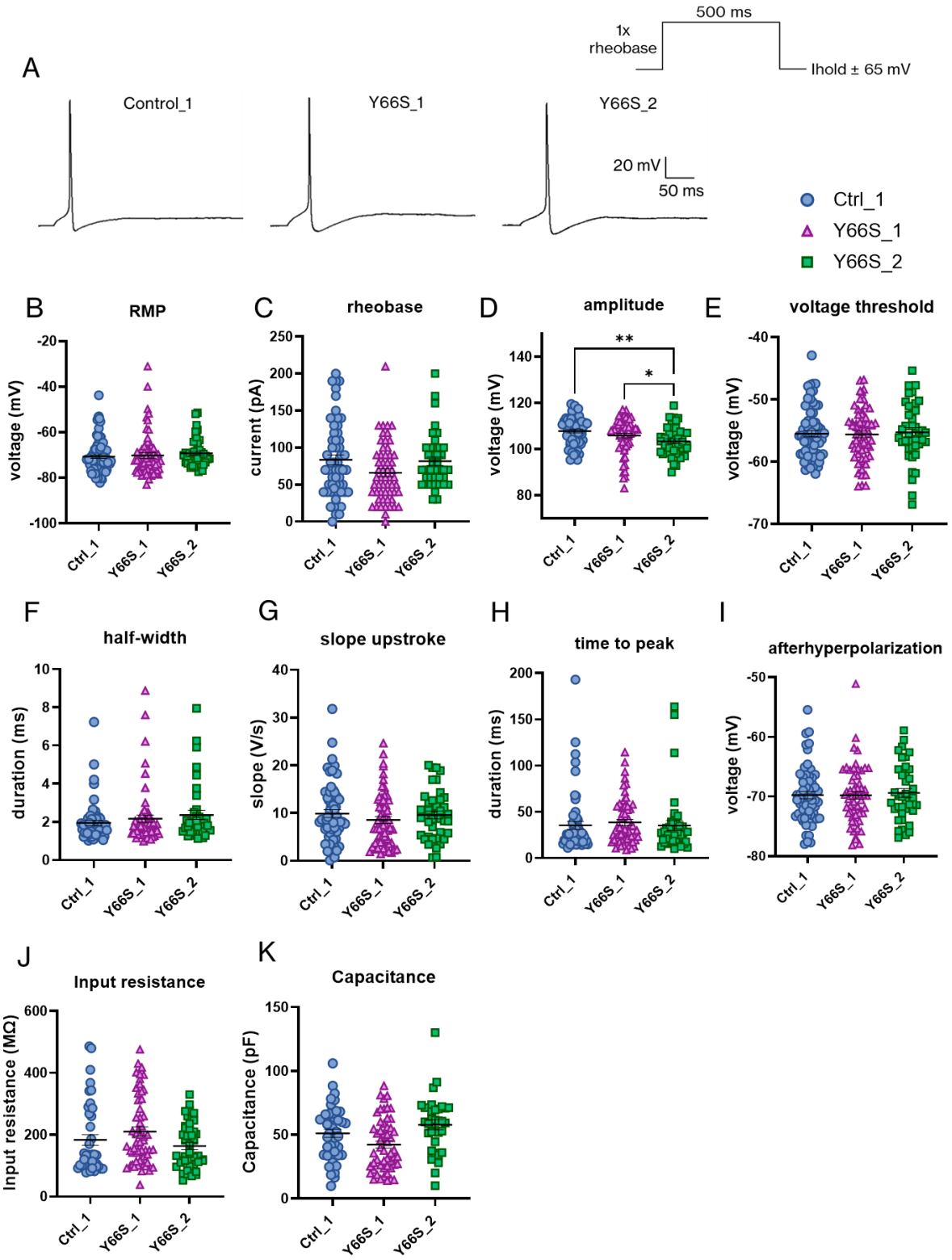

Figure 27 Neuronal excitability and action potential characteristics of control and $Na_v1.9$_Y66S iPSC-SN differentiated with the NGN1 protocol. iPSC-SN were patch clamped at DIV55-64. The first action potential fired at rheobase was used for analysis. A) Representative action potential traces of Ctrl_1, Y66S_1 and Y66S_2. B) Resting membrane potential (RMP). C) Rheobase. D) Action potential amplitude. E) Action potential voltage threshold. F) Action potential

half-width. G) Action potential slope upstroke. H) Action potential time to peak. I) Action potential afterhyperpolarization. J,K) Input resistance was determined by calculating the voltage change upon administration of two hyperpolarized current injections with a delta of 50 pA. K) Cell capacitance was measured by the patch clamp amplifier (C-slow). Data is presented as mean ± SEM and was analyzed for statistically significant differences with a Kruskal-Wallis test followed by Dunn's multiple comparison test. N=3, n=27-59. *p≤0.05 **p≤0.01 ***p≤0.001 ****p≤0.0001.

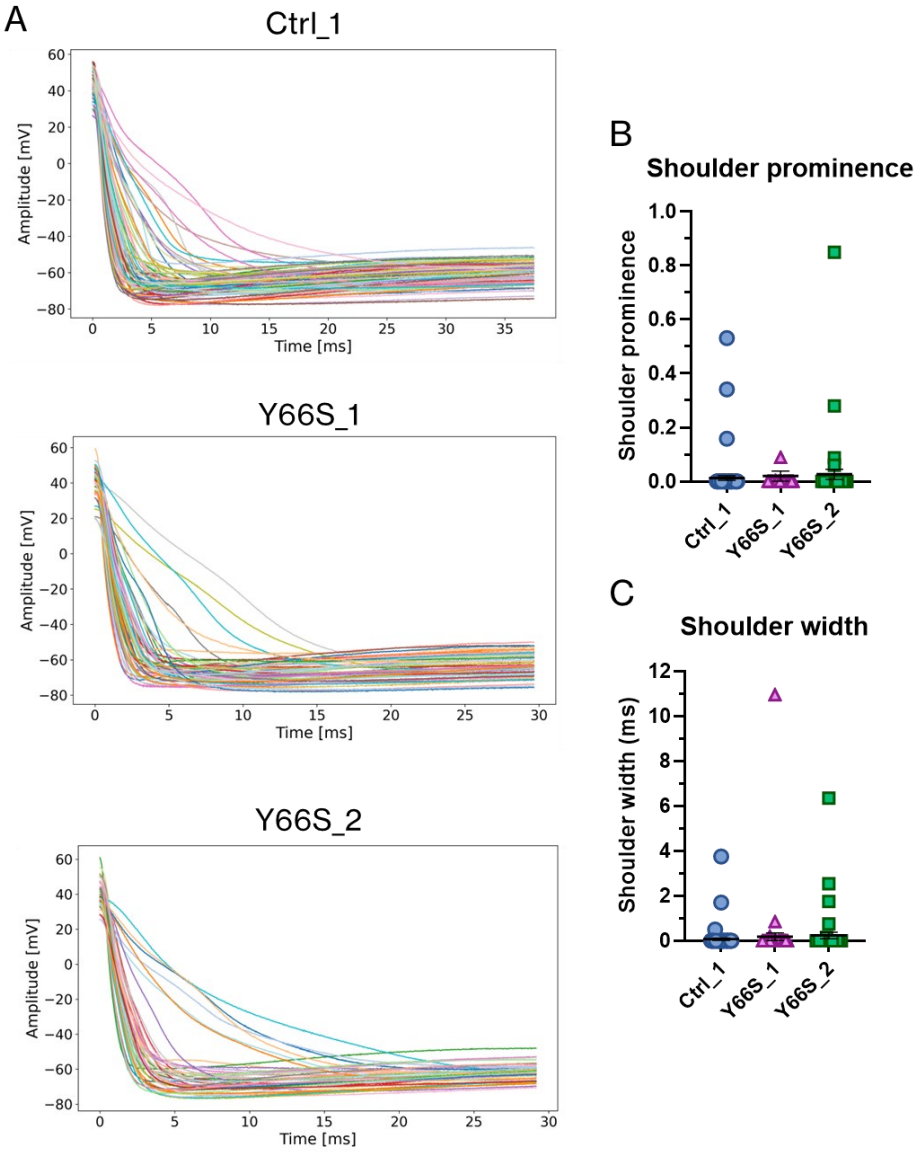

Figure 28 Action potential shoulder in control and $Na_v1.9$_Y66S iPSC-SN differentiated with the NGN1 protocol. iPSC-SN were patch clamped at DIV55-64. The first action potential fired at rheobase was used for analysis. A) Action potential traces of individual iPSC-SN (indicated in different colours) of the Ctrl_1, Y66S_1 and Y66S_2 cell lines. Traces are shown starting from the action potential maximum and show the repolarization phase, including the shoulder. B) Action potential shoulder prominence was defined as the normalized ratio between the maximum and minimum slope of the shoulder and was calculated on a scale from zero to one, where one is a change from a negative slope to a horizontal slope and a pronounced shoulder and zero is no change in slope and no action potential shoulder. C) Action potential shoulder width was

measured between the first root of the second derivative of the action potential (i.e., the first inflection of the action potential downstroke) and the largest local minimum of the first derivative after the shoulder beginning. Data is presented as mean ± SEM and was analyzed for statistically significant differences with a Mann-Whitney test. N=3; n= 48-80. *p≤0.05 **p≤0.01 ***p≤0.001 ****p≤0.0001.

Analysis of the firing frequency showed a higher number of action potentials in the Y66S_1 cell line compared to the Ctrl_1 cell line, but this difference was non-significant (Figure 29A). Interestingly, the firing frequency of the Y66S_2 patient line was lower than the one of Ctrl_1 and significantly lower than the other patient cell line. When analyzing the firing behaviour, the Y66S_1 cell line showed almost 88 % of tonically firing neurons and only 6 % of phasic and intermediate firing neurons (each) (Figure 29B). The Ctrl_1 cell line also showed a high percentage of tonically firing neurons with 74 % and 16 % intermediate, 8 % high threshold multiple and 3 % of phasically firing neurons. The Y66S_2 cell line showed the least amount of tonically firing neurons (59 %) and more intermediate (22 %) and phasic (19 %) firing neurons.
To summarize, in the NGN1-derived sensory neurons, the neuronal excitability, action potential characteristics and shape were comparable between all three cell lines, except for a lower action potential amplitude for the son patient (Y66S_2). The higher firing frequency of the mother (Y66S_1) compared to the control, as observed in the chambers-differentiated neurons, was not significant in the NGN1-differentiated neurons. Strikingly, the cell line of the son, who is suffering from SFN but does not report pain as a symptom, had the lowest firing frequency.

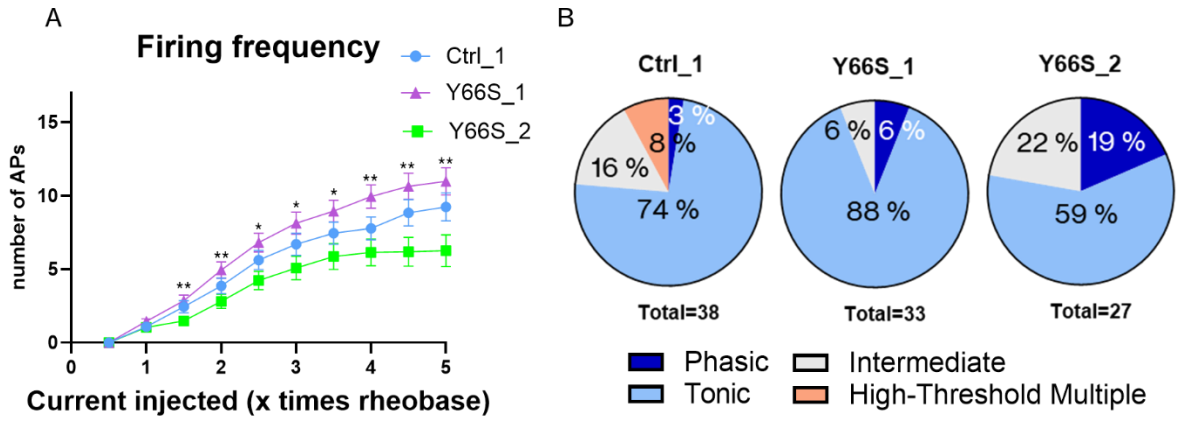

Figure 29 Firing frequency in control and $Na_v1.9$_Y66S iPSC-SN differentiated with the NGN1 protocol. iPSC-SN were patch clamped at DIV55-64. A) Firing frequency. Number of action potentials counted with increasing amounts of current injected (0.5x rheobase increments). Data is presented as mean ± SEM and was analyzed for statistically significant differences with a one-way ANOVA followed by a Tukey's multiple comparison test (if normally distributed) or a Kruskal-Wallis test followed by Dunn's multiple comparison test (if not normally distributed). Asterisks indicate statistically significant differences between the two patient cell lines. *p≤0.05 **p≤0.01 ***p≤0.001 ****p≤0.0001. N=3; n= 27-31. B) Action potential firing behaviour divided into phasic (1 action potential), tonic (>5 action potentials), intermediate (2-4 action potentials) and high-threshold multiple (1 action potential at low current injections, >5 at high current injections). N=3; n= 27-31.

5.12 Spontaneous activity was increased in $Na_v1.9$-Y66S Chambers-differentiated iPSC-SN

In neuropathic pain patients, the amount of spontaneously active fibers (i.e., firing in the absence of an input stimulus) has been found to be increased (Kleggetveit et al., 2012; Namer & Lampert, 2025). Therefore, the amount of iPSC-SN that were spontaneously active at RMP was determined to further investigate the effect of the $Na_v1.9$-Y66S variant on the firing behaviour of the cells. Cells that fired at least one action potential above 0 mV during a 20 ms period at RMP were considered spontaneously active. Most spontaneously active cells fired action potential trains (Figure 30A). In the Chambers-differentiated iPSC-SN, the patient Y66S_1 cell line showed 22 % more spontaneously active cells than the control cell line (Figure 30B). In contrast, in the NGN1-differentiated neurons, the control cell line showed 43 % spontaneously active neurons, which is 11 % more than the Y66S_1 and Y66S_2 patient cell lines (Figure 30C). These results are in line with the higher evoked firing frequency of the control cell line in NGN1 compared to Chambers (Figure 26, Figure 29).

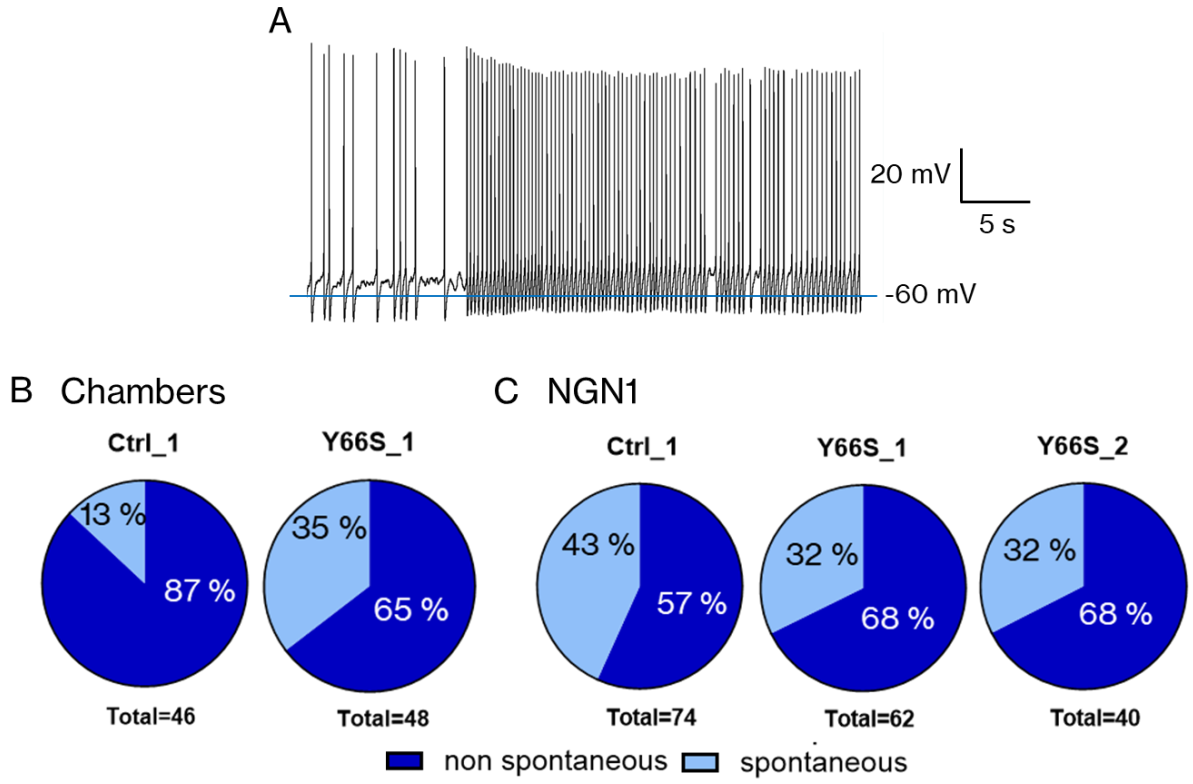

Figure 30 Spontaneous activity in iPSC-SN. iPSC-SN differentiated via the Chambers or NGN1 protocol were patch clamped at DIV55-64. Spontaneous activity was noted if at least one action potential above 0 mV was fired during a 20 ms holding period at the resting membrane potential. A) Representative trace of a spontaneously active neuron firing an action potential train. B) Quantification of spontaneous activity in Chambers-differentiated iPSC-SN and C) NGN1-differentiated iPSC-SN. N=3 n=40-74.

5.13 Potential $Na_v1.9$-Y66S-related phenotype in Chambers-differentiated iPSC-SN but not NGN1-differentiated iPSC-SN

In voltage clamp, the Chambers- or NGN1-differentiated iPSC-SN were not significantly different from each other regarding the TTXr current gating (Figure 16, Figure 17). In current clamp, the Chambers-differentiated Y66S_1 iPSC-SN were significantly different from the Ctrl_1 cell line in their firing frequency, action potential time to peak, half-width, slope upstroke and shoulder (Figure 24, Figure 25, Figure 26). These differences were not found when the same cell lines were differentiated with the NGN1 protocol (Figure 27, Figure 28, Figure 29). To understand why a $Na_v1.9$-Y66S phenotype was observed in Chambers-differentiated neurons but not NGN1-differentiated neurons, the neuronal excitability parameters between the identical cell lines differentiated with the two protocols were compared. The analysis revealed that the Chambers-differentiated iPSC-SN had a significantly more depolarized RMP and a significantly smaller rheobase compared to the NGN1-differentiated cells (Table 18). Furthermore, the voltage threshold was significantly more hyperpolarized in the Chambers-differentiated neurons. These results hint that the Chambers-differentiated iPSC-SN could be firing upon smaller input stimuli compared to the NGN1-differentiated neurons. Interestingly, the action potential half-width, time to peak, afterhyperpolarization, shoulder prominence, shoulder width and cell capacitance were significantly different between the control cell lines differentiated with the two protocols but not the patient cell lines. In addition, the firing frequency was statistically different between the Ctrl_1 lines from a rheobase injection between 1.5x – 5 x, but not between the Y66S_1 cell line differentiated with the two protocols (data presented in Figure 26 and Figure 29 and analyzed by one-way ANOVA & Tukey's multiple comparison test if normally distributed or a Kruskal-Wallis &Dunn's multiple comparison test if not normally distributed). This indicates that the difference in phenotypic modelling between the two differentiation protocols may originate from the Ctrl_1 cell line developing differently in the two differentiation protocols. The Ctrl_1 iPSC-SN differentiated with the NGN1 protocol seem to be more active and more similar to the Y66S_1 iPSC-SN in their action potential parameters, while the Chambers-differentiated Ctrl_1 iPSC-SN show more differences from the patient iPSC-SN.

5.14 Neuronal excitability and action potential characteristics in NGN1-differentiated iPSC-SN with cAMP

Supplementation of neuronal media with cyclic adenosine monophosphate (cAMP) has been found to promote neuronal differentiation (Lepski et al., 2013). Therefore, in an attempt to increase iPSC-SN maturation, observe larger $Na_v1.9$ currents and a phenotypic difference between the $Na_v1.9$-Y66S patient and control cell line, iPSC-SN differentiated via the NGN1 protocol were cultured with 0.5 mM cAMP in the maturation media. Addition of cAMP to the media did not alter the RMP (Ctrl_1 -70.7 ± 0.8, Ctrl_1 cAMP -69.3 ± 1.9, Y66S_1 -70.2 ± 1.2, Y66S_1 cAMP -66 ± 2.3 mV), rheobase (Ctrl_1 83.5 ± 6.8, Ctrl_1 cAMP 96 ± 8.3, Y66S_1 66 ± 5.4, Y66S_1 cAMP 99 ± 11.5 pA) or voltage threshold (Ctrl_1 -55.5 ± 0.5, Ctrl_1 cAMP -52.6 ± 1.2, Y66S_1 -55.6 ± 0.6, Y66S_1 -53.6 ± 1.2 mV), but significantly increased the action potential amplitude (Ctrl_1 107.8 ± 0.8, Ctrl_1 cAMP 102.2 ± 1, Y66S_1 105.9 ± 1, Y66S_1 cAMP 98 ± 1.7 mV) and half-width (Ctrl_1 1.9 ± 0.1, Ctrl_1 cAMP 2.4 ± 0.1, Y66S_1 2.1 ± 0.2, Y66S_1 cAMP 2.3 ± 0.1 ms) compared to the culture without cAMP (Figure 31B,C,D,E,F, Table). The action potential slope upstroke (Ctrl_1 9.9 ± 0.8, Ctrl_1 cAMP 12.6 ± 1, Y66S_1 8.6 ± 0.7, Y66S_1 cAMP 13 ± 1.2) and time to peak (Ctrl_1 35.6

± 4.3, Ctrl_1 cAMP 28.9 ± 8, Y66S_1 38.7 ±3.2, Y66S_1 cAMP 23.2 ±5.3 ms) were significantly different between culture with and without cAMP for the patient cell line, while the afterhyperpolarization (Ctrl_1 -69.8 ± 0.6, Ctrl_1 cAMP -66.3 ± 1, Y66S_1 -69.8 ± 0.6, Y66S_1 cAMP -69 ± 0.9 mV) was significantly different between the control cell line cultures (Figure 31G,H,I). The input resistance was significantly lower for the Y66S_1 cAMP cell line compared to the Y66S_1 cell line, while the cell capacitance was unchanged between all cell lines (Figure 31 J,K).
The addition of cAMP to the maturation media changed these parameters within the cell lines, but no phenotypic difference between the patient and the control cell line could be observed within the iPSC-SN cultured with cAMP. In line with this, the iPSC-SN cultured with cAMP did not show $Na_v1.9$-like persistent current (Figure 31M,N). Interestingly, the culture of NGN1-differentiated iPSC-SN with cAMP resulted in a 13 % decrease in spontaneous activity in the control cell line, while making the patient cell line 4 % more spontaneously active (Figure 31L, Figure 29).

Table 18 Neuronal excitability and action potential characteristics of iPSC-SN differentiated via the Chambers or NGN1 protocol. iPSC-SN were patch clamped at DIV55-64. The first action potential fired at rheobase was used for analysis. Action potential shoulder prominence was defined as the change in slope during the repolarization phase and was calculated on a scale from zero to one, where one is a change from a negative slope to a horizontal slope and a pronounced shoulder and zero is no change in slope and no action potential shoulder. Action potential shoulder width was measured between the first root of the second derivative of the action potential (i.e., the first infliction of the action potential downstroke) and the largest local minimum of the first derivative after the shoulder beginning. Data is presented as mean ± SEM. Statistically significant differences between the same cell line differentiated via the Chambers or NGN1 protocol was analyzed with a Kruskal-Wallis test followed by Dunn's multiple comparison test. *p≤0.05 **p≤0.01 ***p≤0.001 ****p≤0.0001. N=3.

Parameter	Ctrl_1		Y66S_1	
	Chambers	NGN1	Chambers	NGN1
RMP (mV)	-65.9 ± 0.9****	-70.7 ± 0.8****	-64.6 ± 1.3****	-70.2 ± 1.2****
Rheobase (pA)	46.9 ± 4.7***	83.5 ± 6.8***	36.4 ± 4.4***	66.1 ± 5.4***
Amplitude (mV)	106.8 ± 1	107.8 ± 0.8	105.6 ± 1.5	105.9 ± 1
Voltage threshold (mV)	-57.9 ± 0.5*	-55.5 ± 0.5*	-58.4 ± 0.6**	-55.6 ± 0.6**
Half-width (ms)	2.7 ± 0.2****	1.9 ± 0.1****	2.1 ± 0.1	2.2 ± 0.2
Time to peak (ms)	21.7 ± 1.8**	35.6 ± 4.3**	31.9 ± 2.3	38.7 ± 3.2
Slope upstroke (V/s)	11.7 ± 0.9	9.9 ± 0.8	8.1 ± 0.9	8.6 ± 0.7
Afterhyperpolarization (mV)	-71.9 ± 0.6*	-69.8 ± 0.6*	-71.7 ± 0.6	-69.8 ± 0.6
Shoulder prominence	0.2 ± 0.1****	0.01 ± 0.008****	0.05 ± 0.03	0.02 ± 0.02
Shoulder width (ms)	1.9 ± 0.6****	0.07 ± 0.05****	0.24 ± 0.2	0.2 ± 0.2
Input resistance (MΩ)	231.4 ± 14.6**	183.3 ± 17.5**	223.1 ± 14.1	201.4 ± 14.8
Capacitance (pF)	34.2 ± 2.6***	51.1 ± 2.5***	44.4 ± 3.6	44.2 ± 2.8
n	44	59	39	59

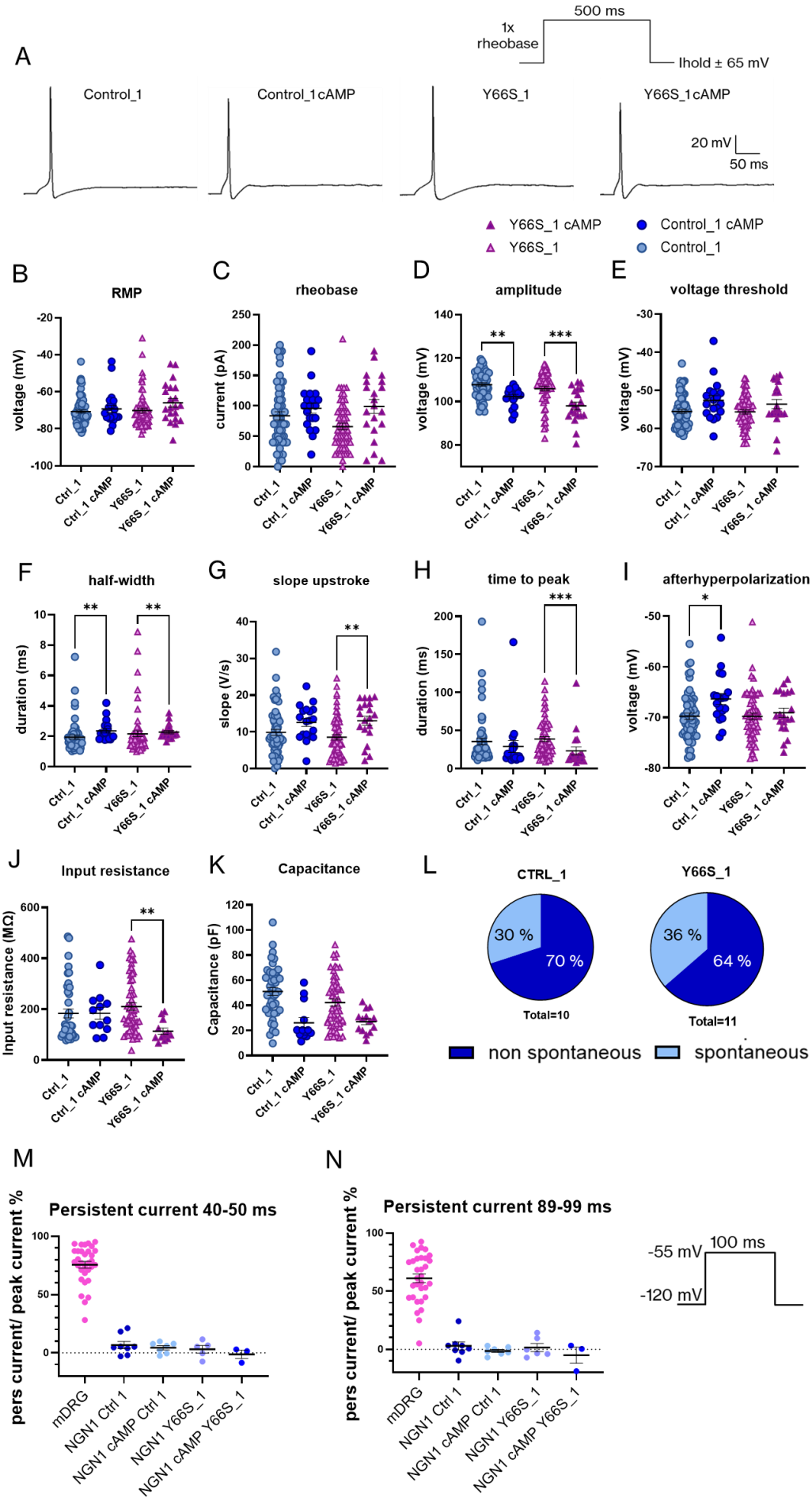
A
500 ms
1x rheobase
Ihold ± 65 mV
Control_1
Control_1 cAMP
Y66S_1
Y66S_1 cAMP
20 mV
50 ms
Y66S_1 cAMP
Y66S_1
Control_1 cAMP
Control_1
B
RMP
voltage (mV)
C
rheobase
current (pA)
D
amplitude
voltage (mV)
E
voltage threshold
voltage (mV)
Ctrl_1
Ctrl_1 cAMP
Y66S_1
Y66S_1 cAMP
F
half-width
duration (ms)
G
slope upstroke
slope (V/s)
H
time to peak
duration (ms)
I
afterhyperpolarization
voltage (mV)
J
Input resistance
Input resistance (MΩ)
K
Capacitance
Capacitance (pF)
L
CTRL_1
Y66S_1
30 %
70 %
36 %
64 %
Total=10
Total=11
non spontaneous
spontaneous
M
Persistent current 40-50 ms
pers current/ peak current %
mDRG
NGN1 Ctrl 1
NGN1 cAMP Ctrl 1
NGN1 Y66S_1
NGN1 cAMP Y66S_1
N
Persistent current 89-99 ms
pers current/ peak current %
-55 mV
100 ms
-120 mV

Figure 31 Effect of cAMP on neuronal excitability and action potential characteristics of control and $Na_v1.9$_Y66S iPSC-SN differentiated with the NGN1 protocol. The NGN1 protocol maturation media was supplemented with 0.5 mM cAMP. iPSC-SN were patch clamped at DIV55-64. The first action potential fired at rheobase was used for analysis. A) Representative action potential traces of Ctrl_1 and Y66S_1 differentiated with or without cAMP. B) Resting membrane potential (RMP). C) Rheobase. D) Action potential amplitude. E) Action potential voltage threshold. F) Action potential half-width. G) Action potential slope upstroke. H) Action potential time to peak. I) Action potential afterhyperpolarization. J,K) Input resistance was determined by calculating the voltage change upon administration of two hyperpolarized current injections with a delta of 50 pA. K) Cell capacitance was measured by the patch clamp amplifier (C-slow). L) Quantification of spontaneously active neurons in iPSC-SN differentiated with cAMP. Spontaneous activity was noted if at least one action potential above 0 mV was fired during 20 ms holding period at the resting membrane potential. M,N) Quantification of persistent current in mDRG and iPSC-SN normalized to the peak current at -55 mV between 40-50 ms and 89-99 ms after test pulse start. Data is presented as mean ± SEM. Data from B-K was analyzed for statistically significant differences with a Kruskal-Wallis test followed by Dunn's multiple comparison test. N=3, n=19-59. *p≤0.05 **p≤0.01 ***p≤0.001 ****p≤0.0001. cAMP= cyclic adenosine monophosphate

5.15 $hNa_v1.9$ could not be expressed in SH-SY5Y cells or iPSC-SN

In iPSC-SN, no clear $Na_v1.9$-like current could be observed. Therefore, alternative strategies to model $Na_v1.9$ variants were explored by transfecting $Na_v1.9$ into SH-SY5Y cells and iPSC-SN. The heterologous expression of $Na_v1.9$ enables the study of channel kinetics in isolation. Furthermore, such systems serve as a platform for testing potential Na_v blockers, which can then be used to isolate specific Na_v currents in systems expressing multiple TTXr Na_v channels, such as mDRG neurons or iPSC-SN. The expression of $hNa_v1.9$ in heterologous systems has been published (Vanoye et al., 2013; Zhou et al., 2017). In the study of Zhou et al., however, the efficiency of $Na_v1.9$ expression remained low, and the results have proven difficult to reproduce across different research groups. To address this, we utilized an eGFP-fused $Na_v1.9$ plasmid that had been codon-optimized for translation by human ribosomes. SH-SY5Y cells were chosen as the host cell line for transfection due to their human neuroblastoma origin. This decision was made in contrast to the frequently used ND7/23 cell line, which is derived from rat dorsal root ganglia. Additionally, SH-SY5Y cells exhibit minimal endogenous TTX-resistant (TTXr) currents, and no detectable $Na_v1.9$ mRNA levels or $Na_v1.9$ currents have been reported in this cell line (Vetter et al., 2012).

The success of sodium channel transfections is dependent on the ideal amount of plasmid and the transfecting reagent JetPei. Adequate amounts of plasmid DNA must be available for cellular uptake, while excessive concentrations of either DNA or JetPei are cytotoxic. To determine the ideal conditions for the transfection of the $Na_v1.9$ plasmid into SH-SY5Y cells, three different DNA concentrations (0.75, 1.5, 2.25 µg) and three different JetPei concentrations (1.5, 2.25, 3 µL) were tested and analyzed 24 and 48 h post-transfection. Cells transfected with 0.5 µg tGFP served as a positive control and cell density was kept comparable. pmaxGFP expression was detected in all three tested JetPei conditions after 24 h and the signal increased after 48 h (Figure 32A). However, no cells transfected with the $Na_v1.9$ plasmid exhibited a strong fluorescent signal.

To enhance the $Na_v1.9$ transfection efficiency, the amount of JetPei was increased to 4.5 µL and 1.5 µg $Na_v1.9$ DNA was used, as no difference was observed between 1.5 µg and 2.25 µg DNA, and lower DNA amounts improved cell viability. The pmaxGFP concentration was reduced to 0.25

µg. Under these conditions, the transfected SH-SY5Y cells showed positive fluorescent signal for pmaxGFP, but the $Na_v1.9$_GFP-transfected cells showed very weak to no fluorescent signal (Figure 32B). Given that weak fluorescence may still indicate protein presence, cells were further analyzed for TTXr currents in voltage clamp. However, the maximum recorded current of -66.1 ± 13.3 pA at -30 mV falls within the noise range of leak currents, suggesting an absence of TTXr Na_v currents. Previous studies have reported that maintaining transfected cells at 28°C can enhance $Na_v1.9$ expression efficiency and increase current amplitudes (Vanoye et al., 2013; Zhou et al., 2017). Therefore, transfected cells were cultivated at 28°C for 48 h post-transfection. However, this approach led to a reduction in fluorescence intensity for both the pmaxGFP positive control and the $Na_v1.9$-transfected cells (Figure 32C). Furthermore, no TTXr currents were detected in the $Na_v1.9$-transfected cells under these conditions.

Heterologous expression systems may lack the translational and post-translational machinery to express $Na_v1.9$. Therefore, I attempted to transfect $Na_v1.9$ into iPSC-SN to obtain differentiated sensory neurons with $Na_v1.9$ in addition to the endogenous TTXr currents and the action potential properties of iPSC-SN that were described in the previous sections. Transfection was performed in 8-week-old Ctrl_1 NGN1-differentiation neurons with a GFP-tagged WT $Na_v1.9$ plasmid, which has previously been successfully used in mDRG neurons (van den Braak et al., 2025). Neurons were patch clamped 72 h post-transfection. Few neurons appeared to be labelled bright fluorescently green, but showed no TTXr currents (Figure 33A). It was hypothesized that the very bright signal might only appear in neurons with damaged cellular membranes that were easy to enter for the plasmid, but were too apoptotic to show current. Therefore, neurons showing a light fluorescent signal were measured. These neurons showed very small transient TTXr currents, but no $Na_v1.9$-like persistent current (Figure 33B). Finally, transfected cells that did not show fluorescent signal and untransfected cells were patch clamped as controls. The transfected iPSC-SN that did not show fluorescent signal showed more transient TTXr current than the neurons with positive signal (Figure 33C), but the untransfected iPSC-SN showed the most TTXr current. These results indicate that the transfection with the $Na_v1.9$ plasmid was unsuccessful and did not result in $Na_v1.9$-like persistent current. The different conditions also show that the transfection itself may be harmful to the neurons and could decrease the current amplitude. Furthermore, it appears that the plasmid could only successfully enter and/or be translated in cells that did not have big TTXr current and might be apoptotic.

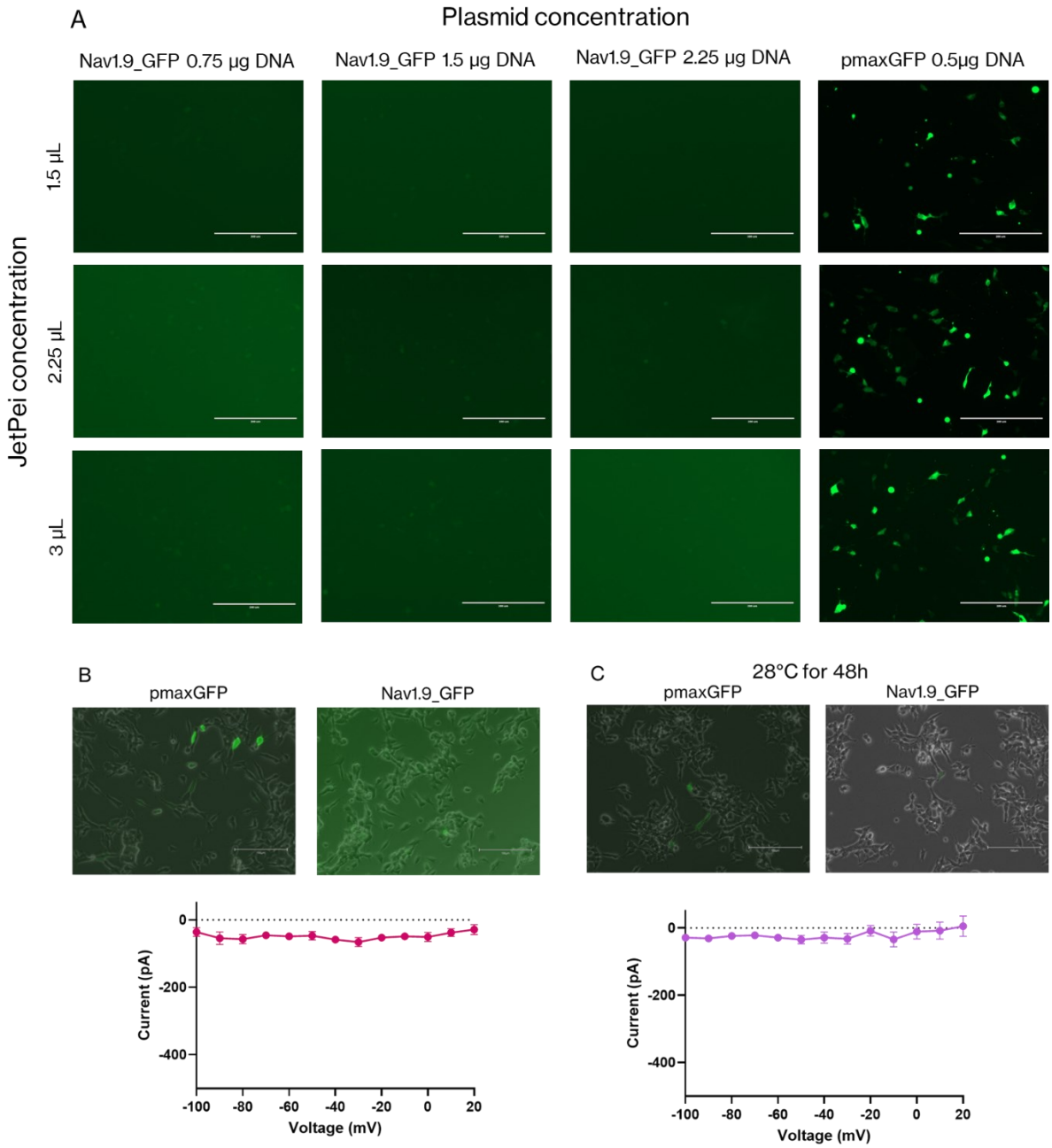

Figure 32 $Na_v1.9$ transfection in SH-SY5Y cells. A) SH-SY5Y cells transfected with 0.75, 1.5 or 2.25 µg of $Na_v1.9$_GFP or 0.5 µg of pmaxGFP and 1.5, 2.25 or 3 µL JetPei. Images were taken 48h post-transfection. Scale bar 200 µm. B,C) Images and current/ voltage (IV) curve of the mean inward current of SH-SY5Y cells transfected with $Na_v1.9$_GFP at 37°C (B) or 28°C (C), n= 6, scale bar 150 µm. GFP= green fluorescent protein.

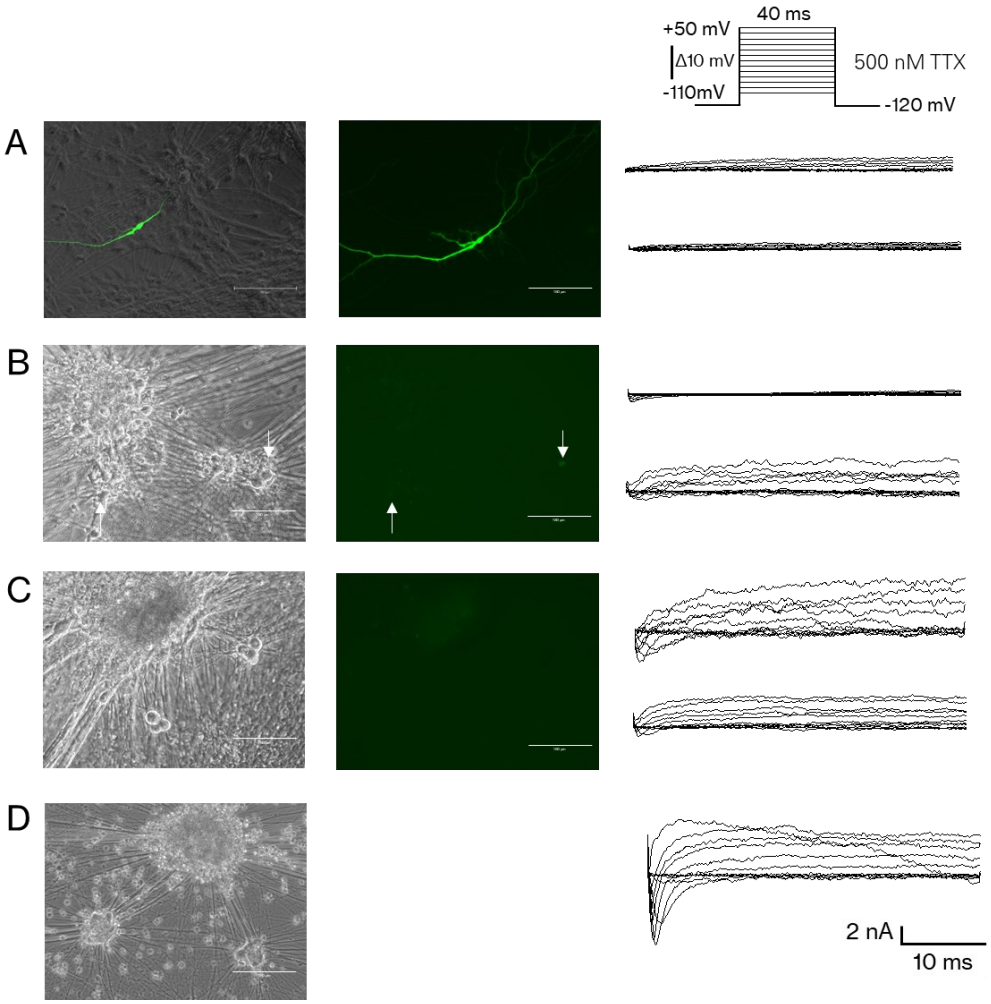

Figure 33 Transfection of iPSC-SN with $Na_v1.9$_GFP. iPSC-SN were mature for 8 weeks before transfection and patch clamped 72 h post-transfection. Brightfield and overlay images with representative current traces for A) iPSC-SN displaying bright green signal B) iPSC-SN displaying faint green signal (indicated with white arrow) C) iPSC-SN displaying no positive signal and D) untransfected iPSC-neurons. Scale bar 150 µm. GFP= green fluorescent protein.

5.16 Modelling keratinocytes under mechanical stress

The aim of this thesis was to develop *in vitro* models for neuropathic pain. The development of a neuropathic pain patient-derived iPSC-SN model has already been discussed. The next part of the thesis will describe the development of an *in vitro* model for neuropathic focused on surrounding cell types and factors that can sensitize sensory nerves, with particular emphasis on keratinocytes under mechanical compression.

Patients diagnosed with Pachyonychia congenita (PC) suffer from thick callus on the glabrous skin of their hands and feet, causing severe pain. It is likely that the presence of the thick callus causes an increase in mechanical compression on all layers of the skin compared to healthy individuals, resulting in an altered local mechanosensation. Additionally, the keratin mutations in the keratinocytes of PC patients likely lead to an altered mechanotransduction (Shutova & Boehncke, 2022). Simultaneously, PC patients frequently report neuropathic pain as their primary symptom and show a reduced intraepidermal nerve fiber density (IEFND) (Pan et al., 2016). As explained in depth in the introduction, keratinocytes can modulate nociception (see section 1.10) (Talagas,

Lebonvallet, Berthod, et al., 2020). Therefore, it was hypothesized that the altered mechanical stress that the keratinocytes on the hands and feet of PC patients are experiencing in combination with the altered mechanotransduction could lead to an altered secretome and signaling of keratinocytes. This could sensitize the free nerve endings in the skin, resulting in neuropathic pain. To investigate this hypothesis, first a keratinocyte and mDRG co-culture was developed. Second, to investigate the role of the keratinocytes, it was essential to only mechanically compress the keratinocytes and not the nerve somata. Therefore, a dynamic cyclic compression system to mechanically compress a monolayer of keratinocytes was developed to model mechanical compression as occurring on the feet while walking. It was then analyzed whether the compressed keratinocytes of healthy and PC patients showed mRNA upregulation of neuroactive factors following compression and whether the factors they secrete are sufficient to increase the excitability of mDRG. This project was performed in collaboration with Mert Karpat (Department of Dental Materials and Biomaterials Research, Uniklinik RWTH Aachen, Germany) and Kyeongmin Kim (Institute of Molecular and Cellular Anatomy, Uniklinik RWTH Aachen, Germany).

5.17 HaCaT and mDRG neurons form connections in co-culture

The objective of the co-culture experiments was to determine whether HaCaT keratinocytes and mDRG neurons could be cultured in a manner that spatially separates neuronal cell bodies while allowing mDRG neurites to extend into the keratinocyte layer. This arrangement would enable mechanical stimulation of keratinocytes and neurites exclusively, modelling the way that mechanical stimulation is detected in the skin. Two days (DIV2) after the HaCaTs and mDRG neurons were seeded on separate ends of the coverslip, the bulk of HaCaTs and mDRG neurons were still spatially separate from each other, with a narrow region of mixed cells in the middle (Figure 34A). Due to the rapid proliferation of keratinocytes and the post-mitotic nature of neurons, the keratinocytes progressively expanded, advancing towards and eventually surrounding the mDRG neurons by DIV5 (Figure 34B). At this stage, short neurite extensions from neurons towards neighboring keratinocytes became visible.

These findings demonstrate that keratinocytes and mDRG neurons can be co-cultured and establish physical connections. However, in the setup used here, mechanical stimulation would affect both keratinocytes and neuronal somas, making it unsuitable for investigating the role of keratinocytes in mechanically induced sensory nerve sensitization. Therefore, a system was developed to cyclically compress keratinocytes exclusively. Additionally, the HaCaT cell line was replaced with human keratinocytes immortalized with HPV 6/7, allowing for the use of patient-derived and control cell lines that were immortalized under standardized conditions.

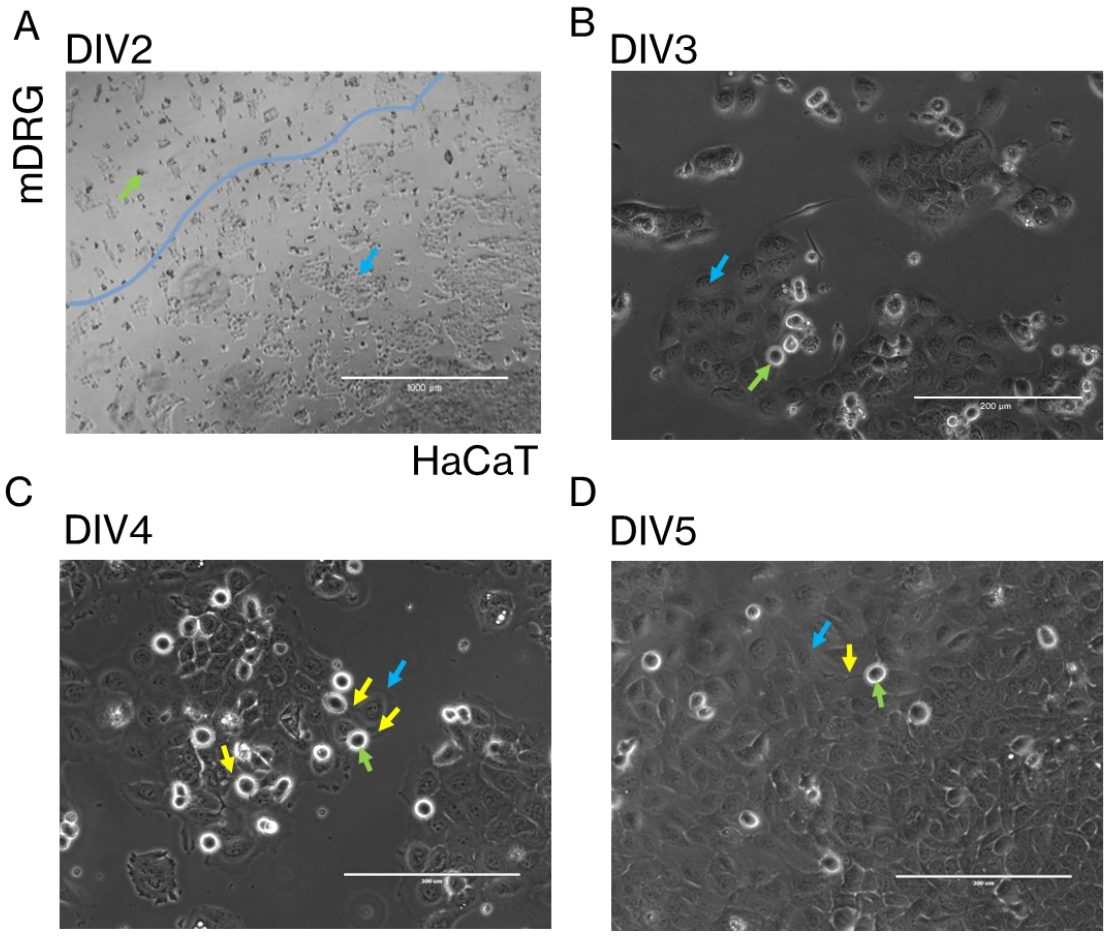

Figure 34 HaCaT keratinocytes and mDRG neurons co-culture. A) Co-culture at DIV2 with mDRG neurons seeded into the top left corner and HaCaTs seeded into the bottom right corner. The blue line indicates the border between the cell areas. Scale bar 1000 µM. B-D) HaCaT and mDRG neuron co-culture at DIV3-DIV5. The blue arrows indicate keratinocytes, the green arrows indicate mDRG neurons and the yellow arrows indicate neurite extensions from mDRG neurons towards keratinocytes. Scale bar 200 µm. DIV: days *in vitro*.

5.18 Design of a keratinocyte monolayer cyclic compression system

To simulate physiological mechanical stress occurring during e.g. walking or other everyday-life mechanical exposures, we aimed to cyclically compress keratinocyte monolayers and thus developed a dynamic cyclic compression system alongside a specialized keratinocyte seeding technique. The system allows for adjustments in both compression frequency and applied pressure by modifying the motor speed and adding weight to the stamp's basket. The pressures exerted during compression were calculated based on the total mass of the stamp and the restricted cell growth area. The total mass includes the intrinsic mass of the stamp as well as any additional stainless-steel weights placed in the basket. These calculations were performed by Mert Karpat (Department of Dental Materials and Biomaterials Research, Uniklinik RWTH Aachen, Germany). A stamp without additional weight in the basket had a mass of 7 g, generating a compressive pressure of 0.45 kPa on the cells. Adding 7 g of weight increased the applied pressure to 0.9 kPa.

For keratinocyte compression, cells were seeded into 35 mm glass-bottom dishes to allow for high-quality microscopy following compression. These dishes have a minor step between the 20 mm wide glass bottom and the plastic bottom of the dish. This structure increases the shear stress that the cells are experiencing when the compression stamp moves up and down in the media. To mitigate this issue, the total compression area was positioned at a defined distance from the interface between the glass bottom and the plastic dish to facilitate the smooth outflow of medium from the monolayer's surface during compression, thereby minimizing resistance. In addition, the designated cell area was designed to be smaller than the area of the stamp to ensure uniform compression of all keratinocytes within the monolayer. Based on these considerations, keratinocytes were seeded in a defined 14 mm area, and 3 mL of medium was added during compression to keep the stamp fully submerged and to reduce wave formation in the medium.

To model the compressive forces that the soles of the feet of healthy and PC patients are experiencing, ideally, a compression frequency modelling the walking frequency of humans (~2 Hz) would be applied. However, while walking *in vivo*, the mechanical load is spread over the entire foot and the full thickness of the skin and underlying tissue. In our experimental setup *in vitro,* the mechanical load is concentrated onto a monolayer of keratinocytes. Therefore, Mert Karpat (Department of Dental Materials and Biomaterials Research, Uniklinik RWTH Aachen, Germany) modelled *in silico* how different compression frequencies affected the amount of shear stress on the keratinocytes. The results showed that increasing the compression frequency increased the shear stress on the cells (unpublished data of Mert Karpat). As our model was aiming to investigate the effect of mechanical compression alone, we aimed to minimize the shear stress as a confounding variable. Therefore, a compression frequency of 150 mHz was chosen.

Ideally, the dynamic cyclic compression would result in a cellular response of the keratinocytes (i.e. increase in cytokine secretion) without inducing cell death. If the compressive weight is too high, the release of neuroactive factors that will be investigated here would simply stem from apoptotic processes in the cells. Therefore, Kyeongmin Kim (Institute of Molecular and Cellular Anatomy, Uniklinik RWTH Aachen, Germany) performed cyclic compression for 1 h at 150 mHz with different compression weights and examined the apoptosis levels with a Caspase 3/7 staining. The results showed that at 0.9 kPa compressive force, up to 5 % of WT cells were positive for caspase 3/7 staining and 5-10 % of PCK16 cells, which was comparable to the apoptosis levels in uncompressed cells (unpublished data of Kyeongmin Kim). Increasing the compressive weight for a higher compressive force resulted in cellular death and the detachment of cells and therefore, 0.9 kPa compressive force for 1 h at 150 mHz were selected as the compression parameters.

5.19 Cytokine gene expression is increased in PC keratinocytes compared to WT keratinocytes

To determine the level of gene expression of cytokines and neuroactive factors in keratinocytes from healthy donors and donors with PC, qPCR was performed. IL-1α and IL-1β were significantly higher expressed in the PCK6 cell line compared to the WT (IL-1α 2-fold; IL-1β 4-fold) (Figure 35A,B). The IL-1 isoforms were also increased by 2-fold in the PCK16 cell line compared to the WT, albeit non-significantly. TNF-α mRNA levels were upregulated in the PC cell lines compared to the WT by 15-fold (PCK6: 15.7 ± 11.25; PCK16: 15 ±7.2, $p<0.05$, Figure 35C). IL-6 and IL-8 were 2- to 4-fold higher in the PC cell lines compared to the WT (non-significant) (Figure 35D,E). NGF mRNA levels were non-significantly increased in PCK16 cells compared to WT cells (1.8 ± 0.4, Figure

35F). The here tested cytokines were only partially statistically significantly upregulated in the PC keratinocytes compared to the control, but overall, a trend is visible of higher cytokine mRNA expression in the PC cell lines, indicating a pro-inflammatory phenotype in PC cells.

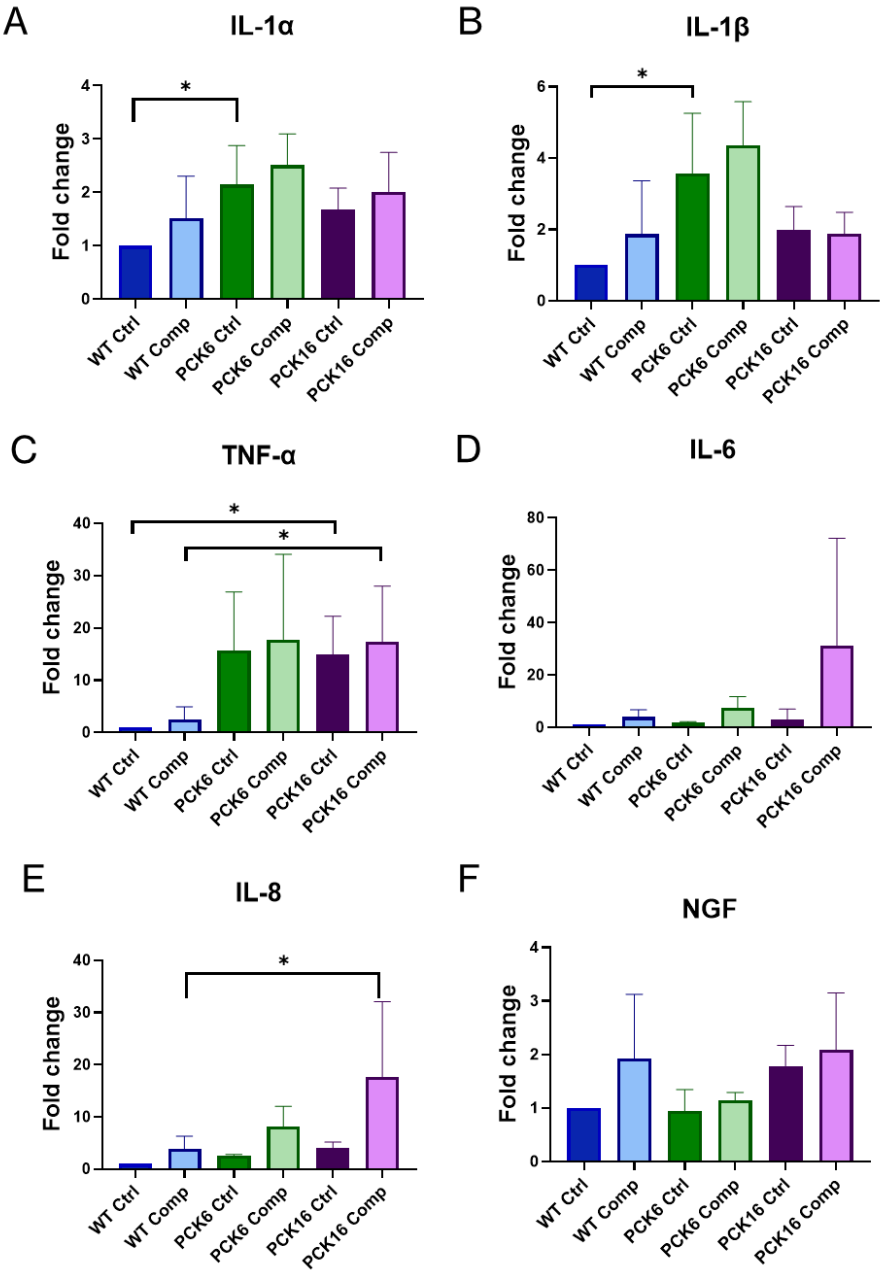

Figure 35 Cytokine gene expression in compressed or uncompressed WT, PKC6 and PCK16 keratinocytes. Dynamic cyclic compression was performed for 1 h at 150 mHz with 0.9 kPa compressive force. Cells were lysed 2 h after compression. Data is presented as mean ± SD fold change in gene expression from the WT Ctrl and was analyzed for statistically significant differences with the Kruskal-Wallis test, followed by Dunn's multiple comparison test. *p≤0.05 **p≤0.01 ***p≤0.001 ****p≤0.0001.N=4; WT Ctrl n=6, WT comp n=8, PCK6 Ctrl n=5, PCK6 comp n=4, PCK16 Ctrl n=6, PCK16 comp n= 7. WT= wild type, IL= Interleukin, TNF-α = Tumor-necrosis-factor alpha, NGF= nerve growth factor. Ctrl= Control, uncompressed; Comp= Compressed

5.20 Cyclic compression increased cytokine expression more strongly in PC keratinocytes compared to WT keratinocytes

Cyclic compression for 1 h at 150 mHz frequency and 0.9 kPa compressive force increased the mRNA levels of IL-1α, IL-1β, IL-6 and IL-8 in both WT and PC cell lines, except for IL-1β in PCK16 (Figure 35A,B,D,E). However, most of these changes were not statistically significant and can therefore only be interpreted as an observed trend. While IL-1α and IL-1β gene expression was increased in a comparable amount between WT and PC cell lines following compression, IL-6 and IL-8 were more highly upregulated in PC cell lines. This was especially remarkable for the PCK16 cells, in which IL-6 was 10-fold and IL-8 was 4-fold increased after compression compared to the uncompressed PCK16 cells (Figure 35D,E). Furthermore, IL-6 was 8-fold and IL-8 was 4-fold higher expressed in PCK16 compressed cells compared to WT compressed cells (Figure 35D,E). This large fold increase was only statistically significant for IL-8 in PCK16 keratinocytes, likely due to the high variance between compressed PC cell samples, which often occurs following biological interventions. TNF-α was significantly increased in PCK16 compressed cells compared to WT compressed cells. However, this is likely related to the increased TNF-α levels in PCK16 cells before compression (Figure 35C). NGF mRNA levels were non-significantly increased in the WT following compression (1.9 ± 1.2 fold), but did not increase much upon compression of PC cell lines (Figure 35F).

To summarize, it was observable that IL-1α, IL-1β and TNF-α are higher expressed in general in PC cell lines, while IL-6 and IL-8 gene expression was more upregulated in PC cell lines compared to WT cell lines following cyclic compression. Interestingly, the PCK6 cell lines had higher levels of IL-1α and IL-1β before compression, whereas the PCK16 cells were more responsive to cyclic compression in terms of IL-6 and IL-8 upregulation.

5.21 Stimulation with supernatant of compressed keratinocytes did not result in altered mDRG firing behaviour

To investigate if the upregulation of mRNA of IL-1, IL-6, IL-8 and TNF-α resulted in an increased cytokine production and secretion sufficient to sensitize sensory neurons, the supernatant of compressed and uncompressed WT and PCK16 keratinocytes was applied to mDRG neurons. The supernatant of three different compression runs was combined to increase the biological sample size and then concentrated in centrifugal concentrator tubes to decrease the initial high volume of the supernatant. A pore size of 3 kDa was chosen for the concentrator tubes, as the smallest relevant protein was IL-8 with a size of approximately 8 kDa (Möller et al., 1993). The sample WT Ctrl (uncompressed) served as the control condition here, as these cells were not exposed to compression and do not carry a keratin mutation.

During the concentration in the concentrator tubes, it became evident that the supernatant of the different conditions could be concentrated to varying degrees. The supernatant of the WT uncompressed cell line could be concentrated to the smallest volume (270µL), followed by the PCK16 uncompressed condition (400µL) and the compressed conditions (WT 460µL, PCK16 720µL). All samples should contain similar amounts of media components, such as serum, that could increase the dead volume left in the membrane. Therefore, the differences in the concentrated supernatant volume could indicate a higher protein concentration in the supernatant of the compressed samples. The supernatant was then rediluted to the same total volume.

mDRG neurons were patch clamped between 12-48 h after supernatant incubation. The four conditions were patch clamped in alternating order to maintain comparable incubation times between all conditions. The duration of incubation had an observable effect on the neuronal activity of the mDRG neurons within one condition. The mDRG neurons could be cultured for up to 48 h in the supernatant of the keratinocytes diluted in DMEM media. A decrease in cell count was visible after 12 h of incubation, but a decrease in cell number between the mDRG isolation day and the following day is frequently observed, as not all cells can firmly attach to the coverslip (Figure 36). After an additional 24 h of incubation, the cell number decreased further, likely due to the prolonged exposure to media that presumably contained cytokines, causing cellular stress. Interestingly, the mDRG neurons cultured with PCK16 Ctrl media seemed to exhibit the most cellular stress, as visible by the granularity of the cells. However, this was not quantified with an apoptosis staining.

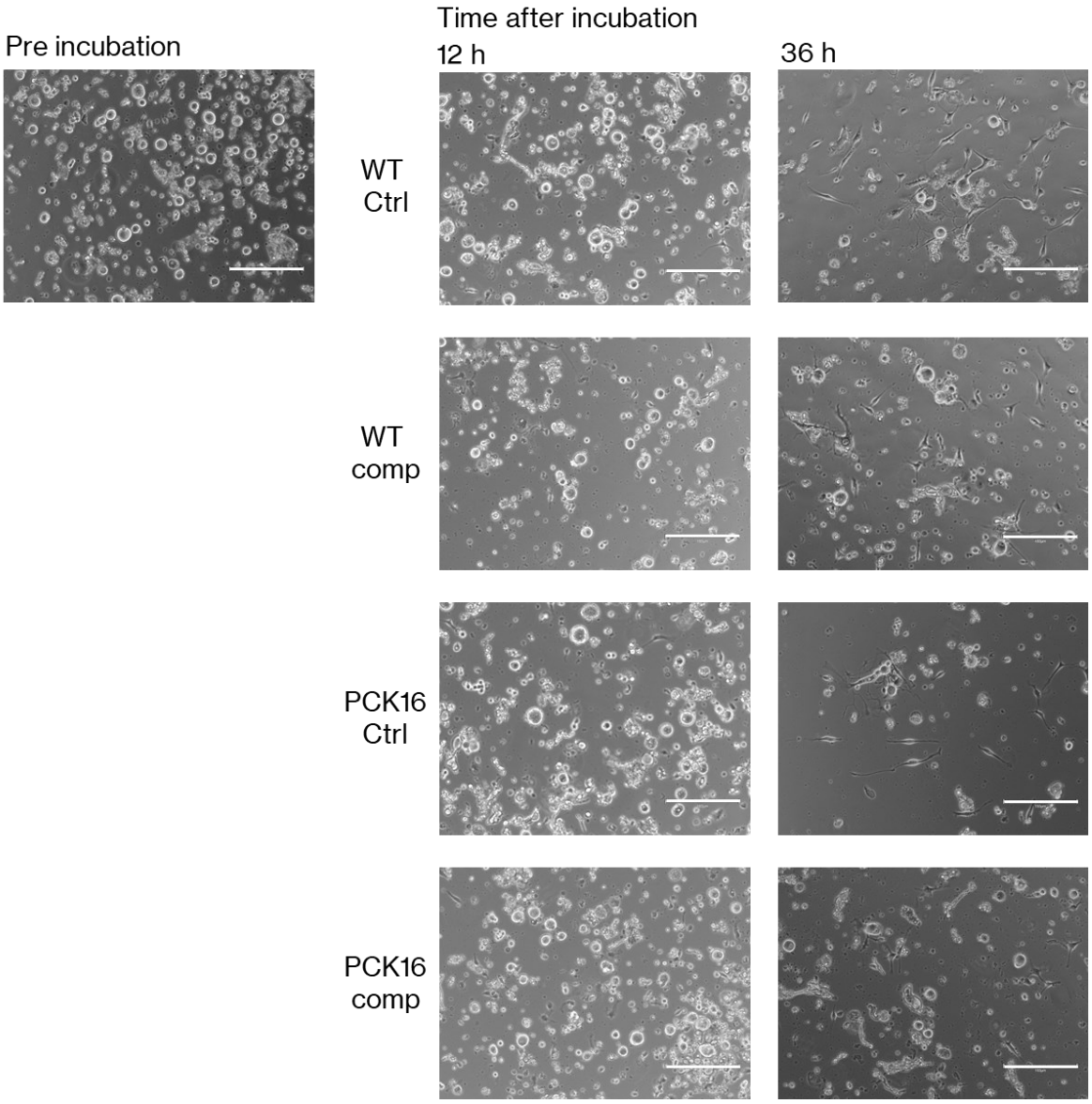

Figure 36 mDRG neurons pre- and post-incubation with supernatant from uncompressed or compressed keratinocytes. Dynamic cyclic compression was performed for 1 h at 150 mHz with

0.9 kPa compressive force on WT and PCK16 keratinocytes. Media of compressed (Comp) and uncompressed (Ctrl) keratinocytes was concentrated in centrifugal concentrator tubes with a pore size of 3 kDa. mDRG were incubated with keratinocyte supernatant 5 h post-isolation. Scale bar 150 µm.

During the current clamp experiments of the small-diameter mDRG neurons, it was observed that the cells frequently died post-sealing or fired action potentials at such a high frequency that they could not be held at a stable holding potential and therefore could not be measured. This indicates that the supernatant incubation caused cellular stress to the cells, potentially due to the presence of neuroactive factors or due to the presence of the remains of the EpiLife keratinocyte media in the supernatant applied. It is noteworthy that the mDRG neurons treated with PCK16 Ctrl supernatant were especially prone to die during patch clamp, again indicating a higher cellular stress level in this condition.
The measured parameters of neuronal excitability revealed a very heterogeneous sample in each of the four conditions. Therefore, only trends could be observed that were not significantly different. The resting membrane potential in each condition varied by 30-50 mV between individual cells (Figure 37A), which is a remarkable difference for a parameter that is usually comparable between the same cell type (e.g., the RMP of iPSC-SN is mainly within a range of 10-20mV). The mean RMP between the groups is comparable, except for the PCK16 Ctrl condition, which had a more depolarized mean RMP. However, in this condition, there are two populations visible: one that has an RMP around -60 mV, comparable to the other conditions and one that has a much more depolarized RMP of -40 to -30 mV. The mean rheobase was highest in the WT Comp and lowest in the PCK16 Comp and the mean action potential amplitude was largest in WT Ctrl and lowest in the WT Comp mDRG neurons, but due to the widespread range of data, no significant difference could be established between the groups (Figure 37B, C). The action potential voltage threshold, half-width, afterhyperpolarization and slope upstroke were overall comparable between the conditions, with small non-significant differences (Figure 37D,E,G,H). The mean action potential time to peak was non-significantly increased in the WT Ctrl mDRG neurons compared to the other groups, due to two action potentials that fired more than 150/ 300 ms after the current pulse onset (Figure 37F). The mean firing frequency was comparable in all conditions except for PCK16 Comp, which showed an increased firing frequency, especially at higher current injections (Figure 37I). However, due to the small n for this condition and the variability within the samples, the difference was non-significant.
In summary, the incubation of mDRG neurons with supernatant from compressed and uncompressed WT and PCK16 keratinocytes did not show a significant difference between the groups or a clear biological trend. The incubation with the supernatant seems to have caused cellular stress in the cells in general, which could contribute to the widespread datasets. Interestingly, the mDRG neurons incubated with supernatant from PCK16 Ctrl were the most different from the other conditions and showed a more depolarized RMP and increased firing frequency (non-significant). These results were unexpected as the cytokine mRNA levels showed a (non-significant) difference between the compressed and uncompressed keratinocytes and the WT and PCK16 cells. The IL-6 and IL-8 mRNA levels were much more increased in the PCK16 compressed cells compared to the uncompressed cells, which is a trend we could not confirm in this experiment.

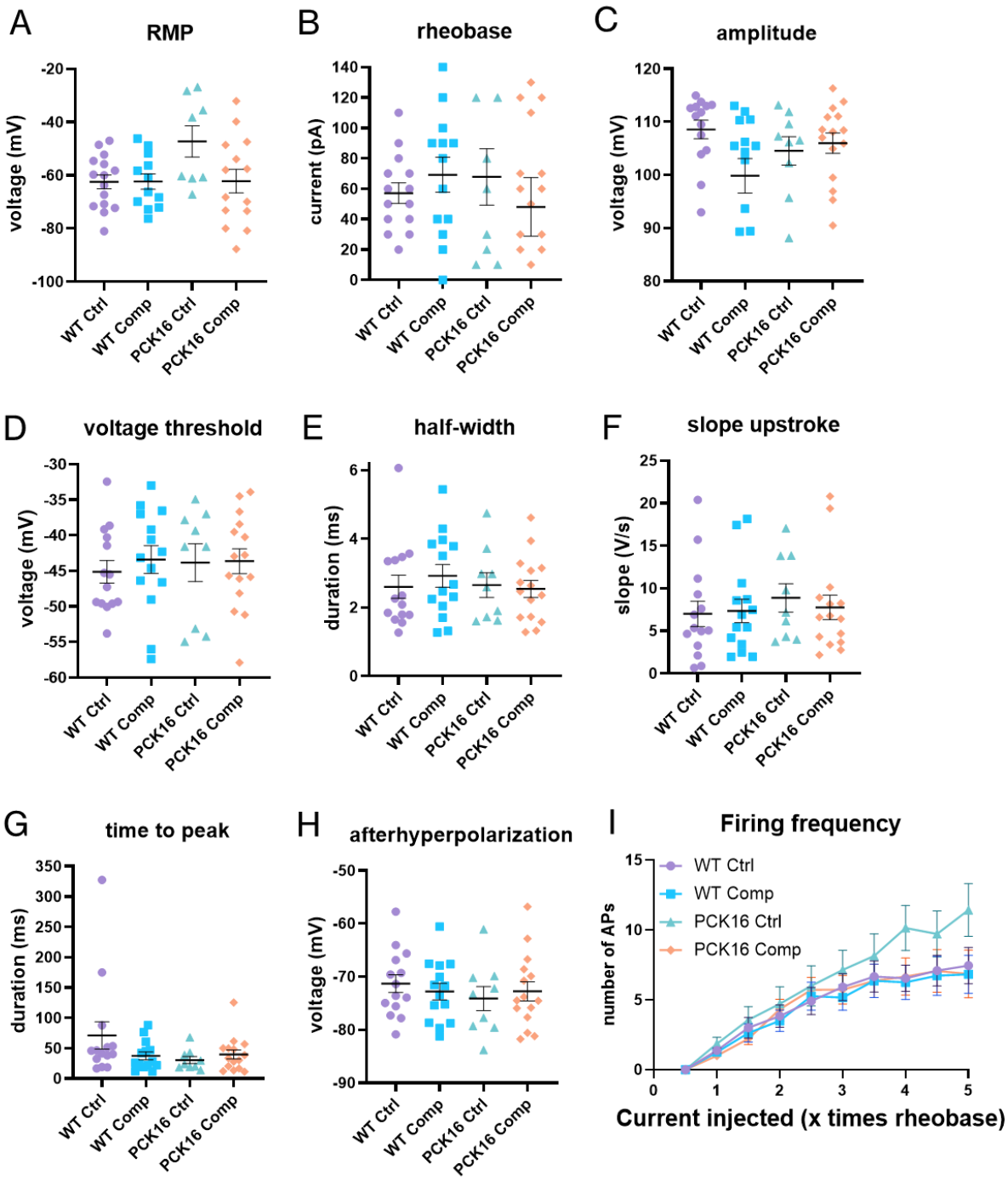

Figure 37 Neuronal activity and action potential characteristics of mDRG neurons stimulated with supernatant from uncompressed or compressed keratinocytes. Dynamic cyclic compression was performed for 1 h at 150 mHz with 0.9 kPa compressive force on WT and PCK16 keratinocytes. Media of compressed (Comp) and uncompressed (Ctrl) keratinocytes was concentrated in centrifugal concentrator tubes with a pore size of 3 kDa. mDRG were incubated with keratinocyte supernatant 5 h post-isolation. A) Resting membrane potential (RMP). B) Rheobase. C) Action potential amplitude. D) Action potential voltage threshold. E) Action potential half-width. F) Action potential slope upstroke. G) Action potential time to peak. H) Action potential afterhyperpolarization. I) Firing frequency: Number of action potentials counted with increasing amounts of current injected (0.5x rheobase increments). Data is presented as mean ±

SEM and was analyzed for statistically significant differences with a one-way ANOVA followed by a Tukey's multiple comparison test (if normally distributed) or a Kruskal-Wallis test followed by Dunn's multiple comparison test (if not normally distributed). *p≤0.05 **p≤0.01 ***p≤0.001 ****p≤0.0001. N compression=3, N patch clamp =1; WT Ctrl n = 13-15, WT Comp n=12-13, PCK16 Ctrl n= 7, PCK16 Comp n=14-15.

6 Discussion

6.1 Neuronal excitability of iPSC-SN compared to hDRG

This thesis analyzed the suitability of current protocols to generate iPSC-SN to model neuropathic pain in two aspects: First, how closely the iPSC-SN can model native sensory neurons/nociceptors in terms of neuronal firing parameters and the expression of TTXr currents, especially $Na_v1.9$. And second, whether iPSC-SN can be used for disease modelling of a $Na_v1.9$ variant. These research aims were examined in three differentiation protocols to ensure that the results were not biased by one technique.

Both the Chambers- and NGN1- differentiation protocols yielded comparable populations of peripherin-positive neurons that fired mature action potentials. Neurons generated via the Chambers protocol exhibited a significantly more depolarized resting membrane potential (RMP) and a lower rheobase compared to NGN1-differentiated neurons. Neuronal excitability and action potential parameters were not assessed for the NBI-differentiated neurons in this study. However, previously published data reported a mean RMP of −69.2 ± 1.35 mV, intermediate between Chambers- and NGN1-derived neurons, and a mean rheobase of 110 ± 10 pA, which was higher than in the present dataset (Röderer, 2021). These differences, however, are likely attributable to methodological variations: the NBI dataset employed a different intracellular patch solution, and rheobase was measured at the RMP rather than at −65 mV, as performed here. Consequently, the observed rheobase difference must be interpreted carefully for its physiological significance.

When evaluating how effectively iPSC-SN recapitulate native hDRG properties, several distinctions emerge. Comparing cell size, it becomes obvious that hDRG neurons exhibit considerably larger diameters, ranging between 28–56 µm, with most cells measuring approximately 42 µm (Davidson et al., 2014; Zurek et al., 2024). Direct comparison of electrophysiological parameters across studies is challenging due to differences in experimental solutions and analytical methodologies; therefore, one-to-one parameter comparisons are limited. Davidson et al. observed an RMP of -62.4 mV in hDRG, which is comparable to the RMP measured for iPSC-SN here (Davidson et al., 2014). Similarly, Zurek et al. compared hDRG to commercially available iPSC-SN and found equivalent RMPs between the two groups (Zurek et al., 2024). Both studies identified markedly higher rheobases in hDRGs (1440 ± 110 pA and 592.7 ± 63 pA, respectively) compared to iPSC-SN (74.2 ± 6.8 pA). However, these differences were no longer significant after accounting for the cell capacitance (Davidson et al., 2014; Zurek et al., 2024). Further distinctions were noted by Zurek et al., who observed that iPSC-SN exhibited more depolarized action potential thresholds and afterhyperpolarization potentials as well as smaller action potential amplitudes and shorter half-widths relative to hDRG (Zurek et al., 2024).

A valuable parameter to assess how closely iPSC-SN can model human nociceptors is the action potential shoulder, which is typical for some subtypes of small-diameter C-fibers in rodent and human DRG neurons (Djouhri et al., 1998; Körner & Lampert, 2022). The amount of neurons displaying action potential shoulders has been found to increase with increasing age of embryonic mDRGs (Lechner et al., 2009). Therefore, the presence of action potential shoulders may indicate neuronal maturation. Furthermore, the presence of action potential shoulders has been associated with the presence of $Na_v1.8$ and $Na_v1.9$ currents (Köster et al., 2025; Stewart et al., 2025). Zurek et al. found action potential shoulders in 96 % of hDRG but only 14 % of iPSC-SN (Zurek et al., 2024). Here, action potential shoulders were observed in 40 % of Ctrl_1 neurons and 12.2 % of Y66S_1 neurons differentiated with the Chambers protocol and 4 % of Ctrl_1, 5 % of

Y66S_1 and 10 % of Y66S_2 NGN1-differentiated iPSC-SN. The presence of an action potential shoulder in a proportion of iPSC-SN could indicate a more mature phenotype of these neurons or a specific subtype identity, as heat-sensitive and IB4-positive DRG neurons are more likely to display an action potential shoulder (Körner & Lampert, 2022). Interestingly, the amount of iPSC-SN showing action potential shoulder was especially high in the Ctrl_1 cell line, but only when differentiated with the Chambers protocol and not with the NGN1 protocol. With the here shown electrophysiological data, it cannot be determined if the Ctrl_1 cell line may produce more nociceptors when differentiated with the Chambers protocol. To analyze this further, a detailed transcriptomics analysis would be useful.

Finally, to assess if iPSC-SN can represent hDRG neurons in neuropathic pain diseases, spontaneous activity is a valuable parameter. In clinical microneurography studies, the proportion of spontaneously active fibers correlates with spontaneous pain intensity in patients (Kleggetveit et al., 2012; Namer & Lampert, 2025). In our experiments with Chambers-differentiated iPSC-SN, patient-derived cells exhibited increased spontaneous activity compared to controls; conversely, NGN1-differentiated neurons showed an opposite trend. Zurek et al. reported low rates (~8 %) of spontaneously active cells in both hDRG and iPSC-SN. Esther Eberhardt (Institute for Neurophysiology, Uniklinik RWTH Aachen, Germany) observed that high levels of spontaneous activity seen in NGN1-differentiated cultures could be attenuated by synaptic blockers during patch-clamp recordings - implying that such activity may at least in part result from dense interconnectivity within cultured networks rather than intrinsic cellular properties (unpublished data). These findings underscore that the optimal conditions for replicating the increased spontaneous activity characteristic of neuropathic pain in iPSC-SN models require further systematic investigation.

In summary, while the RMP values for our iPSC-SN align with those reported for native hDRG and the rheobase values are likely comparable when accounting for the cell size, action potential parameters differ between these models. These discrepancies are probably attributable to variations in ion channel expression profiles.

6.2 TTXr Na_v channels in iPSC-SN: $Na_v1.5$ but not $Na_v1.8$ and $Na_v1.9$?

The functional presence of the TTXr Na_v channels $Na_v1.8$ and $Na_v1.9$ is a hallmark of nociceptor identity. All three differentiation protocols generated TTXr current-positive sensory neurons, despite the differences in neural induction between the protocols. The gating properties of the TTXr currents were comparable across protocols, indicating similar TTXr Na_v subtype compositions.

A $Na_v1.9$-like persistent current could not be observed in cell lines that were tested. To this author's best knowledge, no research group has ever shown $Na_v1.9$ current in iPSC-SN to date and only one group showed $Na_v1.9$-like current in transdifferentiated sensory neurons (Wainger et al., 2015). However, no additional publications showed a $Na_v1.9$-like current in transdifferentiated sensory neurons, leaving the presence of $Na_v1.9$ in this neuronal model uncertain. To enhance $Na_v1.9$ currents that could potentially be present at very low levels, an extended maturation period of 12 weeks and application of the $Na_v1.9$ enhancers Cromolyn sodium, GTP-ɣ-S and the inflammatory mediator PGE2 were applied to iPSC-SN. However, this did not result in an increase in $Na_v1.9$-like currents. Interestingly, after these experiments were performed, a study was published that found that application of an inflammatory soup including PGE2 to hDRG decreased the $Na_v1.9$ current (Zhang et al., 2024). This finding is contrary to the longstanding assumptions of the role of $Na_v1.9$ in inflammatory pain, which is based on rodent models. The

study of Zhang et al. admittedly used a small sample size for these experiments, but it indicates that presumed $Na_v1.9$ enhancers should be investigated in human sensory neurons and not only in heterologous systems and rodent DRG neurons, as mostly done.

In this thesis, a slowly inactivating TTXr current component was observed in iPSC-SN, which is a feature suggestive of $Na_v1.8$ channel activity. Furthermore, a biphasic steady-state fast inactivation was observed, which indicates the presence of two TTXr channels that inactivate at different potentials. Given that no $Na_v1.9$ current could be detected, this is likely a combination of $Na_v1.5$ and $Na_v1.8$. However, application of the presumed selective $Na_v1.8$ blocker VX-548 did not result in a current amplitude reduction or change in gating that would be characteristic for the blockage of $Na_v1.8$. The here applied blocker concentration of 100 nM has been shown to block 100 % of the $hNa_v1.8$ current but none of the other Na_v channel currents in heterologous expression systems (Osteen et al., 2024). Furthermore, the blocker effectively reduced $Na_v1.8$-mediated currents in mouse dorsal root ganglion (mDRG) neurons at higher concentrations - consistent with its lower potency against rodent channels - in our laboratory (unpublished data from Jan Roßberg, Institute of Neurophysiology, Uniklinik RWTH Aachen, Germany). Given these findings, which present contradictory evidence regarding the presence of $Na_v1.8$ in iPSC-SN, two principal interpretations can be considered: 1) the here presumed $Na_v1.8$-like slow inactivating current and bisphasic inactivation do not originate from $Na_v1.8$ and functional $Na_v1.8$ is simply absent in iPSC-SN. However, it is unlikely that a slowly inactivating current would originate from $Na_v1.5$. Alternatively, 2) small quantities of functional $Na_v1.8$ may indeed be present within iPSC-SN, but the pharmacological sensitivity of these channels to VX-548 may differ from that observed for $hNa_v1.8$ expressed in heterologous systems. VX-548 inhibits $Na_v1.8$ by binding to the voltage sensor of domain 2 and stabilizing the closed state of the channel (Osteen et al., 2024). Expression system-related alterations in this region could prevent the blocking of $Na_v1.8$ by VX-548. The literature provides further context but also highlights ongoing uncertainty: Namer et al. showed marginal levels of $Na_v1.8$ mRNA and Alsaloum et al. showed the absence of $Na_v1.8$ mRNA and $Na_v1.8$-like current in iPSC-SN, whereas Schrenk Siemens et al., in contrast, detected SCN10A transcripts encoding $Na_v1.8$ in iPSC-SN (Alsaloum et al., 2021; Namer et al., 2019; Schrenk-Siemens et al., 2022). The evidence in this doctoral thesis cannot definitely confirm or deny the presence of $Na_v1.8$ in iPSC-SN.

The TTXr currents recorded in the iPSC-SN showed a large fast-inactivating component. If this component cannot be solely attributed to $Na_v1.8$, it can most likely be attributed to $Na_v1.5$. The finding of $Na_v1.5$ current but little to no $Na_v1.8$ and $Na_v1.9$ current is consistent with previous reports (Alsaloum et al., 2021; Eberhardt et al., 2015). $Na_v1.5$ current is present at high levels in sensory neurons during development, but only at low levels in uninjured adult hDRG neurons (Renganathan et al., 2002; Tavares-Ferreira et al., 2022). The high prevalence of $Na_v1.5$ currents alongside minimal (if any) $Na_v1.8$ and $Na_v1.9$ currents indicates a developmental phenotype for iPSC-SN. Given that a human pregnancy lasts 9 months and the average iPSC-SN differentiation takes 8 weeks, the iPSC-SN potentially need much more time and/or more complex stimuli during maturation *in vitro* to model native DRG neurons.

6.3 Implications of $Na_v1.8$ and $Na_v1.9$ expression in iPSC-SN for modelling neuropathic pain

To contextualize the above-described TTXr Na_v channel subtype distribution and the subsequent implications for the nociceptor identity of iPSC-SN, studies have been reviewed that investigated the functional roles of these channels in nociceptors. Employing dynamic patch clamp modelling,

which is a combination of electrophysiology and computer modelling, work by Alsaloum et al. suggests that $Na_v1.9$ plays a significant role in setting the RMP, with increasing levels of $Na_v1.9$ current depolarizing the RMP (Alsaloum et al., 2021). Furthermore, the action potential threshold was positively influenced by $Na_v1.9$ current in a nonlinear manner. Köster et al. integrated electrophysiology data from heterologous expression systems into a Hodgkin-Huxley-based model and reported the a for $Na_v1.9$ in the action potential upstroke and shoulder (Köster et al., 2025). However, analysis of the small-diameter DRG of $Na_v1.9$ k.o. mice showed no difference in the RMP, action potential threshold, amplitude, duration or afterhyperpolarization compared to WT mDRG (Priest et al., 2005). While the rheobase was modestly increased and the firing frequency was slightly reduced in k.o. DRG, neither change reached statistical significance.
For $Na_v1.8$, dynamic clamp and computational modelling have consistently shown its importance for action potential overshoot and half-width, likely attributable to its depolarized activation and inactivation kinetics (Alsaloum et al., 2021; Köster et al., 2025). These predictions have been validated *in vitro,* where DRG neurons of $Na_v1.8$ k.o. mice showed smaller action potentials with a slower rise slope (Renganathan et al., 2001). Pharmacological blocking of $Na_v1.8$ with VX-548 prevented more than half of the measured hDRG neurons from firing action potentials (Osteen et al., 2024).
While the role of $Na_v1.8$ in nociceptor firing seems to be well established *in silico* and *in vitro*, the *in silico* and *in vitro* data of the role of $Na_v1.9$ in neuronal excitability seem to deviate between different studies. Interestingly, in a $Na_v1.8$/$Na_v1.9$ double-k.o. mouse model, the RMP and action potential half-width of the k.o. DRG neurons were unaltered compared to the WT DRG neurons (Alves-Simões et al., 2025). The action potential peak amplitude was reduced by 15 mV and the afterhyperpolarization and voltage threshold were decreased in the k.o. DRG compared to the WT DRG. The only difference in behavioral assays was a significantly higher threshold to the Randall Selitto test that measures the response to noxious mechanical stimuli, but no differences in the responses to heat, cold or von Frey hairs were recorded. Given that these double k.o. mice showed no TTXr currents; it is remarkable that their response to noxious heat and cold stimuli is unaltered. Considering the results of the *in silico* models, these results were in line with the prediction for a $Na_v1.8$ k.o., but unexpected for a $Na_v1.9$ k.o.. A plausible explanation for this discrepancy is compensatory upregulation or altered function of other sodium channels upon a deletion of an important Na_v channel gene, allowing for continued functional pain detection. This would explain differences between the results of computer modelling, where currents can be acutely added or subtracted, compared to *in vivo/ in vitro* models, where the cellular organisms may be searching for compensatory mechanisms.
In summary, loss of functional $Na_v1.8$ would be expected to reduce action potential amplitude and slow its rising phase. Nevertheless, the iPSC-SN examined here exhibited robust action potentials with substantial amplitude and speed, although it cannot be determined whether these properties are mediated by $Na_v1.8$. While $Na_v1.9$ is presumably involved in the regulation of the resting membrane potential and action potential threshold, this has not been confirmed *in vitro* or *in vivo* data. Therefore, it is difficult to determine what effect the absence of $Na_v1.9$ would have on the function of iPSC-SN as nociceptors. It is plausible that small/ absent levels of $Na_v1.8$ or $Na_v1.9$ currents could be compensated for by other ion channels. However, this hypothesis warrants further research to determine if and which compensatory mechanisms take place and how this affects the function of iPSC-SN in comparison to hDRG.

6.4 Modelling the $Na_v1.9$-Y66S variant in iPSC-SN

In this thesis, it was assessed whether iPSC-SN are a suitable model for neuropathic diseases. This was examined using the iPSC obtained from two directly related small fiber neuropathy patients carrying a Y66S variant in SCN11A. The Y66S_1 iPSC-SN of the mother exhibited significantly increased firing rates and almost twice as many tonic firing neurons compared to the age- and gender matched Ctrl_1 when differentiated with the Chambers protocol. Furthermore, the action potential shape was significantly narrower and showed a faster upstroke and time to peak. The narrower action potential shape has also been reported for mDRG neurons transfected with $Na_v1.9$-Y66S compared to $Na_v1.9$-WT controls (van den Braak et al., 2025). These phenotypic differences could not be found in the NGN1-differentiated iPSC-SN. Here, only a non-significant increase in the Y66S_1 firing frequency compared to the control could be observed. Further analysis revealed that the Ctrl_1 cell line was significantly different when differentiated with the Chambers protocol compared to the NGN1 protocol in terms of the RMP, rheobase, action potential voltage threshold, time to peak, afterhyperpolarization, shoulder prominence, shoulder width and firing frequency above 1.5 x rheobase injection. In comparison, the Y66S_1 iPSC-SN only differed in RMP, rheobase and voltage threshold between the two differentiation protocols. This raises the question of which differentiation protocol modelled the control phenotype in iPSC-SN more realistically. Unfortunately, this question cannot be determined with the present data set and would best be further pursued by employing an isogenic control cell line created from the patient cell line.

However, it can be discussed if the observed phenotype of $Na_v1.9$-Y66S in the Chambers differentiated iPSC-SN could be representative of the *in vivo* phenotype, despite the lack of overt persistent $Na_v1.9$-like currents in these cells. The presence of a phenotype is supported by analogous findings of Namer et al., who demonstrated altered firing rates on multi-electrode arrays for iPSC-SN harboring a likely pathogenic SCN11A variant (Namer et al., 2019). While the study did not investigate $Na_v1.9$ currents in iPSC-SN, the observed phenotype was reversible *in vitro* and *in vivo* with Lacosamide treatment. This indicates at least a partially correct modelling of the neuropathic pain experienced by the patient in iPSC-SN. The contradiction between the lack of clearly observable $Na_v1.9$ current and a visible phenotype can be explained by three hypotheses. 1) There are marginal levels of $Na_v1.9$ current present in the iPSC-SN, which are indistinguishable from the noise of the leak currents (~ 200 pA) with the methods applied here, but still influence the firing behavior of the neurons. The persistent current component of $Na_v1.9$ may affect the resting membrane potential and AP shape even if the macroscopic current is not distinguishable. The Y66S substitution occurs within a phosphorylation motif that is conserved across various Na_v subtypes. This phosphorylation motif is predicted to be a target of the Fyn kinase, but the replacement of tyrosine with serine potentially creates a target side for the protein kinase A (PKA) instead (van den Braak et al., 2025). Activity of PKA-dependent pathways has a well-documented role in inflammatory pain responses and nerve sensitization (Basbaum et al., 2009; Hucho & Levine, 2007). Thus, this amino acid change may alter intracellular signaling cascades contributing to neuropathic pain phenotypes through interactions with other proteins within sensory neurons. Therefore, even low levels of $Na_v1.9$ with the Y66S variant may potentially result in a change in neuronal excitability through altered intracellular signaling cascades. 2) An additional variant is present in the patient cells and causes the phenotype. The patient cells were genetically screened for additional pathogenic or likely pathogenic variants associated with sensory disorders; however, new pain-related genes are frequently being discovered (Middleton et al., 2025). It is also possible that not one additional variant in a pain-related gene is causing the phenotype, but that multiple, perhaps even partially benign variants affect the neuronal

excitability in combination. Interestingly, NGN1-differentiated iPSC-SN from the Son (Y66S_2) showed a reduced firing frequency (non-significant) compared to the control cell line. Remarkably, the Son does not report any pain symptoms, while the mother is affected by pain episodes. This contrast highlights the phenotypic heterogeneity among individuals sharing identical genetic Na_v variants (Mis et al., 2019), which suggests that additional genetic or epigenetic factors modulate the disease manifestation beyond the presence of the SCN11A variant alone. 3) The observed $Na_v1.9$-Y66S phenotype in the Chambers-differentiated neurons does not replicate neuropathic changes, but rather genetic variability between donor cell lines. For example, a difference was visible in the gating between Ctrl_2 and Ctrl_3 iPSC-SN differentiated with the NBI protocol, despite the fact that both stem from healthy donors. To investigate which of these hypotheses may apply, an isogenic control cell line should be generated from the two patient cell lines. Given that iPSC-derived neurons retain each patient's full genotype, additional genetic factors that could produce a phenotype would be maintained in isogenic controls, while only the $Na_v1.9$-Y66S variant would be removed. Therefore, an isogenic control cell line would aid in determining if the observed phenotype is solely resulting from the Nav1.9-Y66S variant or if there are more factors contributing to it.

6.5 Challenges in functional expression of $Na_v1.9$

The functional presence of $Na_v1.9$ in the form of its characteristic persistent current has not been confirmed in iPSC-SN yet and could not be demonstrated within the scope of this thesis. Although studies employing the Chambers and NGN1 differentiation protocols have detected $Na_v1.9$ mRNA in iPSC-SN - albeit at lower levels compared to $Na_v1.7$ (Namer et al., 2019; Schrenk-Siemens et al., 2022) - the translation of this transcript into a functional membrane protein remains elusive. Attempts to heterologously express $Na_v1.9$ have generally yielded low success rates, with only a limited number of research groups reporting successful expression at low efficiency (Leipold et al., 2013; Lin et al., 2016; Vanoye et al., 2013). In the present study, efforts to express $Na_v1.9$ currents in SH-SY5Y cells were not successful. Notably, groups that have successfully expressed $Na_v1.9$ in heterologous expression systems performed extensive modifications to their expression systems. For instance, Theys et al. (2025) achieved expression of mouse $Na_v1.9$ in ND7/23 cells only after incorporating a vector with a regulatory element to enhance gene expression, co-transfecting β-subunits 1 and 2, and incubating cells at 28°C post-transfection (Theys et al., 2025). In contrast, none of these adaptations were necessary for the robust expression of $Na_v1.5$. Despite such efforts, these strategies failed to express functional human $Na_v1.9$ in ND7/23. Functional $hNa_v1.9$ currents could only be obtained by Theys et al. by generating chimeric channels combining domains from $Na_v1.9$ with those from $Na_v1.5$, an approach that has previously been shown by other groups with domains from $Na_v1.4$ or $Na_v1.7$ (Bothe & Lampert, 2021; Goral et al., 2015; Sizova et al., 2020).

The detection of $Na_v1.9$ mRNA in iPSC-SN and the successful generation of current from chimeric constructs suggest that the principal obstacle to functional expression is likely post-translational rather than transcriptional or translational in nature. Within this work, I attempted to assess whether iPSC-SN possess the necessary cellular machinery for proper translation and membrane integration of exogenous $Na_v1.9$ mRNA through plasmid transfection experiments. However, these experiments proved inconclusive since only apoptotic cells appeared to uptake the plasmid and exhibit fluorescence, without any detectable $Na_v1.9$ current. Here, the plasmid was attempted to be transported into the cells via the transfection agent JetPei, which is frequently used for channel expression in heterologous systems. In a consecutive experiment, viral

transduction could be tested to express $Na_v1.9$. This strategy has already been performed successfully in the NGN1 protocol at the neural crest stage to overexpress the transcription factor NGN1.

A potential explanation for the difficulty in expressing functional $Na_v1.9$ can perhaps be found in its sequence. Of the nine VGSCs, $Na_v1.9$ shows the least sequence homology with the other Na_v channels (Dib-Hajj et al., 2015). Consequently, several studies have focused on identifying specific regions of $Na_v1.9$ that are different from other Na_v channels. These studies have highlighted an essential role for the C-terminus—particularly a segment comprising 49 amino acids spanning the pre-IQ and EF-hand regions—in regulating both channel trafficking/expression and gating behavior (Sizova et al., 2020; Theys et al., 2025). Substituting this region with that from $Na_v1.7$ significantly increased surface expression and current amplitude when expressed in HEK293 cells (Sizova et al., 2020). Conversely, replacing the C-terminal tail of $Na_v1.5$ with that from $Na_v1.9$ led to a marked reduction (~50%) in current density when expressed in ND7/23 cells (Theys et al., 2025). While these findings implicate differences within the C-terminus as central determinants limiting functional channel expression - and contributing to persistent current characteristics - the precise molecular mechanisms remain unclear. While functional expression of $Na_v1.9$ is difficult in heterologous expression systems and iPSC-SN, native rodent and human DRG neurons robustly express large-amplitude endogenous $Na_v1.9$ currents (Zhang et al., 2024). This suggests that commonly used model systems may lack or overexpress critical proteins or systems regulating channel expression, post-translational modification or trafficking of Na_v channels. Such systems include the 'RXR' motif, which regulates the retention of Na_vs in the ER or the neuronal precursor cell-expressed developmentally down-regulated 4 (Nedd4) ubiquitin ligase, which can induce degradation of Na_vs (Shao et al., 2009). Various proteins have been linked to the trafficking of Na_vs, including Ankyrins, Synotrophins, S100A10, plakophilin-related armadillo-repeat protein-interacting protein (papin), the ezrin/radixin/moesin (ERM) family of proteins or beta subunits of Na_v channels. Furthermore, phosphorylation of Na_vs by kinases can occur at multiple sites and can alter both kinetics and expression via intracellular trafficking. Relevant kinases for Na_v channel phosphorylation are PKA, PKC or the Calcium-dependent CaM kinase II (CaMKII) and the second messenger calmodulin. Finally, increasing evidence suggests that Na_vs build large, multi-protein complexes, including cytoskeletal proteins such as actin. Interaction with cytoskeletal proteins could regulate Na_v trafficking (Shao et al., 2009). The here listed proteins and systems have been found to interact with certain Na_v subtypes and influence their expression, but the exact mechanism how they regulate Na_v expression remains largely unknown. Especially data on the regulation of $Na_v1.9$ expression is lacking.

In summary, despite evidence for the presence of SCN11A mRNA in iPSC-SN models and advances using engineered chimeric constructs, the reliable functional expression of wild-type human $Na_v1.9$ remains challenging both in heterologous systems and patient-derived neurons under standard conditions. Further investigation into cell-specific regulatory mechanisms will be crucial for overcoming these barriers.

6.6 iPSC-SN as a model for neuropathic pain: summary and outlook

The aim of this thesis was to assess the suitability of iPSC-SN as neuropathic pain models with the focus on TTXr-, especially $Na_v1.9$- currents, and the neuronal excitability and action potential characteristics of these cells. The results highlight both the promise and current limitations of iPSC-SN as a model for neuropathic pain. iPSC-SN can generate TTXr current and fire mature action potentials, with RMP and rheobase values that can roughly be compared to hDRG neurons.

Studies have successfully used iPSC-SN to model neuropathic diseases, including IEM, SFN and CIP and neuropathic changes upon chemotherapeutic application (L. Cao et al., 2016; McDermott et al., 2019; Meents et al., 2019; Mis et al., 2019; Namer et al., 2019; Schinke et al., 2021; Yuan et al., 2021). Additional studies have found that iPSC-SN can recapitulate the pseudo-unipolar structure of DRG neurons, that they express functional voltage-gated calcium and potassium channels and TRP channels, and can detect cold and mechanical stimuli (Deng et al., 2023; Hulme et al., 2020; Schrenk-Siemens et al., 2022). However, the presence of functional $Na_v1.8$ or $Na_v1.9$ currents could not be conclusively demonstrated in this work. If the currents are present, they appear to exist only at marginal levels, deviating from hDRG neurons. This limits the suitability of iPSC-SN for modelling neuropathic pain conditions associated with variants in these channels, but also other Na_v channels, as $Na_v1.8$ and $Na_v1.9$ regulate nociceptor function.

Despite these shortcomings, iPSC-SN provide the unique opportunity to recapitulate the complete genetic background of individual patients in one model rather than focusing only on one variant. The importance of the holistic approach is underscored by the differences observed in this study in the firing frequency between the iPSC-SN of the mother and the son carrying the same $Na_v1.9$ variant but showing different phenotypes. The mother experienced pain episodes and presented increased neuronal excitability, while the son remained asymptomatic and presented reduced excitability. Such differences suggest that factors beyond the primary genetic variant contribute to disease manifestation—a complexity that would likely be missed using heterologous or rodent models restricted to isolated mutations. While this thesis focuses on VGSCs, it is important to recognize that voltage-gated calcium and potassium channels, among others, also play critical roles in peripheral neuronal signaling. As all of these channels contribute to the electrical characteristics of a neuron and influence each other, they should ideally not be studied in isolation in heterologous expression systems. At present, iPSC-SN are the only model that allows for the study of the role of ion channel variants in neuropathic pain in a human cellular context in the presence of various other ion channels relevant for neuronal excitability, as we cannot obtain hDRG neurons from neuropathic pain patients of interest. Moreover, iPSC technology holds promise for advancing personalized medicine approaches, as shown by the SFN patient who was successfully treated with Lacosamide after the drug had been tested on her iPSC-SN first (Namer et al., 2019).

To enhance the reliability of iPSC-SN as a model for neuropathic pain, further maturation of these cells is necessary, particularly with respect to achieving robust expression of $Na_v1.8$ and $Na_v1.9$ currents. Neuronal networks are plastic, meaning that they constantly change depending on input. It is plausible that exposure to sensory stimuli such as temperature changes, mechanical pressure, or noxious chemicals during late-stage differentiation could facilitate further maturation toward a phenotype more closely resembling native nociceptors. This hypothesis could be experimentally investigated by applying various stimuli during the final phase of the iPSC-SN maturation process (last 2-3 weeks), observing if this may generate more mature iPSC-SN. Additionally, established protocols rely predominantly on small molecules or genetic cues for differentiation while neglecting mechanical cues such as substrate stiffness. However, durotaxis- cell migration guided by rigidity gradients- is an essential part of neural crest migration and may even prime the cells for further differentiation into sensory neurons (Barriga et al., 2018). Therefore, the ideal substrate stiffness for iPSC, neural progenitors and immature neurons should be tested and consequently incorporated into iPSC-SN.

Careful selection and use of control cell lines remain essential for accurate disease modelling using iPSC-SN. Notably, significant variability can exist between healthy donor-derived lines due to benign genetic differences affecting excitability or action potential properties. Therefore,

multiple control cell lines and ideally multiple patient cell lines should be employed whenever possible. Alternatively, CRISPR/Cas9-mediated genetic correction can generate isogenic controls directly from patient lines. This approach allows for the study of one likely pathogenic variant, while the native cellular background will remain the same in the patient and the isogenic control cell line. However, usage of isogenic controls should be accompanied by extensive genetic screening to rule out any off-target effects of genetic engineering.
In summary, although iPSC-SN do not yet fully recapitulate all features of native hDRG neurons—particularly regarding $Na_v1.8/1.9$ channel expression—they constitute a promising platform for modelling sensory neuron pathophysiology associated with neuropathic pain *in vitro*. Considering that induced pluripotent stem cell technology was first described less than two decades ago; continued advances are likely to further enhance their utility and fidelity as a translational research tool.

6.7 A device for cyclic compression of keratinocytes to model neuropathic pain

The aim of this thesis was to develop a device to cyclically compress keratinocytes and investigate if healthy and PC keratinocytes under mechanical stress could sensitize sensory nerves. In this collaborative project, a monolayer compression system was developed, consisting of a custom-designed compression device and an area-restricted keratinocyte monolayer seeding system. Optimal parameters were determined to cause cellular stress in keratinocytes without inducing apoptosis. mRNA analysis showed a trend in which IL-1α, IL-1β and TNF-α were intrinsically higher expressed in PC cell lines compared to WT lines, indicating a pro-inflammatory phenotype. Application of cyclic compression at 150 mHz for 1 h with a compressive force of 0.9 kPa induced an upregulation of cytokine mRNA across all cell lines. Notably, the PC cell lines exhibited a more pronounced increase in IL-6 and IL-8 mRNA expression relative to WT. Not all observed changes in cytokine expression levels were statistically significant between groups, but the general upregulation of cytokines in PC cell lines and following compression shows a clear biological trend.
To assess whether this upregulation of cytokine mRNA translated into sensitization of sensory neurons, conditioned media from both compressed and control keratinocyte samples was applied to mDRG. Contrary to expectations, no differences in neuronal excitability or action potential characteristics could be found between the groups. Furthermore, considerable heterogeneity was observed within each group. This apparent discrepancy between qPCR data and patch clamp results could have two different explanations. First, increased cytokine mRNA levels may not necessarily correspond to elevated secretion of cytokines; post-transcriptional regulation often leads to disparities between mRNA abundance and protein output or secretion profiles. Alternatively, it is possible that the experimental conditions employed—specifically the use of concentrated keratinocyte media—were inherently prone to enhance neuronal excitability in mDRG neurons across all groups, thereby masking any group-specific effects.
The mDRG neurons were incubated in a mixture of concentrated EpiLife keratinocyte media and their standard DMEM high glucose media. Concentration of the keratinocyte media by centrifugal filtration through a 3 kDa membrane resulted in the excretion of a clear substance with low molecular weight components, while larger molecules remained highly concentrated within the membrane. The exact composition of the EpiLife media is proprietary, but the media is supplemented with human keratinocyte growth supplement (HKGS) which contains insulin-like growth factor 1 (IGF-1), hydrocortisone, bovine transferrin and epidermal growth factor. As a

result, before accounting for secreted cytokines, the final incubation medium for mDRG neurons contained presumably higher concentrations of serum and growth factors than typically used for these neurons. This could account for the high excitability and spontaneous activity of the mDRG neurons observed during patch-clamp recordings, irrespective of experimental group. To address this in further experiments, it would be advisable to perform compressions using DMEM high-glucose medium rather than EpiLife supplemented with HKGS. DMEM high glucose media is tolerated by keratinocytes and does not inherently alter the mDRG firing frequency, so all observed changes could be attributed to an alteration of secreted factors by the keratinocytes. Moreover, direct quantification of cytokine protein levels via Enzyme-linked Immunosorbent Assay (ELISA) should be implemented. While this step was initially omitted due to an emphasis on functional outcomes rather than absolute cytokine quantities, such measurements would provide critical insights into optimal experimental conditions for incubating sensory neurons with keratinocyte supernatants. Additionally, mDRG media could be supplemented with the amount of recombinant cytokines found in the compressed keratinocyte supernatant for more controllable experimental conditions.

6.8 The role of Krt6 and Krt16 in inflammation

In this thesis, two keratinocyte cell lines derived from PC patients harboring mutations in KRT6a (PCK6) and KRT16 (PCK16) were investigated. Distinct differences were observed in the baseline phenotype and response to cyclic compression between these cell lines. Specifically, PCK6 keratinocytes showed a trend of intrinsically higher levels of IL-1α and IL-1β mRNA before compression, whereas the PCK16 cells showed a trend of greater upregulation of IL-6 and IL-8 following compression. This difference in responses by the keratinocytes can be explained by the well-established genotype-phenotype relationship in PC patients. Variations in symptom distribution and severity between PC patients are closely linked to specific keratin mutations (McCarthy et al., 2023). For instance, follicular hyperkeratosis is exclusively found in adolescent PC patients carrying a mutation in Krt6 (Pachyonychia Congenita Research & Support Project, 2021). Functionally, Krt6 is implicated in wound healing processes, while Krt16 is assumed to play a role in innate immunity (Lessard et al., 2013; Rotty & Coulombe, 2012). The two keratins operate as functional counterparts and are therefore closely linked to each other.

This study revealed a pro-inflammatory phenotype in both PC keratinocyte lines that was exacerbated by cyclic compression. Supporting evidence for these findings can be found in the literature. Lessard et al. developed a KRT16 null mouse model in which the mice showed footpad lesions analogous to the palmoplantar keratoderma (PPK), i.e., thick callus on the hand and feet, as present in PC patients. Notably, these lesions arose predominantly at sites of high mechanical stress, suggesting a role for Krt16 in mechanotransduction. Lesional skin from these mice showed transcriptional hyperactivation of cytokines and damage-associated molecular patterns (DAMPs), including IL-1α, IL-1β, chemokine (C-X-C motif) ligand 2, chemokine (C-C motif) ligand 5, S100 calcium-binding protein A9, β-Defensin 4, small proline-rich protein 2D, serine peptidase inhibitor B3a, stefin A1 and stratifin. In addition, upregulation of Krt6a was observed (Lessard et al., 2013).

The underlying molecular mechanism for the observed pro-inflammatory phenotype in KRT16 null mice and the PC keratinocytes may involve altered intracellular signaling pathways associated with keratin expression. Krt16 is a target for EGFR and ERK signaling (Chen et al., 2007; Kerns et al., 2010; Y. N. Wang et al., 2006; Y. N. Wang & Chang, 2003). Overexpression of Krt16 has been shown to enhance EGFR signaling, which can enhance MAPK/EGF signaling and thereby

modulate DAMP signaling (Paladini & Coulombe, 1998). For instance, EGFR activation leads to Erk1/2 signaling, which promotes increased production of IL-1α (Hobbs & Watt, 2003). IL-1α can further interact with the MAPK signaling, resulting in epidermal inflammation and keratinocyte proliferation, ultimately creating an autoimmune feedback loop (Freedberg et al., 2001; Hobbs et al., 2004). Less is known about the role of Krt6 in inflammation, but it has been shown that focal adhesion complexes are altered in KRT6 null keratinocytes (Rotty & Coulombe, 2012). Focal adhesion complexes contain integrins, the IL-1 receptor and the EGF-receptor, which are all relevant for pro-inflammatory processes (Wong et al., 2011).

While direct evidence supporting roles for Krt16, and to a lesser extent Krt6, in epidermal inflammation remains limited at present, these findings nevertheless suggest that epidermal inflammation plays a role in PC pathogenesis. If inflammatory mechanisms are indeed excessively induced downstream of keratin mutations, they may present the missing link between genetic keratin defects and neuropathic pain experienced by PC patients. Inflammation is well-known to induce nociceptor sensitization, which could explain both the neuropathic pain and reduced IENFD through overexcitability of sensory neurons in patients with PC (Basbaum et al., 2009; Julius & Basbaum, 2001). Further research is warranted to clarify the contribution of inflammation to PC pathology and establish its connection with neuropathic pain phenotypes. In particular, systematic evaluation of skin biopsies from human PC patients for inflammatory markers would be instrumental in advancing understanding within this field.

6.9 Mechanically compressed keratinocytes as a model for neuropathic pain: summary and outlook

This thesis demonstrates the application of a newly developed dynamic cyclic compression system for modelling mechanically exacerbated skin diseases with neuropathic pain components. The compression parameters employed (150 mHz, 1 h, 0.9 kPa) are easily adjustable to simulate various physiological situations. For the research on PC, extending the duration or periodicity of cyclic compression would be particularly interesting to mimic the recurrent mechanical stress experienced by the patients' feet. Here, keratinocytes and mDRG neurons were cultured separately to ensure that the mechanical compression affected only the keratinocytes and any change in neuronal excitability would be solely keratinocyte-mediated. However, in the native skin, both keratinocytes and free nerve endings respond to changes in the mechanical load. To more closely model this interaction, the compression system could be adapted to a microfluidic co-culture system with two chambers - one for mDRG and one for keratinocytes - connected through narrow channels permitting neurite outgrowth and biological communication. Such microfluidic systems have been developed by different research groups; recently, an advanced model has been published by Ahn et al. (Ahn et al., 2023; Schutte et al., 2021). The co-culture system could be extended with the compression device. The custom-designed and 3D-printed nature of the current device allows for straightforward modifications to accommodate chambers of varying sizes or shapes. Compression could then be selectively applied to compartments containing keratinocytes and nerve endings, subjecting the nerve somas only to input via the keratinocytes and nerve endings. Furthermore, following the establishment of such a system, mDRG neurons could be replaced with PC patient-derived iPSC-SN to generate a fully humanized PC disease model.

In recent years, large advances have been made in the development of complex 3D skin equivalents featuring multiple cell types. Vidal et al. developed a composite system comprising a hypodermis with adipocytes, endothelial cells and smooth muscle cells, a dermis with

fibroblasts, an epidermis with keratinocytes and an additional layer with human induced neural stem cells (Vidal et al., 2019). The cells were embedded in a collagen-silk composite, allowing for long-term culture (>42 days). Rousi et al. introduced a model integrating iPSC-SN alongside human keratinocytes and fibroblasts (Rousi et al., 2022), while Lee et al. developed hair-bearing human skin organoids from iPSC that also featured neurons (Lee et al., 2022). These models are suitable for patient-specific neuropathic pain modelling. Lastly, technological advancements are facilitating the structural organization of these models in an *in vivo*-like manner. Rose et al. developed an anisotropic hydrogel activated by a mechanical field that can provide structural guidance for neurites to grow upwards towards keratinocytes, as seen in native skin architecture (Rose et al., 2017) (Doctoral thesis of Srijeeta Nag Biswas, Institute of Neurophysiology, Uniklinik RWTH Aachen, Germany).

While these complex systems represent significant strides towards recapitulating *in vivo* cellular environments, simpler mono- or co-culture models remain indispensable for elucidating fundamental molecular mechanisms. Previous studies employing advanced multicellular constructs have largely relied on immunocytochemistry or qPCR for analysis; however, addressing specific questions regarding the molecular influence of mechanically stressed keratinocytes on sensory neurons - as explored here - requires electrophysiological approaches to precisely determine neuronal activity. Introducing additional cell types enhances physiological relevance but simultaneously complicates attribution of observed effects to specific cellular contributors. Therefore, initial investigations into how compressed keratinocytes affect sensory neuron function are best conducted using simplified mono- or co-culture systems. These findings can subsequently be transferred to more complex models featuring advanced technologies for stimulation and analysis, for instance, an integrated compression system or an integrated multi-electrode system to record neuronal activity.

In summary, substantial progress has been made in developing 3D *in vitro* skin equivalents comprising multiple cell types, but basic models remain essential for advancing our understanding of mechanobiology and neurobiology within cutaneous tissues at the molecular level. Models of reduced cellular and structural complexity that include advanced stimulation and analysis techniques- as presented here- are highly relevant in improving the understanding of the molecular pathology before investigating the disease on a more holistic, multi-tissue level.

6.10 The ultimate model for neuropathic pain- what should it look like?

Neuropathic pain is a complex disease. The peripheral pain stimuli and nerve sensitization modelled and analyzed in this thesis are only one part of the pain process. An ideal model for peripheral nerve sensitization in neuropathic pain would require four elements: 1) patient-derived sensory neurons and surrounding cells such as keratinocytes, fibroblasts, immune cells and glial cells, 2) a structural 3D organization mimicking the structure of the skin and the spatial segregation of free nerve endings and neuronal soma *in vivo*, 3) a stimulation system to include nociceptive triggers such as noxious pressure or temperature and 4) one or ideally multiple read-out systems for electrophysiological and molecular analysis of the individual cell types. However, in an increasingly complex and multicellular model, controlling all cellular and acellular factors becomes increasingly difficult.

Cells can be classified as self-adapting complex systems, meaning that they are influenced by many external factors, which causes them to respond and adapt, thereby changing the nature of *in vitro* systems (Ma'ayan, 2017). While this is true for simple and complex biological *in vitro* systems, controlling the parameters in a highly developed system is more difficult. At the same

time, the dean of the medical faculty of the RWTH Aachen University Stefan Uhlig once stated "Nothing in biology makes sense unless it is understood in terms of complex self-adaptive systems". Therefore, any biologist aiming to research mammalian systems is faced with the issue of the trade-off between the *in vivo*-like complexity vs the simplified, analyzable model and there does not seem to be a perfect way.

Here, simplified 2D models were analyzed to close the basic research gaps. It became evident that while both the iPSC-SN and the keratinocytes under mechanical compression are suitable models to investigate different aspects of neuropathic pain *in vitro*, both models will benefit from future improvements. Finally, to cite George Box, "All models are wrong", a statement which can be extended with the addition of "but some are useful". No neuropathic pain model available today or in the near future can model the disease in its entire complexity. Therefore, models should be viewed as an estimation of the true biological processes and an opportunity to investigate specific aspects of a disease, which need to be added into the disease context. This requires scientists to be honest and critical with their models and to validate data in multiple available models. To conclude, neuropathic pain models have advanced rapidly in the last decades with the establishment of iPSC-neurons and the acknowledgement of the role of neuron-surrounding cells in pain, but the models still face limitations in terms of complexity and integrating stimulation and neuronal recording devices.

This thesis showed that the TTXr currents in iPSC-SN are likely to be generated by $Na_v1.5$ to a large extent and potentially by $Na_v1.8$ to a lesser extent. The $Na_v1.9$ currents are either absent or too small to be detected with conventional voltage clamp. Furthermore, a phenotype was observed for the $Na_v1.9$-Y66S pain variant in Chambers-differentiated iPSC-SN, but not NGN1-differentiated iPSC-SN. Overall, iPSC-SN can recapitulate hDRG neurons in many parameters, but not all of them yet. To analyze the role of keratinocytes under mechanical compression in PC, a dynamic cyclic compression device was developed. Here, it was shown for the first time that PC keratinocytes exhibit a pro-inflammatory phenotype that exacerbated following cyclic compression. The collective results showed that while both models show promise in neuropathic disease modelling, future improvements need to be made to obtain data that can be translated into the clinic and aid the understanding and treatment of neuropathic pain.

7 List of abbreviations

AM= Acetoxymethylester	Nav= Voltage-gated sodium channels
AmpR= Ampicillin resistance gene	NCLC= Neural crest-like cell
AP= Action potential	Nedd4= neuronal precursor cell-expressed developmentally down-regulated 4
AP-axis= Anterior-to-Posterior Axis	NeoR/KanR = Neomycin/ kanamycin resistance gene
BDNF= Brain-derived neurotrophic factor	NGF= Nerve growth factor
BleoR= Bleomycin resistance gene	NGN= Neurogenin
BMP= Bone morphogenetic protein	NPC= Neural progenitor cells
BRN3A= brain-specific homeobox/POU domain protein 3A	Ori= Origin
CaMKII= Calcium-dependent CaM kinase II	Papin= plakophilin-related armadillo-repeat protein-interacting protein
cAMP= cyclic adenosine monophosphate	PBMCs= Peripheral blood mononuclear cells
CIP= Congenital insensitivity to pain	PBS= Phosphate buffer saline
CMi= Mechano-insensitive C-fibers	PC=Pachyonychia Congenita
CNS= Central nervous system	PCR= Polymerase chain reaction
CS= Cromolyn Sodium	PEEK= Polyether ether ketone
Ctrl= Control	PEPD= paroxysmal extreme pain disorder
D= Domain; if followed by a number D= days of differentiation	PGE2= Prostaglandin E2
DAMP= Damage-associated molecular pattern	PI= Propidium iodide
DIV= Days *in vitro*	PK= protein kinase
DRG= dorsal root ganglia	PM = Pore domain
ECM= Extracellular matrix	PNS= Peripheral nervous system
ECS= Extracellular solution	PPK= Palmoplantar keratoderma
EMT= Epithelial-to-mesenchymal transition	R^2= regression coefficient
ENaC= Mammalian epithelial sodium channels	RMP= Resting membrane potential
Ezrin/radixin/moesin = ERM family	Rock= Rho-associated protein kinase
G= Conductance	Rser= Series resistance
GDNF= Glial cell line-derived neurotrophic factor	RT= Room temperature
GFP= Green fluorescent protein	S= Segment
GOF= Gain-of-function	SD= Standard deviation
h= Human	SEM= Standard error or mean
HA= Hemagglutinin	SFN= Small fiber neuropathy
HPV= Human papillomavirus	SMAD= Mothers against decapentaplegic
I= Current	TetOn= tetracycline-on expression system
IB4= α-D-galactosyl-binding lectin	TNF= Tumor-necrosis-factor
ICS= Intracellular solution	Trk= Tyrosine receptor kinase
IENFD= intraepidermal nerve fiber density	TRP= Transient receptor potential channels

IFM motif = Isoleucine (Ile)- Phenylalanin (Phe)- Methionin (Met) motif	TRPV= Transient receptor potential vanilloid
IL= Interleukin	TTX= Tetrodotoxin
iPSC= Induced-pluripotent stem cell	TTXr= Tetrodotoxin-resistant
iPSC-SN= Induced-pluripotent stem cell-derived sensory neuron	TTXs= Tetrodotoxin-sensitive
ISL1 = Insulin gene enhancer protein 1	TUJ1= Beta-III Tubulin
IV curve= Current/Voltage Curve	UV= Ultraviolet
K.o.= Knockout	V= Voltage
KRT= Keratin (gene), Krt= Keratin (protein)	V50= Voltage of half activation/inactivation
LOF= Loss-of-function	VE= Voltage error
LPS= Lipopolysaccharides	VGCSs =Voltage-gated sodium channels
m= Mouse	Vrev= Reversal potential
MA= Mechanically-activated	VSD= Voltage sensor domain
mRNA= Messenger RNA	WNT=Wingless-related integration site
N= population size, n= sample size	WT= Wild type

8 References

Ahern, C. A., Payandeh, J., Bosmans, F., & Chanda, B. (2016). The hitchhiker's guide to the voltage-gated sodium channel galaxy. In *Journal of General Physiology* (Vol. 147, Issue 1). https://doi.org/10.1085/jgp.201511492

Ahn, J., Ohk, K., Won, J., Choi, D. H., Jung, Y. H., Yang, J. H., Jun, Y., Kim, J. A., Chung, S., & Lee, S. H. (2023). Modeling of three-dimensional innervated epidermal like-layer in a microfluidic chip-based coculture system. *Nature Communications*, *14*(1). https://doi.org/10.1038/s41467-023-37187-4

Alsaloum, M., Labau, J. I. R., Liu, S., Effraim, P. R., & Waxman, S. G. (2023). Stem cell-derived sensory neurons modelling inherited erythromelalgia: normalization of excitability. *Brain*, *146*(1). https://doi.org/10.1093/brain/awac031

Alsaloum, M., Labau, J. I. R., Liu, S., Estacion, M., Zhao, P., Dib-Hajj, F., & Waxman, S. G. (2021). Contributions of NaV1.8 and NaV1.9 to excitability in human induced pluripotent stem-cell derived somatosensory neurons. *Scientific Reports*, *11*(1). https://doi.org/10.1038/s41598-021-03608-x

Arin, M. J. (2009). The molecular basis of human keratin disorders. *Human Genetics*, *125*(4). https://doi.org/10.1007/s00439-009-0646-5

Baker, M. D., Chandra, S. Y., Ding, Y., Waxman, S. G., & Wood, J. N. (2003). GTP-induced tetrodotoxin-resistant Na+ current regulates excitability in mouse and rat small diameter sensory neurones. *Journal of Physiology*, *548*(2), 373–382. https://doi.org/10.1113/jphysiol.2003.039131

Barriga, E. H., Franze, K., Charras, G., & Mayor, R. (2018). Tissue stiffening coordinates morphogenesis by triggering collective cell migration in vivo. *Nature*, *554*(7693), 523–527. https://doi.org/10.1038/nature25742

Basbaum, A. I., Bautista, D. M., Scherrer, G., & Julius, D. (2009). Cellular and Molecular Mechanisms of Pain. *Cell*, *139*(2). https://doi.org/10.1016/j.cell.2009.09.028

Baumbauer, K. M., DeBerry, J. J., Adelman, P. C., Miller, R. H., Hachisuka, J., Hsien Lee, K., Ross, S. E., Richard Koerber, H., Davis, B. M., & Albers, K. M. (2015). Keratinocytes can modulate and directly initiate nociceptive responses. *ELIFE*, *4*(e09674). https://doi.org/10.7554/eLife.09674.001

Benn, S. C., Costigan, M., Tate, S., Fitzgerald, M., & Woolf, C. J. (2001). Developmental Expression of the TTX-Resistant Voltage-Gated Sodium Channels Na v 1.8 (SNS) and Na v 1.9 (SNS2) in Primary Sensory Neurons. *Journal of Neuroscience*, *21*(6).

Bennett, D., Alex Clark, X., Huang, J., Waxman, S., & Dib-Hajj, S. (2019). *The role of voltage-gated sodium channels in pain signaling*. https://doi.org/10.1152/physrev.00052.2017.-Acute

Bennett, D. L. H., & Woods, C. G. (2014). Painful and painless channelopathies. *The Lancet Neurology*, *13*(6), 587–599. https://doi.org/10.1016/S1474-4422(14)70024-9

Boron, W., & Boulpaep, E. (2012). *Boron and Boulpaep Textbook of Medical Physiology 2nd edition*.

Bothe, S. N., & Lampert, A. (2021). The insecticide deltamethrin enhances sodium channel slow inactivation of human Nav1.9, Nav1.8 and Nav1.7. *Toxicology and Applied Pharmacology*, *428*. https://doi.org/10.1016/j.taap.2021.115676

Bronneberg, D., Spiekstra, S. W., Cornelissen, L. H., Oomens, C. W. J., Gibbs, S., Baaijens, F. P. T., & Bouten, C. V. C. (2007). Cytokine and chemokine release upon prolonged mechanical loading of the epidermis. *Experimental Dermatology*, *16*(7), 567–573. https://doi.org/10.1111/j.1600-0625.2007.00566.x

Cao, L., McDonne, A., Nitzsche, A., Alexandrou, A., Saintot, P. P., Loucif, A. J. C., Brown, A. R., Young, G., Mis, M., Randal, A., Waxman, S. G., Stanley, P., Kirby, S., Tarabar, S., Gutteridge, A., Butt, R., McKernan, R. M., Whiting, P., Ali, Z., … Stevensl, E. B. (2016). Pharmacological reversal of a pain phenotype in iPSC-derived sensory neurons and patients with inherited erythromelalgia. *Science Translational Medicine*, *8*(335). https://doi.org/10.1126/scitranslmed.aad7653

Cao, Y. A., Hickerson, R. P., Seegmiller, B. L., Grapov, D., Gross, M. M., Bessette, M. R., Phinney, B. S., Flores, M. A., Speaker, T. J., Vermeulen, A., Bravo, A. A., Bruckner, A. L., Milstone, L. M., Schwartz, M. E., Rice, R. H., & Kaspar, R. L. (2015). Gene expression profiling in pachyonychia congenita skin. *Journal of Dermatological Science*, *77*(3), 156–165. https://doi.org/10.1016/j.jdermsci.2015.01.001

Caterina, M. J., & Julius, D. (2001). The vanilloid receptor: A molecular gateway to the pain pathway. *Annual Review of Neuroscience*, *24*. https://doi.org/10.1146/annurev.neuro.24.1.487

Chambers, S. M., Qi, Y., Mica, Y., Lee, G., Zhang, X. J., Niu, L., Bilsland, J., Cao, L., Stevens, E., Whiting, P., Shi, S. H., & Studer, L. (2012). Combined small-molecule inhibition accelerates developmental timing and converts human pluripotent stem cells into nociceptors. *Nature Biotechnology*, *30*(7), 715–720. https://doi.org/10.1038/nbt.2249

Cobo, R., García-Piqueras, J., García-Mesa, Y., Feito, J., García-Suárez, O., & Vega, J. A. (2020). Peripheral mechanobiology of touch—studies on vertebrate cutaneous sensory corpuscles. *International Journal of Molecular Sciences*, *21*(17). https://doi.org/10.3390/ijms21176221

Cornelissen, L. H., Bronneberg, D., Bader, D. L., Baaijens, F. P. T., & Oomens, C. W. J. (2009). The transport profile of cytokines in epidermal equivalents subjected to mechanical loading. *Annals of Biomedical Engineering*, *37*(5), 1007–1018. https://doi.org/10.1007/s10439-009-9652-y

Coste, B., Osorio, N., Padilla, F., Crest, M., & Delmas, P. (2004). Gating and modulation of presumptive NaV1.9 channels in enteric and spinal sensory neurons. *Molecular and Cellular Neuroscience*, *26*(1), 123–134. https://doi.org/10.1016/j.mcn.2004.01.015

Cox, J. J., Reimann, F., Nicholas, A. K., Thornton, G., Roberts, E., Springell, K., Karbani, G., Jafri, H., Mannan, J., Raashid, Y., Al-Gazali, L., Hamamy, H., Valente, E. M., Gorman, S., Williams, R., McHale, D. P., Wood, J. N., Gribble, F. M., & Woods, C. G. (2006). An SCN9A channelopathy causes congenital inability to experience pain. *Nature*, *444*(7121), 894–898. https://doi.org/10.1038/nature05413

Cummins, T. R., Dib-Hajj, S. D., Black, J. A., Akopian, A. N., Wood, J. N., & Waxman, S. G. (1999). A Novel Persistent Tetrodotoxin-Resistant Sodium Current In SNS-Null And Wild-Type Small Primary Sensory Neurons. In *The Journal of Neuroscience* (Vol. 19, Issue 6). www.jneurosci.org.http://www.jneurosci.org/cgi/content/full/3758

Davidson, S., Copits, B. A., Zhang, J., Page, G., Ghetti, A., & Gereau, R. W. (2014). Human sensory neurons: Membrane properties and sensitization by inflammatory mediators. *Pain*, *155*(9), 1861–1870. https://doi.org/10.1016/j.pain.2014.06.017

Deng, T., Jovanovic, V. M., Tristan, C. A., Weber, C., Chu, P. H., Inman, J., Ryu, S., Jethmalani, Y., Ferreira de Sousa, J., Ormanoglu, P., Twumasi, P., Sen, C., Shim, J., Jayakar, S., Bear Zhang, H. X., Jo, S., Yu, W., Voss, T. C., Simeonov, A., … Singeç, I. (2023). Scalable generation of sensory neurons from human pluripotent stem cells. *Stem Cell Reports*, *18*(4). https://doi.org/10.1016/j.stemcr.2023.03.006

Dib-Hajj, S. D., Black, J. A., & Waxman, S. G. (2015). Na v 1.9: A sodium channel linked to human pain. *Nature Reviews Neuroscience*, *16*(9), 511–519. https://doi.org/10.1038/nrn3977

Dib-Hajj, S. D., Tyrrell, L., Cummins, T. R., Black, J. A., Wood, P. M., & Waxman, S. G. (1999). Two tetrodotoxin-resistant sodium channels in human dorsal root ganglion neurons. *FEBS Letters*, *462*(1–2). https://doi.org/10.1016/S0014-5793(99)01519-7

Djouhri, L., Bleazard, L., & Lawson, S. N. (1998). Association of somatic action potential shape with sensory receptive properties in guinea-pig dorsal root ganglion neurones. *Journal of Physiology*, *513*(3). https://doi.org/10.1111/j.1469-7793.1998.857ba.x

Eberhardt, E., Havlicek, S., Schmidt, D., Link, A. S., Neacsu, C., Kohl, Z., Hampl, M., Kist, A. M., Klinger, A., Nau, C., Schüttler, J., Alzheimer, C., Winkler, J., Namer, B., Winner, B., & Lampert, A. (2015). Pattern of Functional TTX-Resistant Sodium Channels Reveals a Developmental Stage of Human iPSC- and ESC-Derived Nociceptors. *Stem Cell Reports*, *5*(3), 305–313. https://doi.org/10.1016/j.stemcr.2015.07.010

Ekberg, J., Jayamanne, A., Vaughan, C. W., Aslan, S., Thomas, L., Mould, J., Drinkwater, R., Baker, M. D., Abrahamsen, B., Wood, J. N., Adams, D. J., Christie, M. J., & Lewis, R. J. (2006). μO-conotoxin MrVIB selectively blocks NaV1.8 sensory neuron specific sodium channels and chronic pain behavior without motor deficits. *Proceedings of the National Academy of Sciences of the United States of America*, *103*(45), 17030–17035. https://doi.org/10.1073/pnas.0601819103

Erlanger, J., & Gasser, H. S. (1924). THE COMPOUND NATURE OF THE ACTION CURRENT OF NERVE AS DISCLOSED BY THE CATHODE RAY OSCILLOGRAPH. *American Journal of Physiology-Legacy Content*, *70*(3). https://doi.org/10.1152/ajplegacy.1924.70.3.624

Estacion, M., Han, C., Choi, J. S., Hoeijmakers, J. G. J., Lauria, G., Drenth, J. P. H., Gerrits, M. M., Dib-Hajj, S. D., Faber, C. G., Merkies, I. S. J., & Waxman, S. G. (2011). Intra- and interfamily phenotypic diversity in pain syndromes associated with a gain-of-function variant of Na V1.7. *Molecular Pain*, *7*. https://doi.org/10.1186/1744-8069-7-92

Estacion, M., Vohra, B. P. S., Liu, S., Hoeijmakers, J., Faber, C. G., Merkies, I. S. J., Lauria, G., Black, J. A., & Waxman, S. G. (2015). Ca 2 toxicity due to reverse Na /Ca 2 exchange contributes to degeneration of neurites of DRG neurons induced by a neuropathy-

associated Nav1.7 mutation. *J Neurophysiol*, *114*, 1554–1564. https://doi.org/10.1152/jn.00195.2015.-Gain-of-function

Faber, C. G., Hoeijmakers, J. G. J., Ahn, H. S., Cheng, X., Han, C., Choi, J. S., Estacion, M., Lauria, G., Vanhoutte, E. K., Gerrits, M. M., Dib-Hajj, S., Drenth, J. P. H., Waxman, S. G., & Merkies, I. S. J. (2012). Gain of function Na V1.7 mutations in idiopathic small fiber neuropathy. *Annals of Neurology*, *71*(1), 26–39. https://doi.org/10.1002/ana.22485

Faber, C. G., Lauria, G., Merkies, I. S. J., Cheng, X., Han, C., Ahn, H. S., Persson, A. K., Hoeijmakers, J. G. J., Gerrits, M. M., Pierro, T., Lombardi, R., Kapetis, D., Dib-Hajj, S. D., & Waxman, S. G. (2012). Gain-of-function Nav1.8 mutations in painful neuropathy. *Proceedings of the National Academy of Sciences of the United States of America*, *109*(47). https://doi.org/10.1073/pnas.1216080109

Faure, L., Wang, Y., Kastriti, M. E., Fontanet, P., Cheung, K. K. Y., Petitpré, C., Wu, H., Sun, L. L., Runge, K., Croci, L., Landy, M. A., Lai, H. C., Consalez, G. G., de Chevigny, A., Lallemend, F., Adameyko, I., & Hadjab, S. (2020). Single cell RNA sequencing identifies early diversity of sensory neurons forming via bi-potential intermediates. *Nature Communications*, *11*(1). https://doi.org/10.1038/s41467-020-17929-4

Goral, R. O., Leipold, E., Nematian-Ardestani, E., & Heinemann, S. H. (2015). Heterologous expression of NaV1.9 chimeras in various cell systems. *Pflugers Archiv European Journal of Physiology*, *467*(12). https://doi.org/10.1007/s00424-015-1709-1

Gross, F., & Üçeyler, N. (2020). Mechanisms of small nerve fiber pathology. *Neuroscience Letters*, *737*. https://doi.org/10.1016/j.neulet.2020.135316

Halbert, C. L., Demers,' And, G. W., & Galloway', D. A. (1992). The E6 and E7 Genes of Human Papillomavirus Type 6 Have Weak Immortalizing Activity in Human Epithelial Cells. *JOURNAL OF VIROLOGY*, *66*(4), 2125–2134.

Han, C., Estacion, M., Huang, J., Vasylyev, D., Zhao, P., Dib-Hajj, S. D., Waxman, S. G., & Human Na, W. S. (2015). Human Na v 1.8: enhanced persistent and ramp currents contribute to distinct firing properties of human DRG neurons. *J Neurophysiol*, *113*, 3172–3185. https://doi.org/10.1152/jn.00113.2015.-Although

Huang, J., Estacion, M., Zhao, P., Dib-Hajj, F. B., Schulman, B., Abicht, A., Kurth, I., Brockmann, K., Waxman, S. G., & Dib-Hajj, S. D. (2019). A Novel Gain-of-Function Nav1.9 Mutation in a Child With Episodic Pain. *Frontiers in Neuroscience*, *13*. https://doi.org/10.3389/fnins.2019.00918

Huang, J., Han, C., Estacion, M., Vasylyev, D., Hoeijmakers, J. G. J., Gerrits, M. M., Tyrrell, L., Lauria, G., Faber, C. G., Dib-Hajj, S. D., Merkies, I. S. J., & Waxman, S. G. (2014). Gain-of-function mutations in sodium channel NaV1.9 in painful neuropathy. *Brain*, *137*(6), 1627–1642. https://doi.org/10.1093/brain/awu079

Hulme, A. J., McArthur, J. R., Maksour, S., Miellet, S., Ooi, L., Adams, D. J., Finol-Urdaneta, R. K., & Dottori, M. (2020). Molecular and Functional Characterization of Neurogenin-2 Induced Human Sensory Neurons. *Frontiers in Cellular Neuroscience*, *14*. https://doi.org/10.3389/fncel.2020.600895

Hunt, C. C. (1954). Relation of function to diameter in afferent fibers of muscle nerves. *The Journal of General Physiology*, *38*(1). https://doi.org/10.1085/jgp.38.1.117

International Association for the Study of Pain. (2011). *IASP Terminology*. Date Accessed 21/07/2025. https://www.iasp-pain.org/resources/terminology/

Julius, D., & Basbaum, A. I. (2001). Molecular mechanisms of nociception. *Nature*, *413*(6852). https://doi.org/10.1038/35093019

Kléber, M., Lee, H. Y., Wurdak, H., Buchstaller, J., Riccomagno, M. M., Ittner, L. M., Suter, U., Epstein, D. J., & Sommer, L. (2005). Neural crest stem cell maintenance by combinatorial Wnt and BMP signaling. *Journal of Cell Biology*, *169*(2). https://doi.org/10.1083/jcb.200411095

Kleggetveit, I. P., Namer, B., Schmidt, R., Helås, T., Rückel, M., Orstavik, K., Schmelz, M., & Jorum, E. (2012). High spontaneous activity of C-nociceptors in painful polyneuropathy. *Pain*, *153*(10). https://doi.org/10.1016/j.pain.2012.05.017

Klusch, A., Ponce, L., Gorzelanny, C., Schäfer, I., Schneider, S. W., Ringkamp, M., Holloschi, A., Schmelz, M., Hafner, M., & Petersen, M. (2013). Coculture model of sensory neurites and keratinocytes to investigate functional interaction: Chemical stimulation and atomic force microscope-transmitted mechanical stimulation combined with live-cell imaging. In *Journal of Investigative Dermatology* (Vol. 133, Issue 5, pp. 1387–1390). Nature Publishing Group. https://doi.org/10.1038/jid.2012.471

Körner, J., & Lampert, A. (2022). Functional subgroups of rat and human sensory neurons: a systematic review of electrophysiological properties. *Pflugers Archiv European Journal of Physiology*, *474*(4). https://doi.org/10.1007/s00424-021-02656-6

Köster, P. A., Leipold, E., Tigerholm, J., Maxion, A., Namer, B., Stiehl, T., & Lampert, A. (2025). Nociceptor sodium channels shape subthreshold phase, upstroke, and shoulder of action potentials. *The Journal of General Physiology*, *157*(2). https://doi.org/10.1085/jgp.202313526

Kreß, L., Egenolf, N., Sommer, C., & Üçeyler, N. (2023). Cytokine expression profiles in white blood cells of patients with small fiber neuropathy. *BMC Neuroscience*, *24*(1). https://doi.org/10.1186/s12868-022-00770-4

Krishnan-Kutty, V., Bigliardi, P. L., Dykas, M. M., Pomp, O., Kyaw, H. M., Poddar, K., Venkatesan, T., & Bigliardi-Qi, M. (2017). Peripheral nerve fibres form multifacet interactions with keratinocytes in a novel complete human 2D culture model. *Experimental Dermatology*, *26*(3), 281–284. https://doi.org/10.1111/exd.13181

Kupari, J., & Ernfors, P. (2023). Molecular taxonomy of nociceptors and pruriceptors. *Pain*, *164*(6). https://doi.org/10.1097/j.pain.0000000000002831

Labau, J. I. R., Andelic, M., Faber, C. G., Waxman, S. G., Lauria, G., & Dib-Hajj, S. D. (2022). Recent advances for using human induced-pluripotent stem cells as pain-in-a-dish models of neuropathic pain. In *Experimental Neurology* (Vol. 358). Academic Press Inc. https://doi.org/10.1016/j.expneurol.2022.114223

Laly, A. C., Sliogeryte, K., Pundel, O. J., Ross, R., Keeling, M. C., Avisetti, D., Waseem, A., Gavara, N., & Connelly, J. T. (2021). The keratin network of intermediate filaments regulates keratinocyte rigidity sensing and nuclear mechanotransduction. *Science Advances*, *7*(5). https://doi.org/10.1126/sciadv.abd6187

Lampert, A., Bennett, D. L., McDermott, L. A., Neureiter, A., Eberhardt, E., Winner, B., & Zenke, M. (2020). Human sensory neurons derived from pluripotent stem cells for disease modelling and personalized medicine. In *Neurobiology of Pain* (Vol. 8). Elsevier B.V. https://doi.org/10.1016/j.ynpai.2020.100055

Lanier, J., Dykes, I. M., Nissen, S., Eng, S. R., & Turner, E. E. (2009). Brn3a regulates the transition from neurogenesis to terminal differentiation and represses non-neural gene expression in the trigeminal ganglion. *Developmental Dynamics*, *238*(12). https://doi.org/10.1002/dvdy.22145

Lauria, G., & Lombardi, R. (2012). Small fiber neuropathy: Is skin biopsy the holy grail? *Current Diabetes Reports*, *12*(4). https://doi.org/10.1007/s11892-012-0280-9

Lee, J., Kim, S., Kim, H. M., Kim, H. J., & Yu, F. H. (2019). NaV1.6 and NaV1.7 channels are major endogenous voltage-gated sodium channels in ND7/23 cells. *PLoS ONE*, *14*(8). https://doi.org/10.1371/journal.pone.0221156

Lee, J., van der Valk, W. H., Serdy, S. A., Deakin, C. C., Kim, J., Le, A. P., & Koehler, K. R. (2022). Generation and characterization of hair-bearing skin organoids from human pluripotent stem cells. In *Nature Protocols* (Vol. 17, Issue 5). https://doi.org/10.1038/s41596-022-00681-y

Leipold, E., Liebmann, L., Korenke, G. C., Heinrich, T., Gießelmann, S., Baets, J., Ebbinghaus, M., Goral, R. O., Stödberg, T., Hennings, J. C., Bergmann, M., Altmüller, J., Thiele, H., Wetzel, A., Nürnberg, P., Timmerman, V., De Jonghe, P., Blum, R., Schaible, H. G., … Kurth, I. (2013). A de novo gain-of-function mutation in SCN11A causes loss of pain perception. *Nature Genetics*, *45*(11), 1399–1407. https://doi.org/10.1038/ng.2767

Lepski, G., Jannes, C. E., Nikkhah, G., & Bischofberger, J. (2013). cAMP promotes the differentiation of neural progenitor cells in vitro via modulation of voltage-gated calcium channels. *Frontiers in Cellular Neuroscience*, *SEP*. https://doi.org/10.3389/fncel.2013.00155

Lessard, J. C., Piña-Paz, S., Rotty, J. D., Hickerson, R. P., Kaspar, R. L., Balmain, A., & Coulombe, P. A. (2013). Keratin 16 regulates innate immunity in response to epidermal barrier breach. *Proceedings of the National Academy of Sciences of the United States of America*, *110*(48), 19537–19542. https://doi.org/10.1073/pnas.1309576110

Lin, Z., Santos, S., Padilla, K., Printzenhoff, D., & Castle, N. A. (2016). Biophysical and pharmacological characterization of Nav1.9 voltage dependent sodium channels stably expressed in HEK-293 cells. *PLoS ONE*, *11*(8). https://doi.org/10.1371/journal.pone.0161450

Liu, W., Xiong, S., Zhang, Y., Du, J., Dong, C., Yu, Z., & Ma, X. (2021). Transcriptome Profiling Reveals Important Transcription Factors and Biological Processes in Skin Regeneration

Mediated by Mechanical Stretch. *Frontiers in Genetics*, *12*. https://doi.org/10.3389/fgene.2021.757350

Liu, Y., Szymański de Toledo, M., Ernst, S., Hautvast, P., Kesdogan, A., Körner, J., Zenke, M., Neureiter, A., & Lampert, A. (2024). The pain target NaV1.7 is expressed late during human iPS cell differentiation into sensory neurons as determined in high-resolution imaging. *European Journal of Physiology*, *476*.

Lloyd, D. P. C. (1943). NEURON PATTERNS CONTROLLING TRANSMISSION OF IPSILATERAL HIND LIMB REFLEXES IN CAT. *Journal of Neurophysiology*, *6*(4). https://doi.org/10.1152/jn.1943.6.4.293

Ma, Q., Fode, C., Guillemot, F., & Anderson, D. J. (1999). NEUROGENIN1 and NEUROGENIN2 control two distinct waves of neurogenesis in developing dorsal root ganglia. *Genes and Development*, *13*(13). https://doi.org/10.1101/gad.13.13.1717

Martinac, B., & Cox, C. D. (2017). Mechanosensory Transduction: Focus on Ion Channels. In *Reference Module in Life Sciences*. Elsevier. https://doi.org/10.1016/b978-0-12-809633-8.08094-8

Mccarthy, R. L., De brito, M., & O'toole, E. (2023). Pachyonychia Congenita: Clinical Features and Future Treatments. *The Keio Journal of Medicine*. https://doi.org/10.2302/kjm.2023-0012-ir

Mcdermott, L. A., Weir, G. A., Themistocleous, A. C., Tracey, I., Serra, J., Bennett, D. L., Mcdermott, L. A., Weir, G. A., Themistocleous, A. C., Segerdahl, A. R., Blesneac, I., & Bennett, D. L. (2019). Defining the Functional Role of Na V 1 . 7 in Human Article Defining the Functional Role of Na V 1 . 7 in Human Nociception. *Neuron*, *101*(5).

Meents, J. E., Bressan, E., Sontag, S., Foerster, A., Hautvast, P., Rösseler, C., Hampl, M., Schüler, H., Goetzke, R., Le, T. K. C., Kleggetveit, I. P., Le Cann, K., Kerth, C., Rush, A. M., Rogers, M., Kohl, Z., Schmelz, M., Wagner, W., Jørum, E., … Lampert, A. (2019). The role of Nav1.7 in human nociceptors: Insights from human induced pluripotent stem cell-derived sensory neurons of erythromelalgia patients. *Pain*, *160*(6), 1327–1341. https://doi.org/10.1097/j.pain.0000000000001511

Meltzer, S., Santiago, C., Sharma, N., & Ginty, D. D. (2021). The cellular and molecular basis of somatosensory neuron development. *Neuron*, *109*(23). https://doi.org/10.1016/j.neuron.2021.09.004

Middleton, S. J., Markússon, S., Åkerlund, M., Deme, J. C., Tseng, M., Li, W., Zuberi, S. R., Kuteyi, G., Sarkies, P., Baskozos, G., Perez-Sanchez, J., Farah, A., Hébert, H. L., Toikumo, S., Yu, Z., Maxwell, S., Dong, Y. Y., Kessler, B. M., Kranzler, H. R., … Bennett, D. L. (2025). SLC45A4 is a pain gene encoding a neuronal polyamine transporter. *Nature*. https://doi.org/10.1038/s41586-025-09326-y

Mikesell, A. R., Isaeva, O., Moehring, F., Sadler, K. E., Menzel, A. D., & Stucky, C. L. (2022). Keratinocyte PIEZO1 modulates cutaneous mechanosensation. *ELife*, *11*. https://doi.org/10.7554/eLife.65987

Mis, M. A., Yang, Y., Tanaka, B. S., Gomis-Perez, C., Liu, S., Dib-Hajj, F., Adi, T., Garcia-Milian, R., Schulman, B. R., Dib-Hajj, S. D., & Waxman, S. G. (2019). Resilience to pain: A peripheral

component identified using induced pluripotent stem cells and dynamic clamp. *Journal of Neuroscience*, *39*(3). https://doi.org/10.1523/JNEUROSCI.2433-18.2018

Moehring, F., Cowie, A. M., Menzel, A. D., Weyer, A. D., Grzybowski, M., Arzua, T., Geurts, A. M., Palygin, O., & Stucky, C. L. (2018). Keratinocytes mediate innocuous and noxious touch via ATP-P2X4 signaling. *ELife*, *7*(e31684). https://doi.org/10.7554/eLife.31684.001

Moll, R., Divo, M., & Langbein, L. (2008). The human keratins: Biology and pathology. *Histochemistry and Cell Biology*, *129*(6). https://doi.org/10.1007/s00418-008-0435-6

Möller, A., Lippert, U., Lessmann, D., Kolde, G., Hamann, K., Welker, P., Schadendorf, D., Rosenbach, T., Luger, T., & Czarnetzki, B. M. (1993). Human mast cells produce IL-8. *The Journal of Immunology*, *151*(6). https://doi.org/10.4049/jimmunol.151.6.3261

Namer, B., & Lampert, A. (2025). Functional signatures of human somatosensory C fibers by microneurography. *Pain*, *00*. http://dx.doi.org/10.1097/j.pain.0000000000003605

Namer, B., Schmidt, D., Eberhardt, E., Maroni, M., Dorfmeister, E., Kleggetveit, I. P., Kaluza, L., Meents, J., Gerlach, A., Lin, Z., Winterpacht, A., Dragicevic, E., Kohl, Z., Schüttler, J., Kurth, I., Warncke, T., Jorum, E., Winner, B., & Lampert, A. (2019). Pain relief in a neuropathy patient by lacosamide: Proof of principle of clinical translation from patient-specific iPS cell-derived nociceptors. *EBioMedicine*, *39*, 401–408. https://doi.org/10.1016/j.ebiom.2018.11.042

Neureiter, A., Eberhardt, E., & Lampert, A. (2022). Differentiation of iPS-Cells into Peripheral Sensory Neurons. *Methods in Molecular Biology*, *2429*. https://doi.org/10.1007/978-1-0716-1979-7_11

Oh, S., Chung, H., Chang, S., Lee, S. H., Seok, S. H., & Lee, H. (2019). Effect of Mechanical Stretch on the DNCB-induced Proinflammatory Cytokine Secretion in Human Keratinocytes. *Scientific Reports*, *9*(1). https://doi.org/10.1038/s41598-019-41480-y

Osteen, J., Immani, S., Tapley, T., Indersmitten, T., Hurst, N., Healey, T., Aertgeerts, K., Negulescu, P., & Lechner, S. (2024). Pharmacology and Mechanism of Action of Suzetrigine, a Potent and Selective NaV1.8 Pain Signal Inhibitor for the Treatment of Moderate to Severe Pain. *Pain Ther*.

Pachyonychia Congenita Research & Support Project. (2021). *Pachyonychia.org*. Date Accessed 21/07/2025. https://www.pachyonychia.org/

Pan, B., Byrnes, K., Schwartz, M., Hansen, C. D., Campbell, C. M., Krupiczojc, M., Caterina, M. J., & Polydefkis, M. (2016). Peripheral neuropathic changes in pachyonychia congenita. *Pain*, *157*(12), 2843–2853. https://doi.org/10.1097/j.pain.0000000000000711

Qiao, P., Guo, W., Ke, Y., Fang, H., Zhuang, Y., Jiang, M., Zhang, J., Shen, S., Qiao, H., Dang, E., & Wang, G. (2019). Mechanical Stretch Exacerbates Psoriasis by Stimulating Keratinocyte Proliferation and Cytokine Production. *Journal of Investigative Dermatology*, *139*(7), 1470–1479. https://doi.org/10.1016/j.jid.2018.12.019

Raible, D. W., & Ragland, J. W. (2005). Reiterated Wnt and BMP signals in neural crest development. *Seminars in Cell and Developmental Biology*, *16*(6). https://doi.org/10.1016/j.semcdb.2005.06.008

Raja, S. N., Carr, D. B., Cohen, M., Finnerup, N. B., Flor, H., Gibson, S., Keefe, F. J., Mogil, J. S., Ringkamp, M., Sluka, K. A., Song, X. J., Stevens, B., Sullivan, M. D., Tutelman, P. R., Ushida, T., & Vader, K. (2020). The Revised IASP definition of pain: concepts, challenges, and compromises. *Pain*, *161*(9).

Ramakers, C., Ruijter, J. M., Lekanne Deprez, R. H., & Moorman, A. F. M. (2003). Assumption-free analysis of quantitative real-time polymerase chain reaction (PCR) data. *Neuroscience Letters*, *339*(1). https://doi.org/10.1016/S0304-3940(02)01423-4

Renganathan, M., Dib-Hajj, S., & Waxman, S. G. (2002). Nav1.5 underlies the "third TTX-R sodium current" in rat small DRG neurons. *Molecular Brain Research*, *106*(1–2). https://doi.org/10.1016/S0169-328X(02)00411-4

Robinton, D. A., & Daley, G. Q. (2012). The promise of induced pluripotent stem cells in research and therapy. *Nature*, *481*(7381). https://doi.org/10.1038/nature10761

Röderer, P. (2021). *Human iPSC-derived in vitro models of the peripheral nervous system for cellular pain and somatosensation research*. Rheinischen Friedrich-Wilhelms-Universität Bonn.

Romanshin, D., Tolstova, T., Vashaver, A., Kozhin, P., Rusanov, A., & Luzgina, N. (2024). Keratins 6, 16, and 17 in Health and Disease: A Summary of Recent Findings. *Curr Issues Mol Biol*, *46*(8). https://doi.org/ 10.3390/cimb46080508

Rotty, J. D., & Coulombe, P. A. (2012). A wound-induced keratin inhibits Src activity during keratinocyte migration and tissue repair. *Journal of Cell Biology*, *197*(3). https://doi.org/10.1083/jcb.201107078

Rush, A. M., & Waxman, S. G. (2004). PGE 2 increases the tetrodotoxin-resistant Na v1.9 sodium current in mouse DRG neurons via G-proteins. *Brain Research*, *1023*(2), 264–271. https://doi.org/10.1016/j.brainres.2004.07.042

Samuelov, L., Smith, F. J. D., Hansen, C. D., & Sprecher, E. (2020). Revisiting pachyonychia congenita: a case-cohort study of 815 patients. *British Journal of Dermatology*, *182*(3). https://doi.org/10.1111/bjd.18794

Schinke, C., Fernandez Vallone, V., Ivanov, A., Peng, Y., Körtvelyessy, P., Nolte, L., Huehnchen, P., Beule, D., Stachelscheid, H., Boehmerle, W., & Endres, M. (2021). Modeling chemotherapy induced neurotoxicity with human induced pluripotent stem cell (iPSC) -derived sensory neurons. *Neurobiology of Disease*, *155*. https://doi.org/10.1016/j.nbd.2021.105391

Schrenk-Siemens, K., Pohle, J., Rostock, C., Abd El Hay, M., Lam, R. M., Szczot, M., Lu, S., Chesler, A. T., & Siemens, J. (2022). Human Stem Cell-Derived TRPV1-Positive Sensory Neurons: A New Tool to Study Mechanisms of Sensitization. *Cells*, *11*(18). https://doi.org/10.3390/cells11182905

Schutte, S. C., Kadakia, F., & Davidson, S. (2021). Skin-Nerve Co-Culture Systems for Disease Modeling and Drug Discovery. In *Tissue Engineering - Part C: Methods* (Vol. 27, Issue 2, pp. 89–99). Mary Ann Liebert Inc. https://doi.org/10.1089/ten.tec.2020.0296

Shao, D., Okuse, K., & Djamgoz, M. B. A. (2009). Protein-protein interactions involving voltage-gated sodium channels: Post-translational regulation, intracellular trafficking and

functional expression. In *International Journal of Biochemistry and Cell Biology* (Vol. 41, Issue 7). https://doi.org/10.1016/j.biocel.2009.01.016

Sharma, N., Flaherty, K., Lezgiyeva, K., Wagner, D. E., Klein, A. M., & Ginty, D. D. (2020). The emergence of transcriptional identity in somatosensory neurons. *Nature*, *577*(7790). https://doi.org/10.1038/s41586-019-1900-1

Shutova, M. S., & Boehncke, W. H. (2022). Mechanotransduction in Skin Inflammation. *Cells*, *11*(13). https://doi.org/10.3390/cells11132026

Simões-Costa, M., & Bronner, M. E. (2013). Insights into neural crest development and evolution from genomic analysis. *Genome Research*, *23*(7). https://doi.org/10.1101/gr.157586.113

Sisignano, M., Baron, R., Scholich, K., & Geisslinger, G. (2014). Mechanism-based treatment for chemotherapy-induced peripheral neuropathic pain. In *Nature Reviews Neurology* (Vol. 10, Issue 12). https://doi.org/10.1038/nrneurol.2014.211

Sizova, D. V., Huang, J., Akin, E. J., Estacion, M., Gomis-Perez, C., Waxman, S. G., & Dib-Hajj, S. D. (2020). A 49-residue sequence motif in the C terminus of Nav1.9 regulates trafficking of the channel to the plasma membrane. *Journal of Biological Chemistry*, *295*(4), 1077–1090. https://doi.org/10.1074/jbc.RA119.011424

Smith, J. R., Vallier, L., Lupo, G., Alexander, M., Harris, W. A., & Pedersen, R. A. (2008). Inhibition of Activin/Nodal signaling promotes specification of human embryonic stem cells into neuroectoderm. *Developmental Biology*, *313*(1). https://doi.org/10.1016/j.ydbio.2007.10.003

Sopacua, M., Hoeijmakers, J. G. J., Merkies, I. S. J., Lauria, G., Waxman, S. G., & Faber, C. G. (2019). Small-fiber neuropathy: Expanding the clinical pain universe. *Journal of the Peripheral Nervous System*, *24*(1). https://doi.org/10.1111/jns.12298

Speckmann, E., Hescheler, J., & Köhling, R. (2024). *Physiologie* (8th ed.).

Stewart, R. G., Osorno, T., Fujita, A., Jo, S., Ferraiuolo, A., Carlin, K., & Bean, B. P. (2025). Modulation of human dorsal root ganglion neuron firing by the Nav1.8 inhibitor suzetrigine. *Proceedings of the National Academy of Sciences of the United States of America*, *122*(22). https://doi.org/10.1073/pnas.2503570122

Stuhlmiller, T. J., & García-Castro, M. I. (2012). Current perspectives of the signaling pathways directing neural crest induction. *Cellular and Molecular Life Sciences*, *69*(22). https://doi.org/10.1007/s00018-012-0991-8

Sun, Y., Dykes, I. M., Liang, X., Eng, S. R., Evans, S. M., & Turner, E. E. (2008). A central role for Islet1 in sensory neuron development linking sensory and spinal gene regulatory programs. *Nature Neuroscience*, *11*(11). https://doi.org/10.1038/nn.2209

Takahashi, K., Tanabe, K., Ohnuki, M., Narita, M., Ichisaka, T., Tomoda, K., & Yamanaka, S. (2007). Induction of Pluripotent Stem Cells from Adult Human Fibroblasts by Defined Factors. *Cell*, *131*(5). https://doi.org/10.1016/j.cell.2007.11.019

Takahashi, K., & Yamanaka, S. (2006). Induction of Pluripotent Stem Cells from Mouse Embryonic and Adult Fibroblast Cultures by Defined Factors. *Cell*, *126*(4). https://doi.org/10.1016/j.cell.2006.07.024

Talagas, M., Lebonvallet, N., Berthod, F., & Misery, L. (2020). Lifting the veil on the keratinocyte contribution to cutaneous nociception. *Protein and Cell*, *11*(4), 239–250. https://doi.org/10.1007/s13238-019-00683-9

Talagas, M., Lebonvallet, N., Leschiera, R., Sinquin, G., Elies, P., Haftek, M., Pennec, J. P., Ressnikoff, D., La Padula, V., Le Garrec, R., L'herondelle, K., Mignen, O., Le Pottier, L., Kerfant, N., Reux, A., Marcorelles, P., & Misery, L. (2020). Keratinocytes Communicate with Sensory Neurons via Synaptic-like Contacts. *Annals of Neurology*, *88*(6), 1205–1219. https://doi.org/10.1002/ana.25912

Tsutsumi, M., Inoue, K., Denda, S., Ikeyama, K., Goto, M., & Denda, M. (2009). Mechanical-stimulation-evoked calcium waves in proliferating and differentiated human keratinocytes. *Cell and Tissue Research*, *338*(1), 99–106. https://doi.org/10.1007/s00441-009-0848-0

Usoskin, D., Furlan, A., Islam, S., Abdo, H., Lönnerberg, P., Lou, D., Hjerling-Leffler, J., Haeggström, J., Kharchenko, O., Kharchenko, P. V., Linnarsson, S., & Ernfors, P. (2015). Unbiased classification of sensory neuron types by large-scale single-cell RNA sequencing. *Nature Neuroscience*, *18*(1). https://doi.org/10.1038/nn.3881

van den Braak, N. W., Kuehs, S., Peschke, G. Z., Namer, B., Lischka, A., Eggermann, K., Dumke, C., Eswaran, V., Nikolin, S., Weis, J., Schulz, J. B., Lampert, A., Kurth, I., Rolke, R., Leipold, E., & Dohrn, M. F. (2025). Altered NaV1.9 channel activity in two Tyr66Ser variant carriers with small fiber dysfunction. *J Gen Physiol*, *157*(6). https://doi.org/10.1085/jgp.202413691

Van Hecke, O., Austin, S. K., Khan, R. A., Smith, B. H., & Torrance, N. (2014). Neuropathic pain in the general population: A systematic review of epidemiological studies. *Pain*, *155*(4). https://doi.org/10.1016/j.pain.2013.11.013

Vanoye, C. G., Kunic, J. D., Ehring, G. R., & George, A. L. (2013). Mechanism of sodium channel NaV1.9 potentiation by G-protein signaling. *Journal of General Physiology*, *141*(2), 193–202. https://doi.org/10.1085/jgp.201210919

Vetter, I., Mozar, C. A., Durek, T., Wingerd, J. S., Alewood, P. F., Christie, M. J., & Lewis, R. J. (2012). Characterisation of Na v types endogenously expressed in human SH-SY5Y neuroblastoma cells. *Biochemical Pharmacology*, *83*(11), 1562–1571. https://doi.org/10.1016/j.bcp.2012.02.022

Wainger, B. J., Buttermore, E. D., Oliveira, J. T., Mellin, C., Lee, S., Saber, W. A., Wang, A. J., Ichida, J. K., Chiu, I. M., Barrett, L., Huebner, E. A., Bilgin, C., Tsujimoto, N., Brenneis, C., Kapur, K., Rubin, L. L., Eggan, K., & Woolf, C. J. (2015). Modeling pain in vitro using nociceptor neurons reprogrammed from fibroblasts. *Nature Neuroscience*, *18*(1), 17–24. https://doi.org/10.1038/nn.3886

Wang, J., Ou, S. W., & Wang, Y. J. (2017). Distribution and function of voltage-gated sodium channels in the nervous system. *Channels*, *11*(6). https://doi.org/10.1080/19336950.2017.1380758

Yuan, J. H., Estacion, M., Mis, M. A., Tanaka, B. S., Schulman, B. R., Chen, L., Liu, S., Dib-Hajj, F. B., Dib-Hajj, S. D., & Waxman, S. G. (2021). KCNQ variants and pain modulation: a missense variant in Kv7.3 contributes to pain resilience. *Brain Communications*, *3*(3). https://doi.org/10.1093/braincomms/fcab212

Zechner, D., Müller, T., Wende, H., Walther, I., Taketo, M. M., Crenshaw, E. B., Treier, M., Birchmeier, W., & Birchmeier, C. (2007). Bmp and Wnt/β-catenin signals control expression of the transcription factor Olig3 and the specification of spinal cord neurons. *Developmental Biology*, *303*(1). https://doi.org/10.1016/j.ydbio.2006.10.045

Zhang, X., Hartung, J. E., & Gold, M. S. (2024). Persistent (Nav1.9) sodium currents in human dorsal root ganglion neurons. *Pain*. https://doi.org/10.1097/j.pain.0000000000003394

Zhao, P., Barr, T. P., Hou, Q., Dib-Hajj, S. D., Black, J. A., Albrecht, P. J., Petersen, K., Eisenberg, E., Wymer, J. P., Rice, F. L., & Waxman, S. G. (2008). Voltage-gated sodium channel expression in rat and human epidermal keratinocytes: Evidence for a role in pain. *Pain*, *139*(1), 90–105. https://doi.org/10.1016/j.pain.2008.03.016

Zhou, X., Xiao, Z., Xu, Y., Zhang, Y., Tang, D., Wu, X., Tang, C., Chen, M., Shi, X., Chen, P., Liang, S., & Liu, Z. (2017). Electrophysiological and pharmacological analyses of Nav1.9 voltage-gated sodium channel by establishing a heterologous expression system. *Frontiers in Pharmacology*, *8*(NOV). https://doi.org/10.3389/fphar.2017.00852

Zurek, N. A., Ehsanian, R., Goins, A. E., Adams, I. M., Petersen, T., Goyal, S., Shilling, M., Westlund, K. N., & Alles, S. R. A. (2024). Electrophysiological Analyses of Human Dorsal Root Ganglia and Human Induced Pluripotent Stem Cell-derived Sensory Neurons From Male and Female Donors. *Journal of Pain*, *25*(6). https://doi.org/10.1016/j.jpain.2023.12.008

9 Appendix

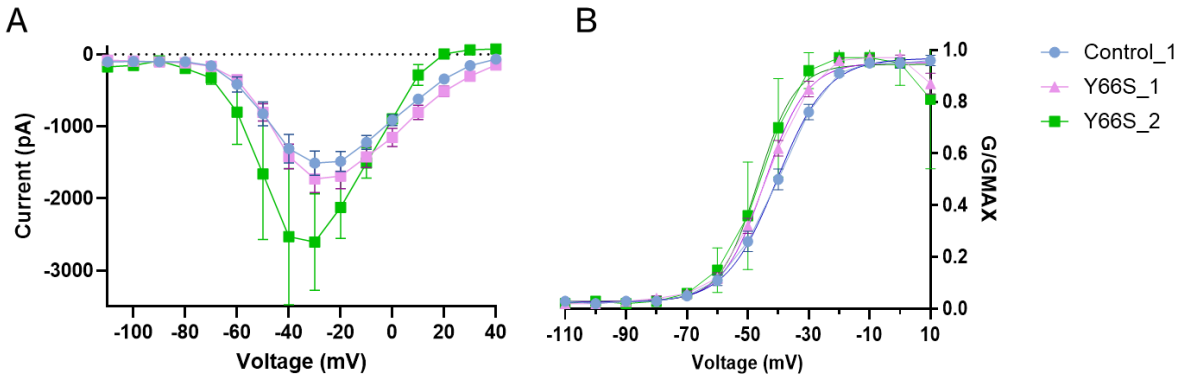

Figure Appendix 1 Activation of TTXr channels in NGN1-differentiated iPSC-SN. iPSC-SN were patch clamped at DIV55-64. A) IV curve and B) conductance (G) curve normalized to the maximum conductance and displayed with a line connecting the data points (lighter colour) and a Boltzmann fit (darker colour) for Ctrl_1, Y66S_1 and Y66S_2. N=3, n=24-32 for Ctrl_1 and Y66S_1; N=1, **n=3 for Y66S_2**.

10 Eidesstattliche Erklärung

Fiona Maria Roll

erklärt hiermit, dass diese Dissertation und die darin dargelegten Inhalte die eigenen sind und selbstständig, als Ergebnis der eigenen originären Forschung, generiert wurden.

Hiermit erkläre ich an Eides statt

1. Diese Arbeit wurde vollständig oder größtenteils in der Phase als Promovierender dieser Fakultät und Universität angefertigt;
2. Sofern irgendein Bestandteil dieser Dissertation zuvor für einen akademischen Abschluss oder eine andere Qualifikation an dieser oder einer anderen Institution verwendet wurde, wurde dies klar angezeigt;
3. Wenn immer andere eigene- oder Veröffentlichungen Dritter herangezogen wurden, wurden diese klar benannt;
4. Wenn aus anderen eigenen- oder Veröffentlichungen Dritter zitiert wurde, wurde stets die Quelle hierfür angegeben. Diese Dissertation ist vollständig meine eigene Arbeit, mit der Ausnahme solcher Zitate;
5. Alle wesentlichen Quellen von Unterstützung wurden benannt;
6. Wenn immer ein Teil dieser Dissertation auf der Zusammenarbeit mit anderen basiert, wurde von mir klar gekennzeichnet, was von anderen und was von mir selbst erarbeitet wurde;
7. Kein Teil dieser Arbeit wurde vor deren Einreichung veröffentlicht.

03.03.2026

11 Acknowledgements

First and foremost, I would like to thank Prof. Angelika Lampert for providing me with the opportunity to persue my PhD in the field of neurophysiology and chronic pain. I appreciated every scientific discussion we had, and I am grateful to have been mentored by not only a scientifically accomplished but also a kind and supportive supervisor. I truly believe that the positive atmosphere in our laboratory is a reflection of your leadership. Thank you for making me a better scientist not only in terms of scientific knowledge, but also in terms of communication, organization, and networking, and for allowing me to pursue my personal career development goals by joining international conferences, the ZDF documentary, the RWTH Aachen Kinderuni and the Cold Spring Harbor "Ion Channels in Synaptic & Neural Circuit Physiology" course.

I would further like to thank my second supervisor Prof. Laura De Laporte, who made it possible for me to pursue a Dr. rer. Nat- title and always made time for questions and meetings, despite her very busy schedule. Your insights into my project from another angle were extremely valuable to me. Thank you for teaching me all about the fantastic world of hydrogels and proving that you can build (almost) anything you want.

Special thanks go to my friend and post-doctoral supervisor Dr. Andelain Erickson for teaching me electrophysiology with endless patience. You have successfully turned me (a stem cell biologist) into an electrophysiologist who loves what she does. Furthermore, special thanks to Dr. Pascal Röderer for his valuable feedback on my doctoral thesis.

I would like to express my sincere gratitude to the ME3T graduate school for funding my PhD and for providing an amazing curriculum to broaden my scientific horizon. It is remarkable how much passion and effort were poured into the education of the PhDs in this graduate school. I would further like to thank my fellow ME3T PhDs for the companionship along the way and the many, many rounds of card games at the ME3T retreats. It was an honor to serve with you all. Special thanks go to Mert Karpt and Kyeongmin Kim for the collaboration on the keratinocyte compression project. The moment we shared observing that keratinocytes are sticky will never be forgotten.

I would like to thank the whole AG Lampert for being a fantastic workplace, with such a kind and supportive spirit. Many of you have become close friends and I appreciated every bad joke, punctual mensa session, Wels meme, pop-cultural and sport event summary and after-work cooking. It is remarkable how lunch with you could fix any mishaps in the lab. No one can say for certain if I would have made it through my PhD without you, but I can say for certain that it would not have been this fun.

Scientific research takes a village and this was mine; I am grateful for the scientific support throughout my PhD by Dr. Anika Neureiter, Dr. Esther Eberhardt, Dr. Andelain Erickson, Dr. Jannis Körner, Jan Roßberg, Dr. Aylin Kesdoğan, Marlene Menke, Luise Rüßmann, Danxia Bao, Vishal Eswaran, Lennart Müller, Dr. Pascal Röderer, Dr. Mariia Suslova, Petra Hautvast, Dr. Nicole Schwarz, Dr. Aaron Barbendreyer, Raphael Tönshoff, Mert Karpat, Kyeongmin Kim and all of AG Lampert and ME3T.

Finally and most important of all, I would like to thank my mum, who gifted me my love for science and was there to support me through every scientific crisis, and my brother, who was so loudly proud of me that I couldn't hear my own doubts.